University of Blida 1
Institute of Aeronautics and Space Studies

STUDY OF THE MECHANICAL BEHAVIOUR OF POROUS COMPOSITES REINFORCED WITH GRAPHENE UNDER COMBINED LOADS

A thesis submitted by

Abdellah Hassaine

for the obtention of the

Doctorate degree in Aeronautics

Defended publicly on the 7th of March 2024, in front of jury members:

Amina Benkhedda	Professor, University of Blida 1	President
Amale Mahi	MCA, University of Blida 1	Supervisor
Abdelouahed Tounsi	Professor, University of Sidi Bel Abbes	Examiner
Mohamed Bourada	Professor, University of Sidi Bel Abbes	Examiner
Zouaoui Sereir	Professor, University of Science and Technology of Oran	Examiner
Mohamed Khodjet-Kesba	MCA, University of Blida 1	Examiner

Abstract

Functionally graded material (FGM) composites represent an exciting and active field of research in mechanical and aerospace engineering. These materials are characterized by a graded variation of certain material properties, which occurs generally between metal and ceramic. In parallel, nanomaterials are also catching the interest of researchers due to their extraordinary physical properties, particularly in structural reinforcing. We study in this thesis the use of graphene platelets (Gpls) nanomaterial to reinforce porous metal-ceramic FGMs, which is a case of study that has not been previously reported in the literature. We utilize a three-steps modelling procedure to represent the material properties of this multi-parametric FGM, and a hyperbolic higher-order plate theory to represent transverse shear effects. The general equations of equilibrium were derived by hand using Hamilton's principle, and were solved analytically for simply-supported plates. After method validation of the developed Python codes, we carried out various parametric examples to study the influence of the base FGM composition, GPls, porosity, and plate's dimensions on the mechanical behaviour of rectangular FGM plates (including the free vibration, static bending, and buckling). The obtained results can serve as a guideline for future research on porous GPls-reinforced metal-ceramic FGMs.

Keywords: Functionally graded material, composite material, plate, free vibration, bending, buckling, graphene, porosity.

ملخص

المواد المركبة المتدرجة وظيفيا تمثل نطاق بحث مثير ونشط في الهندسة الميكانيكية و الجوية-الفضائية. هذه المواد تتميز بتغير متدرج في إحدى خصائص المادة، والذي يكون عادة بين المعدن والسيراميك. في المقابل، تأخذ مواد النانو اهتمام الباحثين لخصائصها الفيزيائية غير الإعتيادية، وخاصة في التقوية البنيوية. ندرس في هذه الأطروحة استعمال صُفيحات الغرافين النانوية لتقوية مواد المعدن-سيراميك المتدرجة وظيفيا والمسامية، وهي مسألة لم يُتطرق إليها من قبل في الأعمال البحثية. إعتمدنا على عملية نمذجة من ثلاث خطوات لتمثيل خصائص هذه المادة المتدرجة متعددة العوامل، و بنظرية قطع زائد عالية الرتبة لتمثيل آثار القص العرضي. تم استخراج معادلات حالة التوازن العامة يدويا باستعمال مبدأ هاميلتون، ثم حُلَّت بطريقة تحليلية لألواح مسندة بمفاصل بسيطة. بعد التحقق من صحة طريقة أكواد البايثون المألفة، درسنا مسائل عاملية متنوعة لتحليل آثار كل من تكوين المادة المتدرجة، صُفيحات الغرافين، المسامات، و أبعاد اللوح على الإستجابة الميكانيكية (والتي تشمل الإهتزاز الحر، الإنثناء السكوني، والإحدداب). النتائج المحصَّلة تفيد كمعيار للأبحاث القادمة على مواد المعدن-سراميك المتدرجة المسماية و المقواة بصُفيحات الغرافين.

كلمات مفتاحية: مادة متدرجة وظيفيا، مادة مركبة، لوح أو صفيحة، إهتزاز حر، إنثناء، إحدداب، غرافين، مسامية.

بِسْمِ ٱللَّهِ ٱلرَّحْمَٰنِ ٱلرَّحِيمِ

وَٱللَّهُ أَخْرَجَكُم مِّنۢ بُطُونِ أُمَّهَٰتِكُمْ لَا تَعْلَمُونَ شَيْـًٔا وَجَعَلَ لَكُمُ ٱلسَّمْعَ وَٱلْأَبْصَٰرَ وَٱلْأَفْـِٔدَةَ لَعَلَّكُمْ تَشْكُرُونَ

(سورة النحل)

Dedicated to my parents,

To Aymen, Abdelaziz, Morad, Abdelmalek, and Mr Boudani,

And to everyone who has favour on me in this scholar career.

Acknowledgement

Thanks are given to Allah for his guidance in the present work, and for all previous accomplishments as well.

I should then express my sincere gratefulness for my advisor Dr. Amale Mahi for all her appreciated help and assistance in this work. I would also like to thank my committee members, Prof. Amina Benkhedda, Prof. Abdelouahed Tounsi, Prof. Mohamed Bourada, Prof. Zouaoui Sereir and Dr. Mohamed Khodjet-Kesba for their willingness to evaluate my doctoral dissertation.

And certainly, I give my deepest gratitude and thankfulness to my mother and father for their great support and patience. Without their directions I would never have made it this far in life.

Table of Contents

List of Figures

LIST OF TABLES

List of abbreviations

AM	Additive manufacturing
CI	Ceramic isotropic (FGM with full-ceramic base matrix)
CM	Ceramic-metal (FGM with equal composition of ceramic and metal)
CNTs	Carbon nanotubes
CPT	Classical plate theory
CR	Ceramic-rich (FGM with ceramic-rich base matrix)
CUF	Carrera Unified Formulation
ESDT	Exponential shear-deformation theory
FGM	Functionally graded material
FSDT	First-order shear-deformation theory
GO	Graphene oxide
GPa	Gigapascal
GPls	Graphene platelets
HSDT	Higher-order shear-deformation theory
hHSDT	Hyperbolic higher-order shear-deformation theory
kg	Kilogram
m	Meter
μm	Micrometer
MR	Metal-rich (FGM with metal-rich base matrix)
nm	nanometer
SSDT	Sinusoidal shear-deformation theory
TSDT	Third-order shear-deformation theory

LIST OF SYMBOLS

a, b, and h	Plates dimensions
E	Elasticity modulus
ν	Poisson's ratio
ρ	Mass density
V	Volume fraction of ceramic in the base FGM
V_{GPl}	Volume fraction of GPls in the reinforced FGM
ϕ	Volume fraction of porosities in the reinforced porous FGM
$\overline{V}_{GPl}$	Average volume fraction of GPls in the reinforced FGM
P	Average volume fraction of porosities in the reinforced porous FGM
n	FGM power-law index
u, v	In-plane displacements of the FGM plate along the x and y axes
w	Deflection (in the z direction)
$f(z)$	Shear-deformation shape function
ϵ_{ij}	Strain tensor
σ_{ij}	Stress tensor
Q_{ij}	Elastic coefficient tensor relying the strain and stress tensors
A_{ij}	Extension stiffness coefficients
B_{ij}, B_{ij}^{a}	Bending-extension coupling stiffness coefficients
D_{ij} ,D_{ij}^{a}, D_{ij}^{aa}	Bending stiffness coefficients
A_{ij}	Transverse-shear stiffness coefficients
x , y , z	Rectangular coordinates of the plate
t	Time variable

General introduction

Subject of research

The wide application range of composite structures in the construction of important components in aircrafts and space shuttles, and the extreme mechanical stresses that these structures may experience in service, necessitates the use of reliable materials that can provide sufficiently high resistance and structural integrity. These requirements drive a continuous improvement of current material technology, and functionally graded materials (FGMs) are one of the latest chapters in this development series.

In this work we make a comprehensive treatment of the mechanical behaviour of porous FGM plates with GPls reinforcement. Our plate model consists initially of a metal-ceramic FGM matrix that varies in a continuous manner along the thickness direction according to two types of FGM power-law:

- In the vibration and bending analysis: the FGM varies from pure metal at the bottom surface of the plate to pure ceramic at the top surface according to the traditional power law, which gives a non-symmetric variation of elastic properties.
- In the buckling analysis: the power-law is modified to make a symmetric variation, where the FGM is metal-rich at the middle and gradually changes towards the surfaces to be completely ceramic.

This FGM matrix is reinforced by GPls, which are a recently discovered carbonaceous nanomaterial that takes the form of two-dimensional nano-sheets. Porosities are also included to simulate the defects of micro-scale voids that occur in many engineering materials, and which may be also introduced intentionally to reduce total weight, in addition to other benefits. Both parameters, ie GPls and porosities, may follow four different forms on non-linear distributions. In addition, the base FGM variation-profile and the overall proportions of metal and ceramic are adjusted by the value given to the power-law index.

Incorporating GPls into metal-ceramic FGMs was shown to yield very interesting results in these anisotropic materials, including increased effective modulus and stiffness coefficients, improved mechanical response, and more interestingly, the uncoupling of bending and extension in FGM plates. A visual abstract of the entire work is given in Figure 1. The results snapshots in the figure were obtained from our main article, which is introduced in the following section.

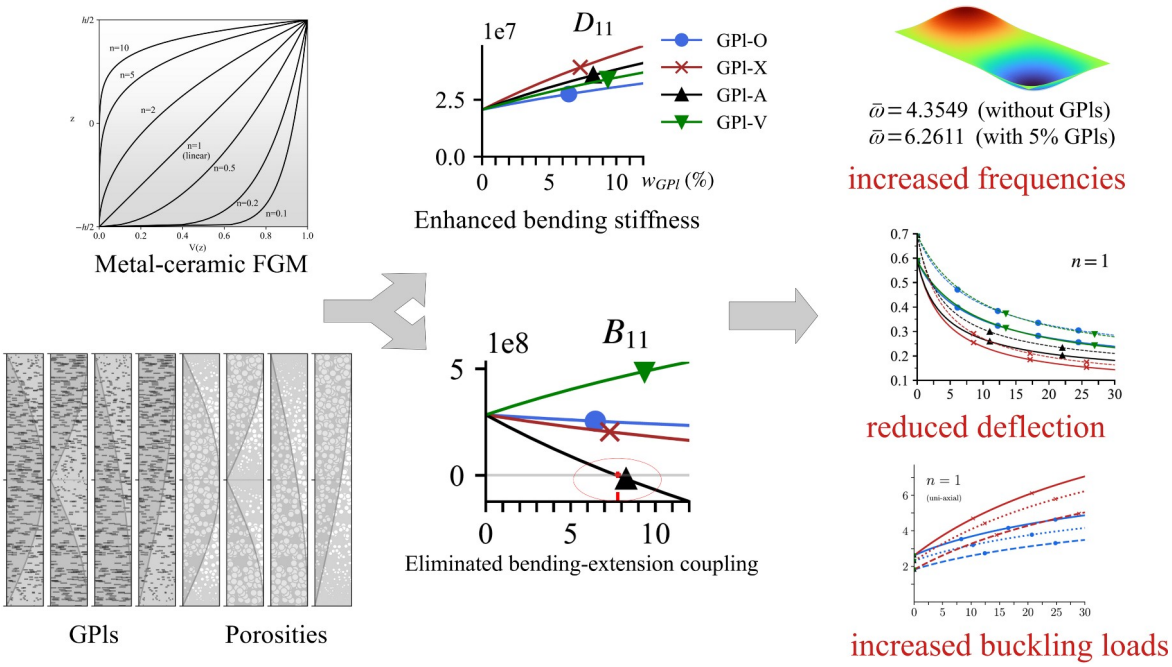

Figure 1: Visual abstract of the analysed parameters and findings of this work.

Scientific contribution

The recent FGM field has already reached a nearly mature stage of research, where an enormous works have been accomplished in all engineering aspects that relate to these materials. This includes the linear and non-linear mechanical responses [1], [2], thermal effects [3], integration of piezoelectric actuators [4], bio-medical applications [5], and many other research directions as well.

Despite these considerable research efforts devoted to FGMs, we have found that no previous work has attempted to analyse metal-ceramic FGMs with GPls inclusions, which was confirmed after careful search in multiple databases. Accordingly, we put our efforts on this line of research, which was eventually accomplished by the publication of our article entitled 'Effects of graphene-platelets reinforcement on the free vibration, bending, and buckling of porous functionally-graded metal-ceramic plates', in the Journal of Composite Materials, from Sage publications group [6].

In addition to this investigation, we have made a conference communication in ICARESS'22[1] [7] on the use of graphene and other nanomaterials in photovoltaic cells, which are considered from the mechanical perspective as composite panels without load-bearing capacities. This communication paper was chosen for

1 International Conference on Advanced Renewable Energy Systems, at UDES (Unité de Développement des Equipements Solaires), Bousmail.

publication in a national journal after the conference [8], which was done after paper improvement and extension. We have also contributed by a comparative study of different higher-order shear-deformation plate theories using a quasi-3D analysis, with application to the flexural response of metal-ceramic FGM plates. This work was communicated to ICMA'23[2] [9].

Our last contribution was the participation in the international conference ICCESEN-2023[3] by two papers. The first develops an analytical solution to the free vibration of GPls-reinforced metal-ceramic FGM beams with different boundary conditions [10], and the other investigates the effect of CNTs on the free vibration behaviour of FGM beams, also using an analytical method [11].

Organisation of the thesis

After setting an introductory background to the subject, I have organised the rest of the thesis as follows:

In Chapter I a comprehensive literature review was elaborated, focusing on the experimental state-of-the-art and mechanical analysis works of metal-ceramic FGMs, graded porous materials, and nano-reinforced materials. The production techniques and theoretical studies of each of these material types were categorized and explained thoroughly, with a special focus on most recent approaches.

Chapter II covers the theoretical modelling strategies and the various mathematical models used to represent metal-ceramic FGMs, nano-additives, and porosities. After that, kinematic plate theories and common solution approaches were discussed in detail.

The mathematical problem of interest is formulated in Chapter III, involving a rectangular FGM plate with porosities and GPls reinforcement. A unified displacement field that admits any desired plate theory was used. Then the principle of Hamilton was applied to derive the equilibrium equations, which were solved analytically by specifying the support type with the corresponding boundary conditions.

Chapter IV, which is the essential part of the thesis, exhibits the numerical results of a multi-parametric study of the free vibration, bending, and buckling of porous GPls-reinforced FGM plates. This chapter has a direct correlation with our article [6], from which some important results and conclusions were used to support our analysis. The influence of various parameters was examined and

2 International Conference on Mathematics and Applications, at Université of Blida 1, Blida.
3 10th International Conference on Computational and Experimental Science and Engineering, Turkiye.

discussed, including the composition of the FGM, the amount and distribution of GPls and porosities, and loading settings.

At the end of this work we report our findings and conclusions, and we propose a number of future recommendations to extend and enrich this FGM plates analysis.

Chapter I: State of the art of FGMs

I.1 Introduction

Functionally graded materials are advanced composites characterised by a graded variation in certain material parameters. This includes the composition of matrix materials, grains size, reinforcement particles, porosities, or any other material property. Also, the gradation pattern of a given FGM plays an important role in the mechanical characteristics of an FGM structures. All these parameter are set during the manufacturing stage. Besides, it is necessary to perform prior calculations to simulate the behaviour of the FGM models that we want to realize.

In this first chapter we review the state-of-the-art of FGMs in experimental and theoretical research, including the latest trends of 3D printing and the use of graphene and other nanomaterials for reinforcing FGMs. We also review and discuss the important simulation works on FGM structures.

I.2 Bibliographic research methodology

The bibliographic research was accomplished by using multiple scholar databases. Of which, the most useful to us was Scopus. We used the efficient search engine of this database with logic operators to refine results, and to exclude out-of-scope articles (like nonlinear FGM analysis in our research, see Figure I.1). Results were then sorted following two criteria: *Cited by (highest)*, and *Date (newest)*. Sorting articles by citations allows to obtain the most important works for research community, and citations are one of the best indicators of the value and quality of work (generally but not always, because citations are often manipulated and boosted, unethically).

On the other hand, sorting by recency allows to obtain the most up-to-date pieces of research. In this case, most recent works have few or even no citations at all, irrespective of how good or mediocre they are, which makes the selection difficult. Therefore, these works were filtered by personal judgement of the contribution to the field. Similar methodology was used in other databases like Proquest and Sage.

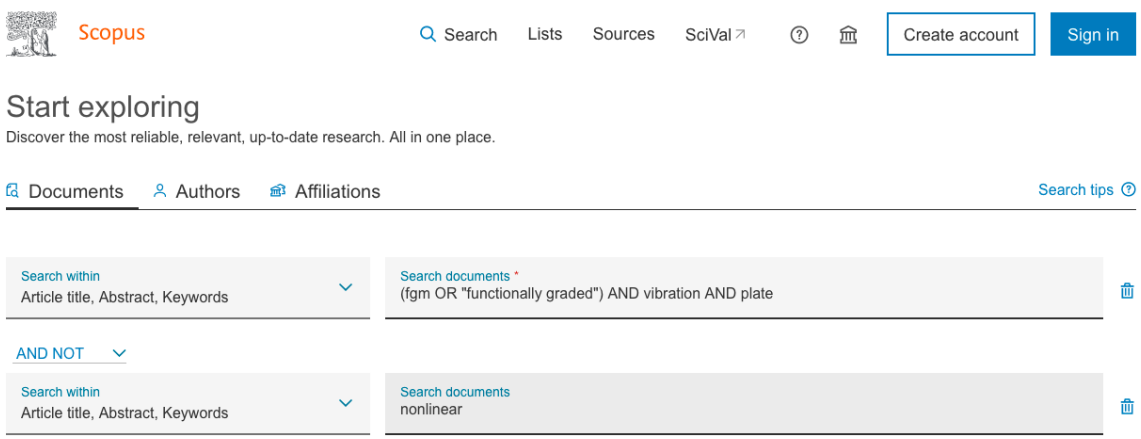

Figure I.1: Search interface in Scopus scholar database.

I.3 Fabrication techniques of FGMs

Fabrication phase is an essential part of composites research because it defines all the characteristics of the final product. Realizing FGM composites with the desired mechanical qualities requires good adjusting of material variation, controlling voids, and avoiding the formation of cracks and uneven shrinkage of different FGM layers due to varying material properties.

Despite the short existence of FGMs since their first proposition in 1983 to reduce thermal stresses in space vehicles [12], research community has accumulated a considerable amount of understanding on the properties and behaviour of these materials, and it can be considered now that these composites branch is almost as mature as that of laminates.

In this respect, FGMs fabrication techniques have followed a rapid curve of research and development, which was aided by the long experience in metallurgy and laminated composites, and also the gained knowledge from recent FGMs research. Many FGMs fabrication techniques exist today, but they all belong to three main classes, namely: deposition based methods, solid phase based methods,

and liquid phase based methods. Each class includes a family of different techniques, as it is shown in Figure I.2.

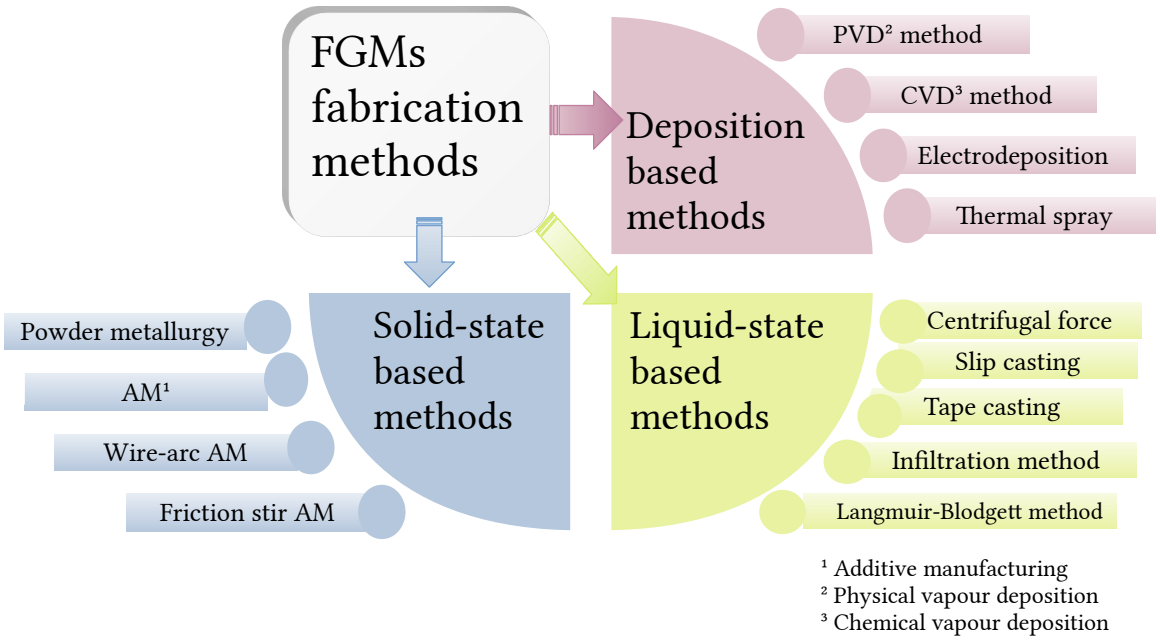

Figure I.2: Overview and classification of current manufacturing methods of FGMs.

The most common techniques from this chart are explained briefly bellow [13]:

- **Powder metallurgy:** this is an old technique based on materials powders that are compacted to give integrity, and then subjected to high temperatures but bellow the melting point (called the sintering process). In the case of FGMs, the constituents are stacked in the mould with grading proportions.
- **Centrifugal force:** this is a liquid-state method that is very popular in FGMs research. It allows to produce continuous FGMs by rotating a mould with high speeds, which generates a centrifugal force that drives heavier constituents outwards, creating a graded composition along the radial direction.
- **Vapour deposition methods:** in this methods the material is condensed from a vapour phase under high temperatures to solid layers that are deposited on a substrate. This method may be of physical or chemical type. We note that chemical vapour deposition can also be used to produce high quality graphene sheets [14].

- **Additive manufacturing (AM):** also known as 3D printing [15], this is a very advanced method that has many advantages over the other methods, such as the precise control of the composition and geometry in 3D space, the rapid printing speed that allows mass production, and the near-net forming character of the procedure, which reduces byproducts and wasted materials [16]. Some new hybrid methods that combine this method with other procedures were developed as well, such as wire-arc AM and friction stir AM.

Figure I.3 shows some recent FGMs realisations from these fabrication techniques. In Figure I.3(a) we see a 32-layered metallic FGM (Al-W), realised by Kelly et al. [17] using directed energy deposition, where W phase varies from 0% at the bottom layer to 55% at the top layer. In Figure I.3(b) we see an 8-layered metal-ceramic FGM (Ti-PSZ), fabricated by Fujii et al. [18] using spark plasma sintering (a powder metallurgy method), in which the FGM varies from full-ceramic to full-metal. In Figure I.3(c) we see a 5-layered metallic FGM (Cu-W), realised by Matějíček et al. [19] using thermal spray method. We can see that even though layers are few, the FGMs have nearly continuous variation. Also, we can observe by comparison that the more layers in the FGM, the smoother is the variation.

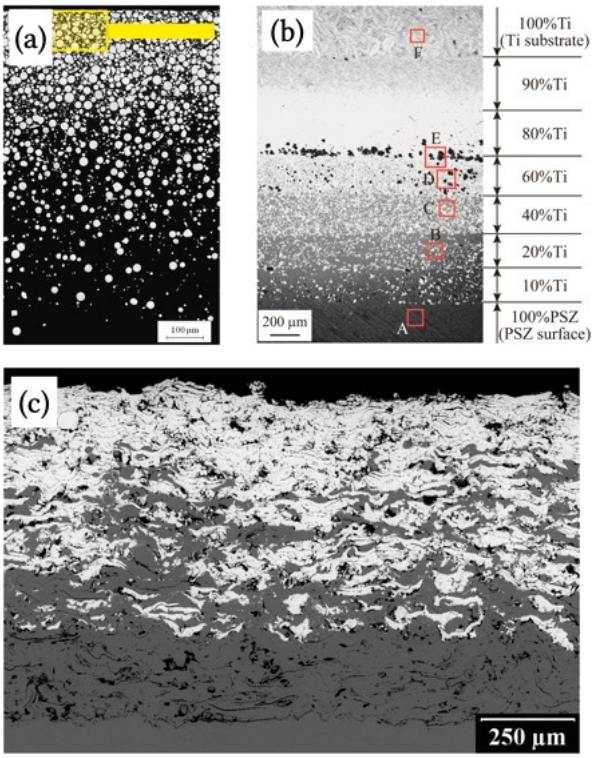

Figure I.3: FGM microstructures resulting from different fabrication techniques: (a) Al-W FGM realised using directed energy deposition (Al is the dark phase, and W is the white). Adapted from Kelly et al. [17]. (b) PSZ-Ti FGM realized using a powder metallurgy method. Adapted from Fujii et al. [18]. (c) Cu-W FGM realised using a thermal spray method (Cu is the dark phase and W is the white). Adapted from Matějíček et al. [19].

Continuous transition of material composition was demonstrated to in many recent FGM production techniques [13]. Even with discrete multilayered FGMs, quasi-continuous variation without abrupt changes in inter-laminar boundaries is observed, which is due to the thermal diffusion of materials at the interfaces of deposited layers [20]. The FGM gradation smoothness can be controlled by the number of layers as shown in Figure I.4 from Su et al. [20].

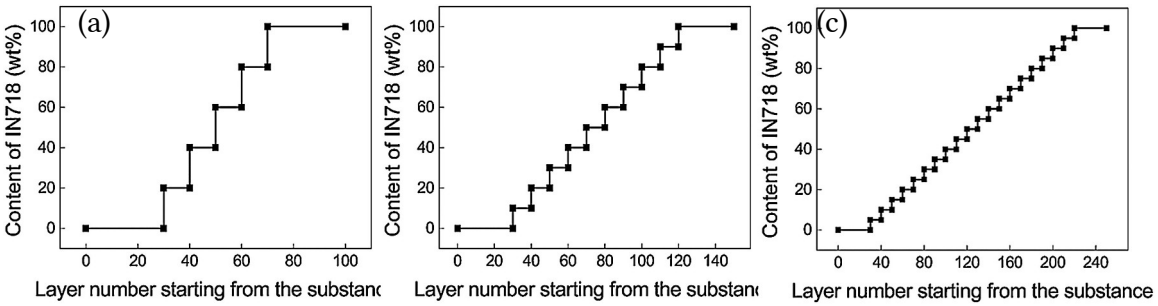

Figure I.4: Different transition modes of 316 L/Inconel718 FGM: **(a)** 5-layered FGM region. **(b)** 10-layers FGM region. **(c)** 30-layers FGM region. Adapted from Su et al. [20].

In this example, measurements of ultimate tensile strength and maximum elongation showed an increase between the 5-layers sample and the 10-layers sample, but deteriorated in the 30-layers sample because of heat accumulation associated with many deposited layers [**20**]. This negative effect may not necessary occur in all fabrication methods, especially with the most sophisticated ones like 3D printing.

The global elastic properties of entire FGM samples are determined in the same manner as with isotropic and composite materials (for example, using the usual tensile test). In addition to this, it is possible to obtain experimentally a layer-by-layer profile of elastic modulus using advanced inverse minimization methods combined with instrumented tests, such as micro-indentation tests [**21**] and four-point bending tests [**22**]. The results allow to visualize the through-thickness stiffness variation, and also to assess the accuracy of FGMs micromechanics models that estimate theoretically the effective properties.

I.4 Types of FGMs

I.4.1 Metal-ceramic FGMs

The most explored type of FGMs is the metal-ceramic FGM, which is designed primarily for thermal protection structures [12], [23]–[26]. Typically, ceramics are used at one surface (ie, an extreme FGM layer) for heat resistance and insulation, and metals are used at the other surface to provide structural rigidity, and the transition in between is made gradually according to specified profiles. Experimental and simulation results of these FGMs revealed good heat insulation, smooth temperature variation, and maintained structural integrity after prolonged thermal cycling. Material gradation in metal-ceramic coatings can also reduce the

amplitude of mode-I stress intensity factor under mechanical and thermal loadings [27].

Before FGMs, conventional duplex ceramic-metal thermal-barrier coatings had only two discrete regions of metal and ceramic, as shown in Figure I.5(a). The FGM coating improved these discontinued structures by making a graded intermediate layer (Figure I.5(b)). For the same coating thickness in this illustrated example, FGM coatings outperformed standard coatings by higher thermal insulation, longer lifetime under cyclic thermal loads and greater adhesion strength [28].

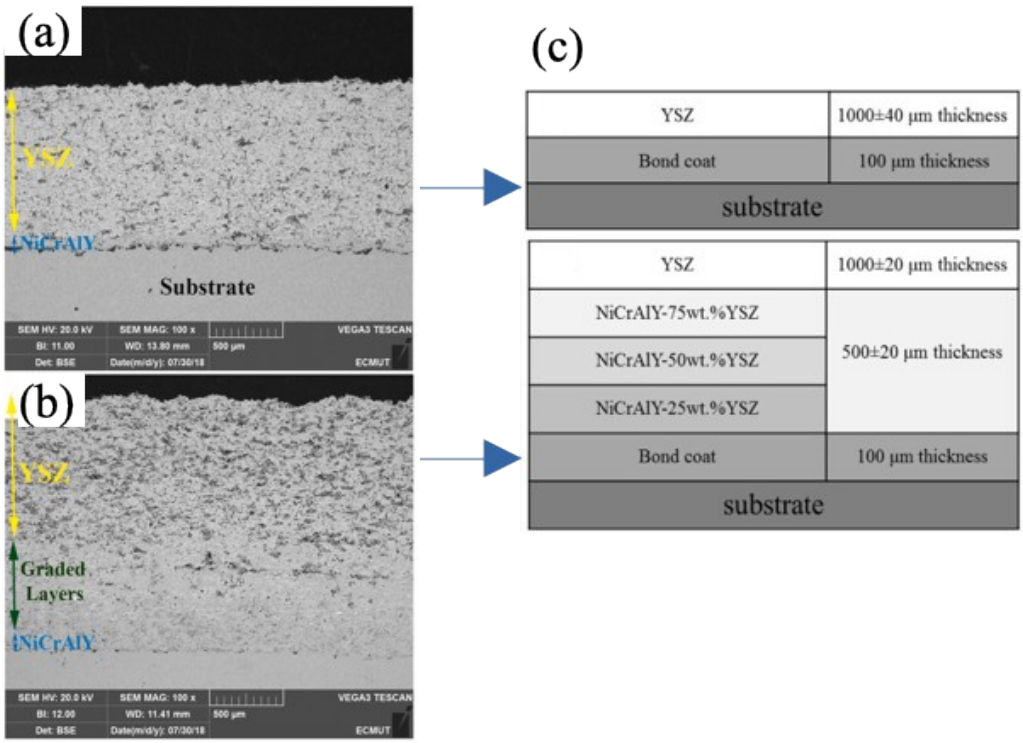

Figure I.5: Metal-ceramic thermal coatings: **(a)** traditional duplex type, where YSZ is the ceramic, and NiCrAlY is the metal alloy. **(b)** FGM type. **(c)** Composition scheme of both coating types for the same total thickness. Adapted from Mohammadzaki et al. [28].

In a similar study, Saeedi et al. [29] showed that thermal barrier coatings with an FGM YSZ-NiCrAlY layer had 1.5 times higher bonding strength than duplex thermal barriers, and also formed less cracks after thermal shocks [29].

In biological fields, metal-ceramic FGMs are efficiently used to reduce thermal stress in ceramic dental restorations, and to give higher strength and fracture toughness to artificial bones replacements [5], [30].

In terms of theoretical research of metal-ceramic FGMs, Yang and Shen [31] investigated the nonlinear free vibration and transient response of FGM plate with initial thermo-mechanical loads and temperature-dependant properties. The

authors found that the transient response of FGM plates does not necessary lie between those of isotropic ceramic and metal plates. Huang and Shen [32] made a similar study with heat conduction parameter, and concluded that the natural frequencies can be reduced by increasing the volume fraction index and temperature rise. Zenkour studied the statics [33] and buckling and dynamics [33] of sandwich FGM plate composed of metal core-layer bounded by two FGM layers using various higher-order shear-deformation theories (HSDTs). Li et al. [34] made a three-dimensional analysis of vibrating FGM plates under thermal loadings. The solution was performed using the Ritz method and the displacements were expressed by Chebyshev polynomials. Qian et al. [35] analysed the statics and dynamics of FGM plates using a normal-deformable HSDT and a meshless local Petrov–Galerkin method for the solution. It was found that the deflection magnitude is not symmetric about the mid-plan for both FGM and isotropic plates. Han et al. [36] used a four-variables third-order HSDT to analyse the dynamic stability of sigmoid FGM plates under periodic in-plane excitation loads. It was found that the instability region increases with the values of elastic foundation parameters. Huang et al. [37] investigated the vibration of FGM plates with cutouts situated at different positions and with various sizes using the finite elements method (FEM). Lahdiri and Kadri [38] analysed the vibration of FGM porous plates with different geometric forms and multi-directional material gradation using an isogeometric approach. Nguyen et al. [39] developed a semi-analytical analysis of corrugated cylindrical FGM shells without or full of fluid and under dynamic loads. The solution was calculated using the fourth-order Runge–Kutta method, and it was revealed that vibration amplitudes of corrugated FGM cylinders are substantially reduced from those of non-corrugated FGM cylinders with the same material quantity.

I.4.2 Porous FGMs

Porous materials are commonly used in aerospace and transportation industries because these fields emphasize on structural weight and also on minimizing the consumption of material resources. A genius way for these objectives is to introduce microscale air voids into the material, or porosity. Porous materials trade a percentage of the original mechanical properties for the gained benefits. However, this loss is often compensated-for by thermal treatment procedures [40], or by reinforcing materials [6]. The current research direction in porous materials is the graded porosity, which was shown to outperform uniform-porosity materials by many researchers [41]–[43].

Different techniques exist to introduce porosities into engineering materials. A long-standing technique consists of casting the liquid material around granules or

hollow spheres of low density, called *space holders* or *pores-forming agents*. These granules may be of inorganic origin like alumina [40] or organic origin like starch [44], [45], and they will eventually burn out by the heat of the procedure to leave spherical pores in place.

The size and density of pores can be controlled by adjusting the beads-size and the volume-fraction of pores-forming agents [43], [46]. Figure I.6, reproduced with modification from the work of Vemoori et al. [46], illustrates how pores-forming agents (polystyrene beads here) can be used to adjust the characteristics of porous ceramic. Pores mean-diameter is adjusted through beads size, and pores density is adjusted through beads volume-fraction. These parameters affect directly the median wall-thickness of cells, which plays a principal role in the mechanical resistance of cellular materials [46].

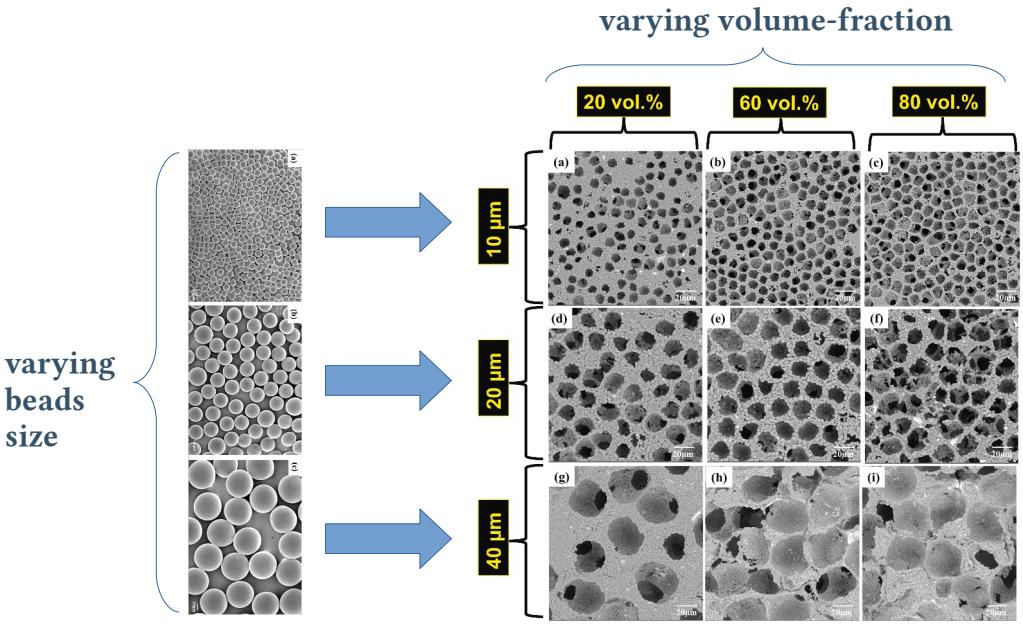

Figure I.6: Controlling pores size, density, and wall-thickness of cellular ceramic by varying the parameters of pores-forming agents. Adapted from Vemoori et al. [46].

It is also possible to realize lamellar-shape voids in centrifugal techniques, where the matrix material is pushed outwards by high-speed rotation of the mould, leaving more void spaces in the inner region [47]. This technique has the advantages of not requiring pores-forming agents, and the automatic creation of porosity gradient in the radial direction.

Additives manufacturing of porous materials is much investigated given the accuracy of this technique in adjusting pores distribution in the space. In this respect, Bin Liu et al. [42] developed a procedure to control porosity field in additively-manufactured FGMs, which allows consequently to tailor the elastic

modulus distribution in 3D space [42]. This method was demonstrated in polyurethane samples, in which the elastic field was adjusted according to pre-defined equations that were integrated in the process system (see Figure I.7).

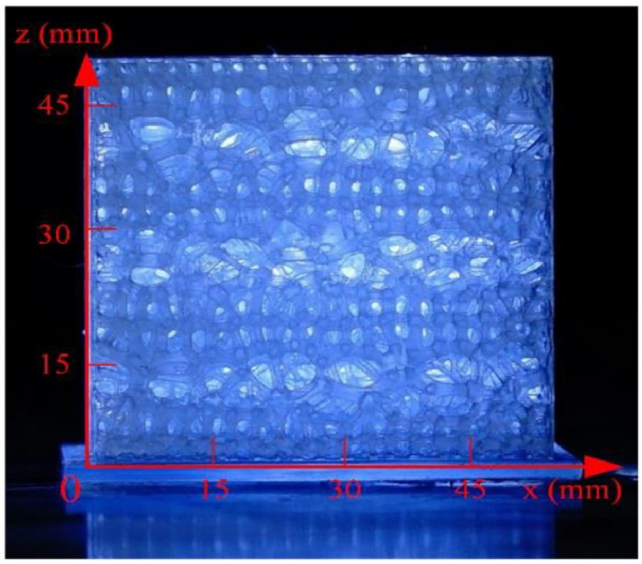

$$E(x,y,z)=\begin{cases}0.09 & z\in[0,5)\cup[15,20)\cup[30,35)\cup[\\ 0.025 & z\in[5,15)\cup[20,30)\cup[35,45)\end{cases}$$

Figure I.7: Designing graded elastic field of polyurethane using pre-defined 3D-printing rules. Adapted from Bin Liu et al. [42].

Coffigniez et al. [48] developed a new 3D-printing method to control porosity in metal scaffolds (i.e tissues) by using the size of extruded metal powder. Figure I.8(a) shows a titanium-alloy scaffold realised by this approach, and Figure I.8(d)-(f) shows the graded porosities in the printed filaments of this scaffold.

In addition to these engineered porosities, another type of pores may occur unintentionally in the material. Figure I.8(c) shows an instance of these accidental pores (marked by red arrows). These pores are generally undesired as they make detrimental discontinuities in the material.

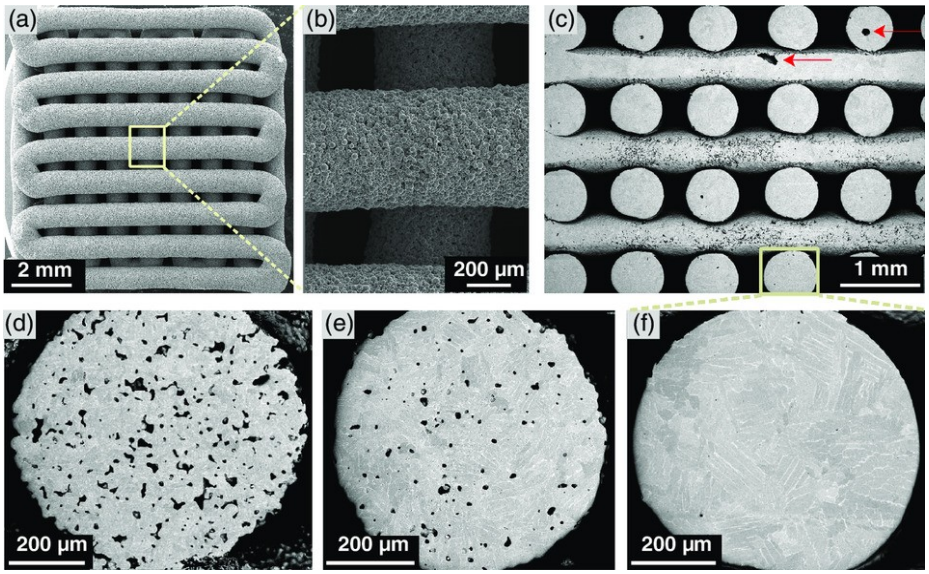

Figure I.8: Microscopic images of a 3D printed Ti-6A-4V porous scaffold. **(a)** Tissue filaments. **(b)** zoomed inset. **(c)** accidental pores highlighted. **(d)-(f)** porosities gradation between different filaments. Adapted from Coffigniez et al. [48].

Graded porosity was shown to delay the compressive failure in metal-foams, which is due to the gradual collapsing of different layers instead of uniform collapsing at once in the case of homogenous porosity [43]. Similar improvements in compressive strength with graded porosity were obtained in porous ceramics [41], metal-lattice structures [49], [50], and porous polymers [42].

I.4.3 Graphene and nanomaterials-reinforced FGMs

Improving the physical properties of composite materials by nano-additives is a subject of extensive research in various fields. Graphene, in particular, is a very interesting nanomaterial because of its high elastic modulus of $\sim$1000 GPa, which makes it the strongest nanomaterial [51]. Steel for comparison –one of the strongest engineering metals– has a modulus of $\sim$200 GPa. Graphene is a two-dimensional carbon-based nanomaterial with a hexagonal atomic lattice. It is often incorporated in the form of graphene nanoplatelets, or graphene oxide (GO).

Theoretical research on the effects of GPls addition to the flexion, buckling, and vibration of FGM plates is only in its first stages. Not long ago, Song et al. [52] initiated this direction in 2017 by studying the free and forced vibration behaviour of GPls-reinforced polymer plates using the first-order shear-deformation theory (FSDT). Wu et al. [53] presented a parametric study on the buckling and free vibration of multi-layered FGM GPls-reinforced plates subjected to periodic in-

plane forces and uniform temperature rise. García-Macías et al. [54] conducted a comparative analysis of the bending and vibration of polymer plates reinforced by GPls or by carbon nanotubes (CNTs), and used an FEM simulation with consideration of GPls orientation and agglomeration defects. The stiffening effect of GPls was found to be superior than that of CNTs for the same additives content. Yang et al. [55] investigated the impacts of porosities and GPls on the buckling and dynamic behaviour of metal-matrix multi-layered plates using the FSDT and the Chebyshev-Ritz solution method. Zhao et al. [56] investigated the vibrations of thick porous FGM plates using the three-dimensional elasticity theory and the Rayleigh-Ritz solution method. Pashmforoush et al. [57] conducted a statistical analysis of the dynamic response of isotropic plates reinforced with graded GPls. It was found that boundary conditions and GPls volume-fraction were the most influencing parameters affecting natural frequency, followed by thickness ratio and GPls distribution modes, respectively. Thai and Phung-Van [58] solved the free vibrations problem of FGM GPls-reinforced plates with circular or complicated holes using the moving-Kriging meshless method and a special integration scheme. Nguyen et al. [59] used an isogeometric solution for the vibration and buckling of GPls-reinforced FGM porous plates using a refined three-variables HSDT. The forced vibration and resonance of metal-foam laminated plates reinforced with GO were studied by Zheng et al. [60] using Galerkin method. Van Do and Lee [61] examined the nonlinear thermal buckling and post-buckling responses of GPls-reinforced laminated epoxy plates under different kinds of thermal loadings using an isogeometric approach. Sheikholeslami et al. [2] made a non-linear analysis of doubly-curved GPls-reinforced micro-panels with double curvature under non-uniform thermal loadings.

We have recently treated the free vibration, bending, and buckling of porous metal-ceramic FGM plates reinforced by GPls [6]. We found that the relative change of frequency due to GPls varies significantly with the composition of the base FGM, while the change due to porosities is nearly unaffected by varying the FGM. It was also demonstrated that GPls and porosities have marked effects on the bending-extension coupling of FGMs [6].

CNTs, which are graphene's uncle, are another important carbonaceous nanomaterial that is widely investigated in composites research. Salama et al. [62] fabricated a radially-graded aluminium-CNTs FGM (showed in Figure I.9). The FGM behaved like a bulk material without delamination of layers under loads, and showed an increase in the ultimate tensile strength by 107.1% with respect to pure Al samples, and by 10% with respect to uniformly-dispersed CNTs sample. Daikh et al. [63] studied the free vibration, bending and static stability of FGM polymer plates reinforced by CNTs with consideration of nonlocal elasticity theory. A

quasi-3D formulation was used with Galerkin solution method. It was found that the introduction of nonlocal parameter leads to a decrease of calculated plate stiffness, which consequently decreases buckling loads and frequencies, and increases deformations.

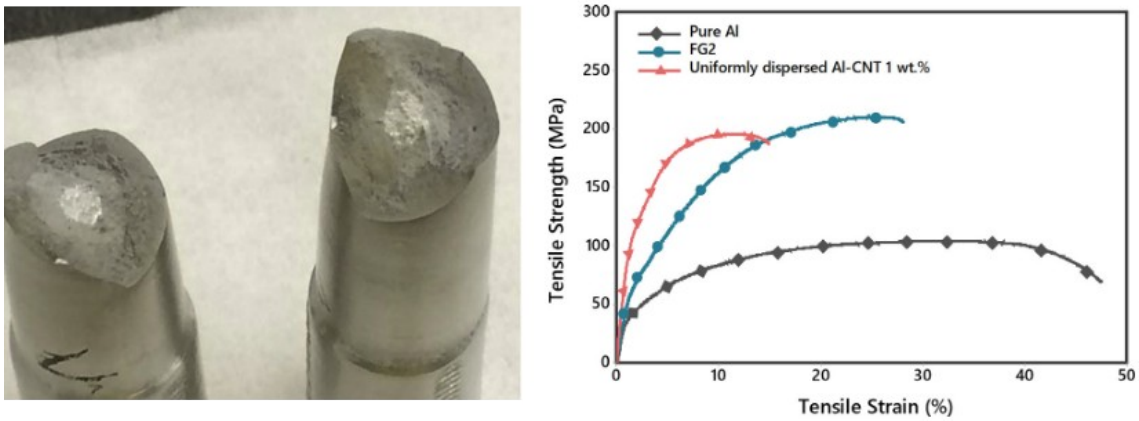

Figure I.9: Al-CNTs FGM sample. Left: fractured sample after tensile test. Right: stress-strain diagrams from tensile test, in which FG2 (the FGM sample) has equivalent CNTs content to uniform dispersion samples. Adapted from Salama et al. [62].

Adding nano-clay particles and nano-silica particles to reinforced glass/epoxy composites can decrease the coefficient of hygroscopic expansion by 17% and 23%, respectively, which improved the dimensional stability of epoxy composites under corrosive environmental conditions [64].

I.4.4 Other types of FGMs

In addition to the common FGM types discussed above (metal-ceramic FGMs, porous FGMs, and particles-reinforced FGMs), some other types of graded cellular materials are also attracting researchers' interest. Traditional honeycomb composites, for instance, have a large room of development using the FGM idea. These materials consist of two thin but rigid skins sandwiching a soft core. This core occupies most of the honeycomb thickness, and it is characterized by a unit cell that repeats in 2D patterns. Density gradient was shown to be an effective means for enhancing the energy absorbing properties and damping in honeycomb materials [65].

Lattice structures are also another area in which the FGM concept is being integrated. Lattice materials consist of ordered cellular patterns that repeat in the 3D space (in contrast to honeycomb materials). The reduced elasticity moduli of lattice materials compared to highly stiff alloys makes them very suitable to be used as orthopaedic materials and avoid the "stress shielding" effect in

conventional alloy implants [66]. FGM lattices are realized using advanced AM printing procedures that allow to realize gradients with many possible geometric parameters. FGM lattice structures with a gradient along the loading direction showed optimal mechanical results, with and increase in elastic modulus by 17.53% and by 59.43% in energy absorption capacity (compared to uniform-lattice) [49]. Figure I.10 shows some examples of honeycomb and lattice FGMs from very recent experimental studies.

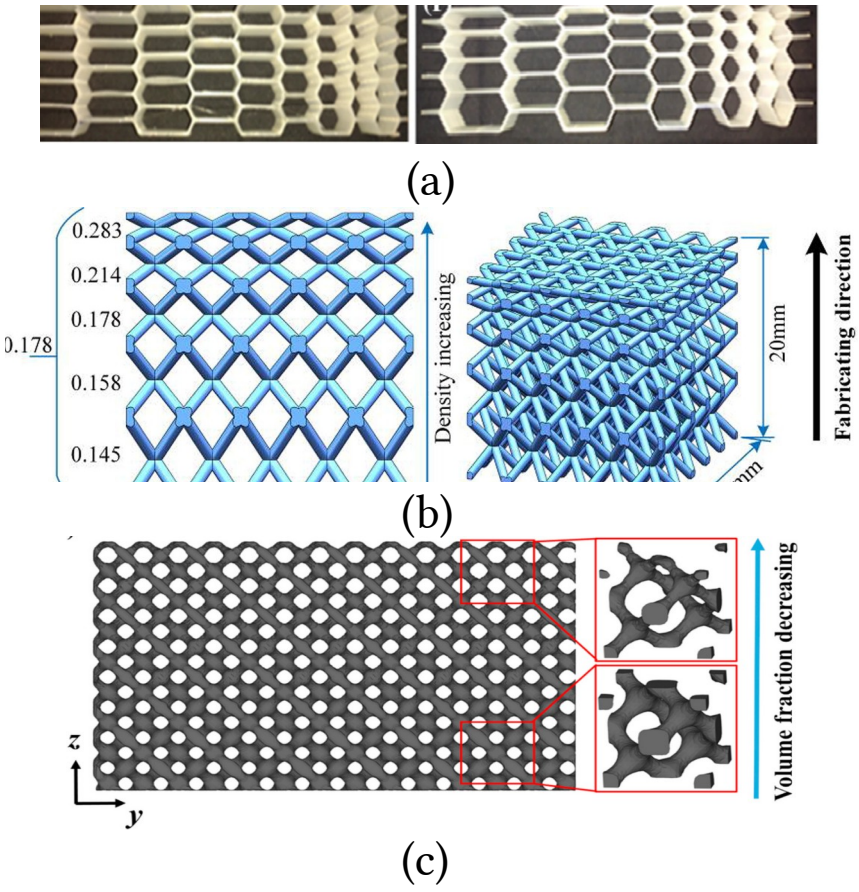

Figure I.10: Cellular FGM structures. **(a)** honeycomb with length grading (left), and hybrid height-length grading (right). Adapted from Sahu and Sreekanth [65]. **(b)** FGM lattice with grading in cell-size. Adapted from Bai et al. [49]. **(c)** FGM lattice with grading in both cell-size and structs diameters. Adapted from Yang et al. [50].

FGM Research is also beign applied on polymeric composites, which are a widely-used materials in aeronautical industry. Graded fiberglass laminates demonstrated higher flexural capacity and better resistance to sliding wear in comparison to conventional laminates [67]. Joining polymer matrix composites by FGM adhesives was shown to reduce the peel stress and facilitate the realization of lighter aircrafts structures, in contrast to heavy rivet-type joints [68].

Chapter II: Modelling and solution approaches of FGM structures

II.1 Introduction

The purpose of this chapter is to investigate the theoretical models used by researchers in the linear elastic analysis of FGM plates that we study specifically in this thesis. The first part of the chapter presents the material models applied to each of metal-ceramic FGMs, nanomaterials-reinforced composites, and porous composites. Then, the important models of shear-deformable plate theories are explored with their various applications in the FGM field. And finally we review the solution methods applied to FGM plates problems.

II.2 FGM constitutive models

The physical properties of solid multi-phasic media, and in particular FGMs, are modelled by homogenization –or micromechanical– models, which aim to calculate the effective properties of these mediums by considering the effects of microstructures and the properties of individual phases and their interactions. Micromechanics represents an important part of the mechanical analysis of composite materials, because the results depend essentially on the estimated elastic moduli.

In the following sub-sections we will review the most common models used to model FGM material properties. Given that our analysed FGM plate is composed of a base metal-ceramic matrix, GPls inclusions, and porosities, then each of these parameters is treated apart.

II.2.1 Modelling metal-ceramic FGMs

Modelling the metal-ceramic FGM matrix is done in the most part of the literature by the simple rule of mixture, also known as the Voigt model [69]. This

rule estimates the effective elastic property as a linear sum of phases properties weighted by their respective volume-fractions. Accordingly, the effective elastic modulus E and Poisson's ratio ν are calculated as:

$$\begin{aligned} E_{mat} &= E_m V_m + E_c V_c \\ \nu_{mat} &= \nu_m V_m + \nu_c V_c \end{aligned} \tag{II.1}$$

where *mat* denotes matrix, *c* denotes ceramic, and *m* denotes metal.

Mori-Tanaka homogenization model is also widely used to estimate the elastic properties in the case of a two-phases FGM material having a base-matrix with randomly distributed inclusions. This model expresses the effective shear G and bulk K moduli as:

$$\begin{aligned} G(z) &= G_m + \frac{V_i}{\frac{1}{G_i - G_m} + \frac{6(K_m + 2G_m)(1 - V_i)}{5G_m(3K_m + 4G_m)}} \\ K(z) &= K_m + \frac{V_i}{\frac{1}{K_i - K_m} + \frac{3(1 - V_i)}{3K_m + 4G_m}} \end{aligned} \tag{II.2}$$

Where subscripts m and i denote the matrix and particles inclusions, respectively. The elastic modulus and Poisson's ratio are then obtained from equation (II.2) by the relationship:

$$\begin{aligned} E(z) &= \frac{9G(z)K(z)}{G(z) + 3K(z)} \\ \nu(z) &= \frac{3K(z) - 2G(z)}{2(G(z) + 3K(z))} \end{aligned} \tag{II.3}$$

A question arises in the Mori-Tanaka model as to which phase in the FGM to consider as the matrix and which one to consider as the inclusion, because the FGM varies from metal-rich with little ceramic as inclusions, to ceramic-rich with little metal as inclusions. Vel and Batra [70] used a combined technique for this case, where they considered the bottom and top regions of the FGM as a particulate microstructure with ceramic and metal as inclusions, respectively, and a middle region with skeletal microstructure (see Figure II.1 for illustration). In the top and bottom regions the Mori-Tanaka model was used, and in the skeletal region a self-consistent model was used.

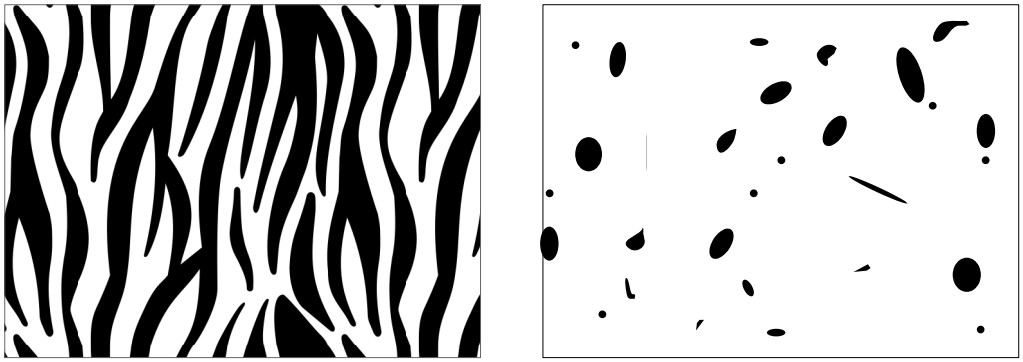

Figure II.1: Two-phases composite material with **(a)** skeletal microstructure, and **(b)** particulate microstructure.

Ferreira et al. [71] analysed FGM plates modelled using either the rule of mixture or the Mori-Tanaka homogenization technique. The authors found that when Poisson's ratio of the two phases has very similar values, the two techniques give close values, but the results will diverge significantly for largely different ratios.

Other micromechanical models exist for the calculation of elastic properties, such as the Tamura model and the cubic local representative volume elements model [72], but are less used because of the increased complexity.

As for the effective mass density, it is always calculated using the rule of mixture, irrespective of the adopted model.

The variation profile of the FGM is controlled by the function $V(z)$. This function has been often described by adopting a convenient power-law function, given as:

$$V(z)=\left(\frac{z}{h}+\frac{1}{2}\right)^{n} \tag{II.4}$$

Researchers have worked with many other functions as well, such as sigmoid rule [11], [36] and exponential rule [9], [73], [74]. In effect, any valid mathematical expression can serve the same purpose as these functions. Thus, the FGM can be tailored to a given application by specifying the profile of gradation to suit the design requirements.

II.2.2 Modelling the effects of porosity on FGMs

The most simple model of porosities is the modified rule of mixture, which is widely used to determine the elastic properties in metal-ceramic FGMs [38], [56], [75]–[79]. The rule of mixture assumes a linear decrease of elasticity modulus with porosities, but this assumption is only valid for very small amounts of porosities [80], [81]. Also, Abuteir and Boutagouga [3] have recently revealed that the mathematical expression of this modified rule of mixtures is physically inconsistent.

On the other hand, the Gibson-Ashby models are used to obtain the elastic properties of porous metal foams FGMs. Two Gibson-Ashby variants are used: the model of open-cells cellular solid (for example in [55]), or that of closed-cells cellular solid (for example in [59]). Jalali et al. [82] have recently reported that the open-cells model was wrongly simplified in 86 recent papers, which led to significantly overestimated elastic modulus, and consequently in large errors in deflections and frequencies.

There exist a simpler and more accurate exponential relation of porosities proposed by Pabst and Gregorová [80], [83]. The higher accuracy of this model over the others, including Gibson-Ashby models, was confirmed by experimental measurements of elastic modulus [84] and by computational micro-structures simulation [85]. In our article on porous GPls-reinforced FGMs [6], we have adopted this exponential model and showed that it gives very realistic results. Specifically, the natural frequencies will decrease with higher porosities irrespective of their distribution, which is a physical consequence of the reduced stiffness. On the other hand, the linear rule-of-mixture may lead to increasing frequencies with porosities amount [6].

II.2.3 Modelling the properties of nanomaterials-reinforced composites

Evaluating the mechanical properties of composites with nanomaterials inclusions is a challenging task, because of the hierarchical structures of nanoparticles which is not limited to the nano-scale only. For example, graphene nanosheets are of the order of nanometers along the thickness, but the other two dimensions may be few micrometers long. Numerous models were developed for an accurate representation of nanomaterials-reinforced composites with more focus on elastic properties, as they are directly involved in the static and dynamic analysis of these structures. The following strategies are used for modelling nano-additives in composite materials, classified from the simplest to the most complicated [86]:

- **Micromechanical models:** these are the most used models in FGMs research because of their closed-form explicit expressions. These models make use of Cauchy's continuum mechanics to represent the matrix and nano-additives without considering nanoscale interfacial interactions. In the case of GPls-reinforced FGMs, the Halpin-Tsai homogenization [87] model is usually used. Improved Mori-Tanaka models are also utilized with consideration of interface and agglomeration defects [88], [89].
- **Nanostructural modelling:** this approach represents a more elaborated strategy which attempts to considers the morphology of nano-additives at the nanoscale while keeping the hypothesis of continuity like micromechanical models. Nanostructural modelling offers more precise insights on the nanomaterial-matrix interface interaction without loosing much simplicity.
- **Molecular modelling:** this is the most accurate strategy as it considers three modelling scales: the atomistic model, nanostructural model and micromechanical model. This approach abandons the continuity hypothesis to consider only discrete theories, which gives very realistic results, but at the expense of a very high computational penalty. Molecular dynamics is a very popular method in this type of modelling [90].

II.3 FGM plates theories

Plate structural elements are widely used in many industry, and they are fabricated in various shapes and compositions. In aeronautical structures particularly, plate and plate-like structures compose tailplanes, winglets, and control surfaces (see Figure II.2 for illustration). The various applications of plates in engineering have made them extensively studied by researchers and engineers to optimize their material and geometric attributes and enhance their mechanical performance.

Figure II.2: Control surfaces exemplify well the use of plates structures in aeronautical engineering. Wing of Boeing 767-324. Image from www.airliners.net.

Therefore, many plates theories have been proposed since the early works of Kirchhoff and Love in the 19 th century [91] on isotropic plates with many simplifying assumptions, to the recent developed models of shear-deformable plates with nonlinearity and non-local effects. The main goal in the field of plates modelling is to describe their mechanical behaviour with sufficient accuracy and with reduced computing costs compared to the exact –but complicated– elasticity solution. The most important characteristics in the elastic mechanical analysis of plates are: the state of stresses and strains, natural frequencies, and critical buckling loads.

Despite the huge number of plates theories out there, the difference between two theories lies in four essential points:

- **The type of variables:** the most common approach is to assume a displacement field that satisfies the boundary conditions of the plate. Alternatively, some researchers prefer to start with an assumed stress field and derive the equations of motion, or with combined stress and displacement fields. We will focus on the first approach as it is conventional now in plates modelling.

- **The number of variables:** the literature review reveals that most HSDTs use a five-variables kinematic model (three displacements and two rotations). A four-variables formulation is also very common (using four displacements).
- **The shape function:** this parameter determines the variation of transverse shear stresses and strains across the thickness. The choice of this function becomes very important for thick plates, which exhibit more influence of transverse shear effects.
- **The assumption on normal transverse deformation (stretching):** theories that consider this effect are called quasi-3D theories, and are mainly used for large thickness ratios. On the other hand, 2D formulations are based on the assumption of plane elasticity without stretching, and are deemed accurate for most practical engineering problems.

II.3.1 Shear-deformation plate theories

The simplest plate model is the classical plate theory (CPT), also known as thin plates theory, or Kirchhoff plates theory. CPT is the plate equivalent of the classical Euler-Bernoulli beam theory, and it has served engineers from the times of manual calculation of mathematical tasks to recent days where it is used in FEM formulations for its computational simplicity. However, the CPT totally neglects transverse shear stress and strain, which leads to inaccurate results in moderately-thick and thick plates.

Shear-deformation theories were then proposed with consideration of these transverse shearing effects. First by Reissner [92], [93], who derived the governing equations in function of the variables V_x and V_y (transverse shear resultants) and deflection. Mindlin [94] then proposed the first-order shear-deformation theory (FSDT) with the following displacement field:

$$\begin{aligned} u(x,y,z) &= u_0(x,y) - z\, w_{0,x} \\ v(x,y,z) &= v_0(x,y) - z\, w_{0,y} \\ w(x,y) &= w_0(x,y) \end{aligned} \tag{II.5}$$

Where u_0 and v_0 are membrane extensions at the mid-plane level, and w_0 is the deflection. The FSDT results in a uniform shear stresses distribution along the thickness (σ_{xz} and σ_{yz}), when they should vary quadratically. This uniform variation also means that the zero transverse shear boundary condition at the top and bottom surface of the plate is not satisfied. Mindlin introduced a shear correction factor of $k = \pi^2/12$ to adjust the erroneously calculated shear

resultants, but the distribution of transverse shear strain and stress remains incorrect[4], and this error has more impact in thicker plates. Timoshenko [95] defined this factor as the ratio of the average shear strain on a given section to the shear strain at the geometric centroid of the cross section of a beam. Physically, the true value of this factor is a function of cross-sectional shape, Poisson's ratio, material properties and boundary conditions, and it is harder to determine for laminated structures than single-layered ones [96]. Reissner [92], [93] introduced factor of $k = 5/6$, which is numerically close to that of Mindlin.

It should be noted that the widespread naming of the 'Reissner-Mindlin theory' is incorrect because the two theories are fundamentally different. Reissner's theory assumes quadratic transverse shear stresses, and results in non-zero thickness extension (stretching). In contrast, Mindlin's FSDT leads to constant transverse shear stresses and zero thickness extension. Wang et al. [97] established the relationships between the corresponding quantities of these theories and has carried out numerical comparison for the same correction factor. Mota et al. [75] showed recently that the actual value of this factor varies largely between FGM power indices, and that it also changes with porosity amount and distribution. Figure II.3, adapted from the same source, demonstrates the deviation of the shear correction factor of various FGMs from the constant value set by Reissner in function of porosity volume ratio (modelled by the modified rule of mixtures).

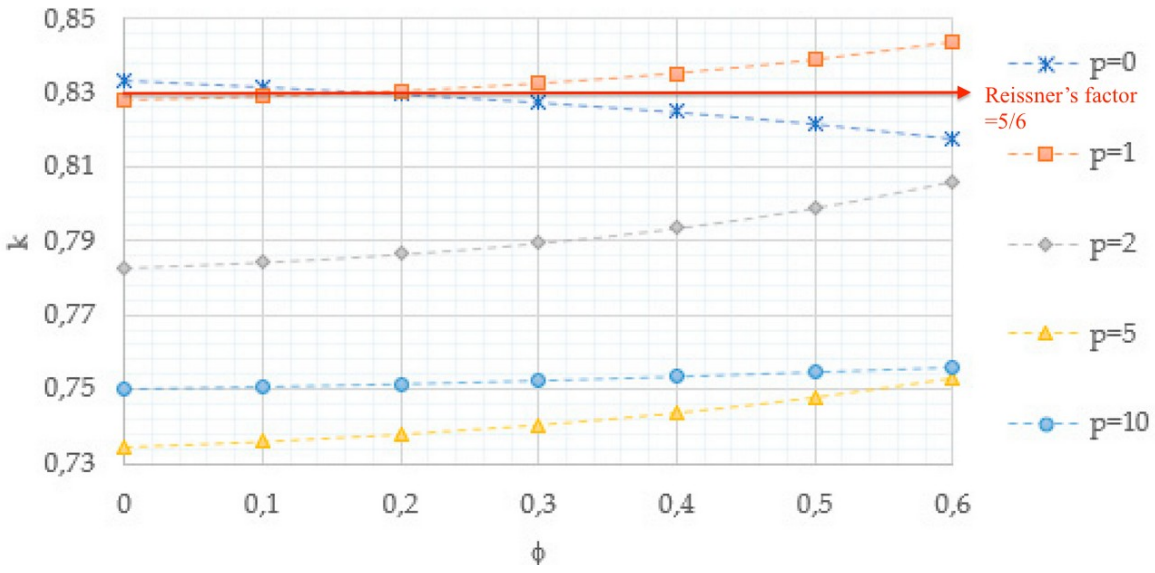

Figure II.3: Variation of the actual value of shear correction factor for different FGM power indices with respect to porosity ratio ϕ. Adapted from Mota et al. [75].

4 This mistake of the FSDT will be seen in the bending section of results chapter.

Shimpi et al. [98] proposed two FSDT models with two variables. The displacement fields of these FSDT variants are given as:

$$\begin{aligned} u &= -z\,\frac{\partial w_b}{\partial x} \\ v &= -z\,\frac{\partial w_b}{\partial y} \\ w &= w_b + w_s \end{aligned} \tag{II.6}$$

or:

$$\begin{aligned} u &= -z\,\frac{\partial \phi}{\partial x} \\ v &= -z\,\frac{\partial \phi}{\partial y} \\ w &= w_0 \end{aligned} \tag{II.7}$$

It can be seen that this work neglects in-plane displacements u_0 and v_0, which is not justified in many cases of plate analysis. For instance, the magnitudes of u_0 and v_0 become significant when there is coupling of in-plane and out-of-plane motions, which occurs in FGM plates with material asymmetry [6]. Rezaei et al. [99] used the refined FSDT of equation (II.6) with in-plane effects to analyse the vibration of porous FGM plates. The equations of motion were decoupled by algebraic procedure to obtain one single final equation. Bellifa et al. [100] used the refined theory of equation (II.7) with membrane contributions to analyse the bending and vibration of FGM plates. The authors used the neutral surface concept which uncoupled the equations of motion.

Mindlin's theory was later implemented in numerical methods to solve plates problems, like the FEM [24], [26], [101]–[105], meshless numerical methods [106]–[108], differential quadrature methods (DQM) [109]–[111], and the discrete singular convolution method[5] [112]–[114].

A number of other researchers have proposed FSDTs with integral terms instead of derivative terms as follows:

$$\begin{aligned} u &= u_0 - z\ k_1 \int \phi\,(x,y)\,\mathrm{d}x \\ v &= v_0 - z\ k_2 \int \phi\,(x,y)\,\mathrm{d}y \\ w &= w_0 \end{aligned} \tag{II.8}$$

5 Singular convolution method is a recent numerical method, developed in 1999 for fast and effective solving of mathematical physics problems.

This approach was used by Mantari and Granados [115], [116], and then it was extended to quasi-3D FGM HSDTs by Abualnour et al. [1] and Zaoui et al. [117].

Kienzler and Schneider [118] developed a second-order plate theory starting from the three dimensional equations of elasticity and without any kinematic assumptions. They found that their proposed theory coincides with Reissner's theory [92], [93]. Second-order shear-deformation theories are not developed and used as much as the FSDT, mainly because of the insignificant gain in accuracy over the FSDT [119].

As the FSDT makes faulty description of transverse shear variation, some researchers have tried to modify it in order to ameliorate this aspect. Tati [120] developed an improved FSDT model by imposing a parabolic variation of transverse shear stresses and including the stretching effect in the displacement field. He used this theory in a FEM analysis of FGM plates bending. A similar FEM approach was used by Vinh et al. [76] to analyse the buckling and bending of porous FGM plates.

Higher order shear-deformation theories were then developed to reflect a parabolic variation of transverse shear, which gives more realistic results for the mechanical behaviour. The term *higher order* was used initially to indicate that the displacements varied along the thickness following polynomials of order higher than the first [121], and then this designation was extended to non-polynomial plate theories. The displacement field of a general two-dimensional HSDT contains higher-order terms in the in-plane components u and v:

$$\begin{aligned} u(x,y,z) &= u_0(x,y) - z\, w_{0,x} + f(z)\, \theta_x(x,y) \\ v(x,y,z) &= v_0(x,y) - z\, w_{0,y} + f(z)\, \theta_y(x,y) \\ w(x,y) &= w_0(x,y) \end{aligned} \tag{II.9}$$

The last term in each in-plane component reflects the displacements due to transverse-shear strains. $f(z)$ is the shape function, whose choice should be made so that the resulting transverse shear stresses vanish at the top and bottom surfaces with a quadratic variation in-between. HSDTs therefore do not require a shear correction factor like the FSDT.

Third-order shear deformation theories (TSDTs) are the most common type of HSDTs in the literature. Historically, a third-order polynomial variation of transverse shear was proposed first by a number of east-European researchers (see the review of Ghugal and Shimpi [122] and the thesis of Hanna [123] for detailed historical development of HSDTs). These works have aided Reissner [124] to develop his TSDT, defined by the shape function:

$$f(z)=\frac{5}{4}z\left(1-\frac{4}{3}\frac{z^2}{h^2}\right) \tag{II.10}$$

Livenson [125] and Murthy [126] proposed a similar TSDT of the form:

$$f(z)=z\left(1-\frac{4}{3}\frac{z^2}{h^2}\right) \tag{II.11}$$

Reddy [127] adopted the shape function of equation (II.11) and followed a variationally consistent formulation unlike Levinson and Murthy. The accuracy of his theory was validated by Reddy and Phan [128] in the analysis of the vibration and buckling of plates.

Shi [129] proposed a new TSDT of the form:

$$\begin{aligned} u(x,y,z) &= u_0(x,y)+\frac{5}{4}\left(z-\frac{4}{3h^2}z^3\right)\phi_x(x,y)+\left(\frac{1}{4}z-\frac{5}{3h^2}z^3\right)\frac{\partial w_0}{\partial x}\\ v(x,y,z) &= v_0(x,y)+\frac{5}{4}\left(z-\frac{4}{3h^2}z^3\right)\phi_y(x,y)+\left(\frac{1}{4}z-\frac{5}{3h^2}z^3\right)\frac{\partial w_0}{\partial y}\\ w(x,y) &= w_0(x,y) \end{aligned} \tag{II.12}$$

Shimpi [130] developed a refined TSDT with the shape function of Reissner [124], in which the deflection was divided into bending and shearing contributions ($w=w_b+w_s$), such that:

$$\begin{aligned} u(x,y,z) &= u_0(x,y)-z\frac{\partial w_b}{\partial x}+h\left(\frac{z}{4h}-\frac{5}{3}\left(\frac{z}{h}\right)^3\right)\frac{\partial w_s}{\partial x}\\ v(x,y,z) &= v_0(x,y)-z\frac{\partial w_b}{\partial y}+h\left(\frac{z}{4h}-\frac{5}{3}\left(\frac{z}{h}\right)^3\right)\frac{\partial w_s}{\partial y}\\ w(x,y) &= w_b(x,y)+w_s(x,y) \end{aligned} \tag{II.13}$$

This theory was extended by Shimpi and Patel to the free vibration of isotropic and orthotropic plates [131], [132], and by Demirhan and Taskin [77] to the bending and free vibration problems of Levy-type porous FGM plates. Thai and Choi considered thickness stretching effect in a five-variables analysis of FGM plates [133] using Reissner's TSDT. It was found that the reduced number of variables affected marginally the accuracy, and the results were comparable to those of nine variables solutions [133].

Non polynomial HSDTs were developed in an earlier time when Levy [134] assumed the in-plane displacements as trigonometric series. Kil'chevskiy [135] used similar concept for shells analysis. Stein and Jegley [136]–[138] used a higher-order sinusoidal shear deformation theory (SSDT), which was later adopted by Touratier [139]. This SSDT has the shape function of the form:

$$f(z)=\frac{h}{\pi}\sin\frac{\pi z}{h} \tag{II.14}$$

Touratier's theory was adopted by Zenkour for the bending analysis of cross-ply laminated plates and FGM plates [140], [141] and for the buckling analysis of visco-elastic composite plates [142]. Li and Pan [143] also used this theory for the bending and free vibration of FGM piezoelectric microplates based on modified couple-stress theory. The SSDT was used by Thai and Vo for the bending, buckling and vibration of nano-scale beams [144] and nano-scale plates [145].

Tounsi et al. [146] developed a simple SSDT involving reduced four unknowns for the bending of FGM and sandwich-FGM plates under thermal loads. This refined formulation was in parallel adopted by Merdaci et al. [147] and Ameur et al. [148], always in the static analysis of FGM plates. Thai and Vo [149] extended this four-variables SSDT formulation to the buckling and vibration of FGM plates.

By introducing an additional variable, the SSDT can capture the effects of thickness normal deformation (a quasi-3D theory). Neves et al. [150] used a quasi-3D SSDT for the bending and vibration analysis of FGM plates, in which nine unknowns were used to describe the motion. A six-variables quasi-3D SSDT was used by Zenkour [73] to study the bending of thick FGM plates, and by Zenkour and Aljadani [151] to analyse the electro-mechanical buckling for FGM piezoelectric plates.

Thai and Kim [152] used a quasi-3D SSDT for the analysis of FGM plates in which the number of unknowns was further reduced to five. This quasi-3D formulation was used by Houari et al. [153] and by Fekrar et al. [74] for the thermo-mechanical analysis of FGM plates, and recently by Żur et al. [154] to analyze the vibration and buckling of sandwich FGM nanoplates integrated with piezo-magnetic face-layers.

Zenkour [155], [156] introduced certain unknowns relationships to further reduce the number of variables in the quasi-3D SSDT to four. However, we assume that the description of plate's quasi three dimensional motion by only four variables will be far less accurate than a full formulation, given that stretching effect is considered with the other effects. Also, this refined formulation [155], [156] was not verified side by side with the 3D elasticity

solution, but only with some quasi-3D solutions, which does not fully validate its accuracy.

Other types of trigonometric HSDTs were proposed as well, including tangent shape functions [157], inverse tangent function [158], and tangential trigonometric function [159].

Ait Atmane et al. [160] developed a new hyperbolic HSDT (hHSDT) for the free vibration of FGM plates supported by elastic foundation. This theory was extended by Benyoucef et al. [161] to the bending of FGM plates. Meiche et al. [162] and Nguyen Van Do et al. [61] used similar hHSDT in a refined four-variables analysis of metal-ceramic FGM plates and GPls-reinforced FGM plates, respectively. Zenkour and Aljadani [79] extended this hHSDT to the quasi-3D analysis of FGM plates buckling. Thai et al. [163] presented a new quasi-3D HSDT that was adapted from the two-dimensional hHSDT of Soldatos [164].

Mahi et al. [165] developed an efficient hHSDT for the vibration and bending analysis of isotropic, laminated and FGM plates, which has a shape function of the form:

$$f(z)=\frac{h}{2}\tanh\left(\frac{2z}{h}\right)-\frac{4}{3\cosh^2(1)}\frac{z^3}{h^2} \tag{II.15}$$

Using this shape function, Ebrahimi et al. [166] analysed the vibration of FGM beams under thermal loads in a refined formulation, and Zenkour and Aljadani [4] investigated the thermo-electrical buckling of piezoelectric FGM nanoplates using Eringen's nonlocal theory. Recently, we have used this hHSDT to analyse the mechanics of porous GPls-reinforced FGM plates in our thesis article [6]. The solution was compared to many 3D and quasi-3D solutions from recent literature, and we showed very accurate results in the vibration, bending, and buckling cases. Singh and Kumar used this theory in a refined formulation with consideration of thickness stretching.

Karama proposed an exponential shear-deformation theory (ESDT) for the analysis of laminated composite beams [167] and plates [168], which is defined by the shape function:

$$f(z)=z\,e^{-2\left(\frac{z}{h}\right)^2} \tag{II.16}$$

Zenkour and Radwan [169] used Karama's ESDT in a four-variables static analysis of FGM plates under temperature and moisture effects. The ESDT was also used with consideration of nonlocal strain gradient theory to investigate the

buckling and postbuckling of micro-sized FGM plates [170] and micro-sized FGM shells [171].

Aydogdu [172] developed a parametric ESDT shape function that represents a generalization of Karama's theory:

$$f(z) = z\,\alpha^{\frac{-2(z/h)^2}{\ln \alpha}}, \qquad \alpha > 0 \tag{II.17}$$

Some authors have worked on generalized formulations that can consider any HSDT by means of a parametric shape function (as in the form of equation (II.9)), which allows to compare theories results. For instance, Thai et al. [173] investigated a number of HSDTs using a five-variables isogeometric analysis. We have recently developed a generalized quasi-3D formulation of FGM plates bending to compare the performance of six HSDTs with the 3D solution [9].

In general, the use of an HSDT in FGM plates analysis is strongly recommended over the FSDT if one of the following cases are involved [174]:

- The thickness ratio a/h is below 10.
- Requiring an accurate estimation of frequency modes higher than the first.
- The power-law exponent of the FGM has a large value.
- The FGM plate is supported by clamped edges.

Table 1 lists the most important plates HSDTs, in which only the most common theories in the literature were selected (the number of HSDTs is actually too large). In the second column we listed the theory variant followed by the initial author. We have also searched and collected all the works that we could find of other authors who adopted that theory in FGMs analysis. The CPT was excluded because it is not a shear-deformation theory (it neglects this effect), and also it is far outperformed by more recent HSDTs. We note finally that all HSDTs, in contrast to the FSDT, do not need a shear correction factor.

Table 1: Noticeable shear-deformation plate theories in FGM literature.

Theory	Shape function $f(z)$	Author/ adoptions	Theory variables	Variation of transverse shear	Normal stretching effect
FSDT	z	Mindlin [94], also [175], [176].	$u_0, v_0, w_0, \psi_x, \psi_y$	Constant	Omitted
		Shimpi [98], also [99].	u_0, v_0, w_b, w_s	Constant	Omitted
		Shimpi [98], also [100].	u_0, v_0, ϕ, w_0	Constant	Omitted
		Tati [120], also [76].	$u_0, v_0, w_0, \varphi_x, \varphi_y$	Parabolic	Omitted
TSDT	$\frac{5}{4}z\left(1-\frac{4}{3}\frac{z^2}{h^2}\right)$	Reissner [124].	$u_0, v_0, w_0, \varphi_x, \varphi_y$	Parabolic	Omitted
		Shimpi [130], also [77], [147], [177].	u_0, v_0, w_b, w_s	Parabolic	Omitted
		Thai and Choi [133], also [178].	u_0, v_0, w_b, w_s, w_z	Parabolic	Considered
	$z\left(1-\frac{4}{3}\frac{z^2}{h^2}\right)$	Reddy [127], also [179].	$u_0, v_0, w_0, \varphi_x, \varphi_y$	Parabolic	Omitted
		Han et al. [36].	u_0, v_0, w_b, w_s	Parabolic	Omitted
SSDT	$\frac{h}{\pi}\sin\frac{\pi z}{h}$	Touratier [139], also [141].	$u_0, v_0, w_0, \varphi_x, \varphi_y$	Parabolic	Omitted
		Zenkour [73], also [63], [151], [180].	$u_0, v_0, w_0, \varphi_x, \varphi_y, \varphi_z$	Parabolic	Considered
		Tounsi et al. [146], also [77], [147], [148].	u_0, v_0, w_b, w_s	Parabolic	Omitted
		Thai and Kim [152], also [74],	$u_0, v_0, w_b, w_s, \varphi_z$	Parabolic	Considered

		[153], [154].			
		Zenkour [155], [156].	u_0, v_0, w_0, φ	Parabolic	Considered
hHSDT	$Cz - \frac{h}{\pi}\sinh\frac{\pi z}{h}$ / $C-1$, $C=\cosh(\frac{\pi}{2})$	Ait Atmane al. [160], also [61], [79], [161], [162].	$u_0, v_0, w_0, \varphi_x, \varphi_y$: [160], [161] u_0, v_0, w_b, w_s: [61], [162]	Parabolic	Omitted
	$\frac{h}{2}\tanh\left(\frac{2z}{h}\right) - \frac{4}{3\cosh^2(1)}\frac{z^3}{h^2}$	Mahi et al. [165], also [4], [6].	$u_0, v_0, w_0, \varphi_x, \varphi_y$	Parabolic	Omitted
ESDT	$z\ e^{-2(z/h)^2}$	Karama [167], [168], also [169]–[172].	$u_0, v_0, w_0, \varphi_x, \varphi_y$	Parabolic	Omitted
Generalized formulation	Parametric	Thai et al. [173].	$u_0, v_0, w_0, \varphi_x, \varphi_y$	Parabolic	Omitted
	Parametric	Hassaine and Mahi [9].	$u_0, v_0, w_0, \varphi_x, \varphi_y, \varphi_z$	Parabolic	Considered

II.3.2 Unified formulations

In addition to the HSDTs discussed above, which have explicit expressions of the shape function, is also possible to expand the displacement field in a finite polynomial Taylor series, a non-polynomial series, or a mixture of both. The displacement field with polynomial expansion is expressed as:

$$\begin{aligned} u(x,y,z) &= u_0(x,y) + z\,u_1(x,y) + z^2u_2(x,y) + z^3u_3(x,y) + \ldots + z^N u_N(x,y) \\ v(x,y,z) &= v_0(x,y) + z\,v_1(x,y) + z^2v_2(x,y) + z^3v_3(x,y) + \ldots + z^N v_N(x,y) \\ w(x,y,z) &= w_0(x,y) + z\,w_1(x,y) + z^2w_2(x,y) + z^3w_3(x,y) + \ldots + z^N w_N(x,y) \end{aligned} \tag{II.18}$$

in a non-polynomial expansion, the displacement field may be expressed in a trigonometric, hyperbolic or exponential series. If we consider the sine trigonometric expansion, for example, the displacement field is given in the form:

$$\begin{aligned} u(x,y,z) &= u_0(x,y) + z\,u_1(x,y) + \sin\left(\tfrac{\pi z}{h}\right)u_2(x,y) + \ldots + \sin\left(\tfrac{n\pi z}{h}\right)u_{N+1}(x,y) \\ v(x,y,z) &= v_0(x,y) + z\,v_1(x,y) + \sin\left(\tfrac{\pi z}{h}\right)v_2(x,y) + \ldots + \sin\left(\tfrac{n\pi z}{h}\right)v_{N+1}(x,y) \\ w(x,y,z) &= w_0(x,y) + z\,w_1(x,y) + \sin\left(\tfrac{2\pi z}{h}\right)w_3(x,y) + \ldots + \sin\left(\tfrac{n\pi z}{h}\right)w_{N+1}(x,y) \end{aligned} \tag{II.19}$$

And in general, all expansion types enter in the following unified form of displacement field:

$$\begin{aligned} u(x,y,z) &= F_0(z)u_0(x,y)+F_1(z)u_1(x,y)+...+F_N(z)u_N(x,y) \\ v(x,y,z) &= F_0(z)v_0(x,y)+F_1(z)v_1(x,y)+...+F_N(z)v_N(x,y) \\ w(x,y,z) &= F_0(z)w_0(x,y)+F_1(z)w_1(x,y)+...+F_N(z)w_N(x,y) \end{aligned} \tag{II.20}$$

Where $F_i(z)$ are known functions chosen a priori, and the limit number N is determined by considering the desired approximation.

To include membrane extension in the analysis, which is recommended in general, we set $F_0(z) = 1$. Also, the presence of a linear term (that is: $zu_1(x,y)$) was found to be very important for an accurate description of displacement and stress fields, and it will reduce the trigonometric and exponential terms needed to reach the intended degree of accuracy [181]. We note that this type of unified plate theory formulation does not have an explicit form of shape function.

Using a polynomial expansion equivalent to equation (II.18) for FGM beams vibration, Giunta et al. [182] obtained good accuracy for a computational time of an order of seconds, while using Ansys 3D FEM took hours for a refined mesh, and minutes for the coarsest mesh [182].

The polynomial series expansion has its origin in the analysis of laminated structures (beams, plates and shells), before it was extended to FGMs. This idea was first adopted by Carrera [183], [184] in what is known as the Carrera unified formulation, or CUF. Soon, CUF method was applied by Carrera et al. [185] to the mechanical analysis of FGM structures with either analytical or FEM solution methods. The most noticeable FGM works using CUF include the studies of Giunta et al. [186] and He et al. [187] for FGM beams; and Leetsch et al. [188], Fazzolari and Carrera [189], Ramos et al. [190], Frrokh et al. [191], and Dozio [174] for FGM plates; and Cinefra et al. [192] and Monge and Mantari [193], [194] for FGM shells. Using the element-free Galerkin method with CUF kinematics, Ghadiri Rad and Hosseini [195] solved the buckling problem of GPls-CNTs reinforced laminated FGM plates with circular cutouts. Neves' doctoral thesis [196] involves detailed information on the modelling and application of this method on FGM plates.

II.4 Solution methods

Deriving the full exact solution of FGM plates problems is quite difficult giving the multitude of parameters and coupled effects. Therefore, researchers recourse to analytical methods to obtain approximate but sufficiently accurate results.

These solutions are written in the form of a finite number of terms (closed-form expressions).

Researchers often prefer to consider the analytical method of Navier that applies for four simply-supported edges (SSSS supports), because of its simplicity of implementation. Another popular analytical method is the Levy method, which can solve plates problems with two simply-supported opposite edges and an arbitrary choice for the rest (which makes 6 cases: SSSS, SFSF, SCSC, SFSC, SSSC, and SSSF, where F denotes free and C denotes clamped). Navier's and Levy's methods share similar concept of expanding displacements and loads in the form of trigonometric series.

For a plate problem with a free choice of edge supports, energy methods are used to provide approximate solutions. A solution of this type is written in the form of a finite linear combination of undetermined parameters and properly-chosen functions. According to Scriven and Nayfeh and Pai [197], [198], energy methods fall into two main categories

- **Variational methods:** these include the Ritz and the Rayleigh-Ritz methods, which differ in some minor aspects, but are basically a single theory.
- **Weighted-residuals:** the most notable methods of this category are the Galerkin method, Petrov-Galerkin method, Collocation method, and Kantorovich method.

If the structural analysis involves complicated parameters such as plates with cutouts of arbitrary shapes, unconventional boundary conditions, or non-standard forms of loads, then analytical and energy methods are uncapable of providing the solution, and numerical methods are used instead. Numerical methods include the FEM, finite differences method, and element-free methods. Figure II.4 illustrates some examples of complex FGM settings from the works of Wang et al. [199] and Gupta and Talha [78], in which the FEM was used to provide the solution.

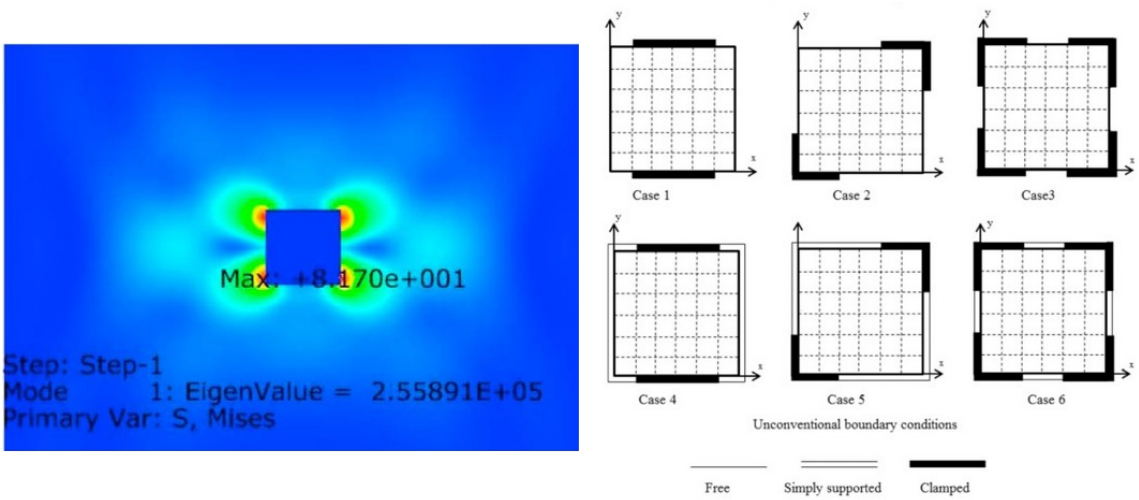

Figure II.4: Analysis of complicated FGM configurations using FEM. Left, state of von Mises stress in a cutout FGM shell wall. Adapted from Wang et al. [199]. Right: unconventional FGM plate supports. Adapted from Gupta and Talha [78].

A very important aspect in the solution procedure is the supports type of the plate. Supports are translated mathematically by a set of boundary conditions that consist of [200]:

- Kinematic –or essential– boundary conditions, which impose displacement and rotation constraints on the boundary domaine, and,
- Natural boundary conditions, which prescribe the boundary forces and moments.

These two types are present in every boundary value problem of all fields of physics. In solid mechanics particularly, these are called *geometric boundary conditions* and *force boundary conditions*, respectively [201]. Kinematic boundary conditions are intuitive to define, but force boundary conditions are not physically obvious. Variational approaches of deriving the equations of motion are advantageous in this respect by establishing force boundary conditions as automatic products of the integration-by-parts procedure [200]. The importance of finding the boundary conditions relations appears when setting up numerical methods like the FEM.

Boundary conditions strongly affect the solution of FGM plates problems. Thai et al. [173] showed that the deflection increases when changing the boundary condition from SFSF to SSSS and CCCC because of the increase of structural stiffness [173]. Gupta and Talha [78] found that the frequencies of FGM plate are the lowest in FFFF support, and they increase with more constrained supports, to a maximum in CCCC support. Shariyat and Asemi [202] revealed that buckling

occurs in lower loading for FGM plates with less constrained edges, so that critical buckling load of CFFF plate is lower than that of SCSF plate, which is lower than that of SSSS plate. Pashmforoush [57] made a statistical analysis of variance (ANOVA) on the relative importance of the input parameters relating to the free vibration response of GPls-reinforced FGM composite plates. He found that boundary condition type is the most influencing parameter on natural frequencies, more than the volume fraction of GPls, or their distribution pattern, or thickness ratio.

II.5 Concept of neutral surface

In their typical form, metal-ceramic FGMs consist of a graded matrix that vary in an asymmetric manner from from full ceramic at one surface to full metal at the other. The bending and extension motions of FGM structures are coupled in both the elastic and dynamic responses. This coupling is generated by the non-symmetric distribution of materials, and as a result, of elastic/mass properties (transverse anisotropy).

Consequently, the neutral surface is shifted from the geometric mid-surface. In the case of FGM plates, they will exhibit non-zero mid-surface extension under pure bending (ie $u_{(z=0)} \neq 0$), and non-zero deflections under the smallest tensile/compressive loads on the edges.

Choosing the reference xy plane as the neutral surface will eliminate this coupling and give identical equations to those of isotropic plates [203], [204]. This concept is analogous to the use of the elastic centre in the analysis of inhomogeneous beams, which is treated in many relevant books (for example in [205]).

Another method to eliminate FGMs' extension-bending coupling is to assume symmetric FGMs from the beginning. This approach was used by Mahi et al. [206] for FGM beams along with some simplifications of insignificant terms in the equations of motions, which has uncoupled and simplified the problem. Then an analytical method was applied to solve the equations for various boundary conditions. Mahi and Hassaine extended this analytical solution to the free vibration of GPls-reinforced FGM beams [10], and CNTs reinforced FGM beams [11].

We have recently demonstrated that the addition of GPls with more amounts in the metal-rich regions will balance the transverse distribution of elastic properties and consequently uncouple these two effects (ie extension and bending) [6].

Figure II.5 illustrates that the extension of the mid-plane of the base FGM does not vanish, but it does for the FGM with GPl-A distribution.

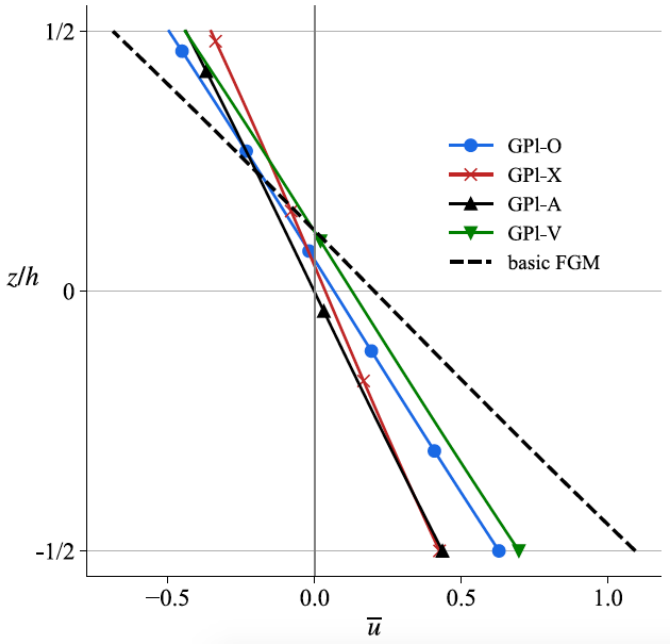

Figure II.5: Mid-plane extension of base FGM plate and FGMs with GPls inclusions, under bending. From Hassaine and Mahi [6].

Chapter III: Formulation of the FGM plate problem

III.1 Introduction

Describing the motion of elastic plates or other elastic structures requires a set of three basic equations: the equations of geometry of deformation relating displacements to strains, or kinematics; the equations of equilibrium which states the balance between body forces, stresses and inertial forces; and finally the constitutive equations relating stresses to strains [198].

Accordingly, this chapter aims to obtain the final equations of motion by going through all these modelling equations. Following the conventional modelling order of recent FGM studies that we reviewed in the previous chapter, we will start by the base FGM which is modelled by the rule of mixtures between metal and ceramic, and then we include GPls by means of the Halpin-Tsai micromechanical model, and finally we consider porosities defects using the exponential relation. All these components can be adjusted by their volume fraction and also by their through-thickness distribution. After this step, strains are obtained from the generalized displacement field (with a parametric shape function), and then stresses are obtained according to linear plane-elasticity. Finally, the equations of equilibrium are derived using Hamilton's principle.

We should note that the entire formulation was done manually from the beginning to the final governing equations of simply supported plate, including all the intermediary integrals and algebraic procedures. However, we preferred to demonstrate only the final expressions of each step, and the interested reader can refer to the thesis of Mahi [207] for the full development.

III.2 Assumptions

We base our FGM plate model on the following assumptions:

1. The FGM constitutes of an elastic and homogenous mixture of materials, with no materials discontinuities (except for micro-pores).
2. The FGM plate is isotropic in the xy plane, but not in the transverse direction.
3. The displacements of the plate are far smaller than its thickness, so it is possible to consider infinitesimal strain assumption.
4. The order of magnitude of the transverse normal stress σ_z is small and negligible compared to in-plane normal stresses σ_x and σ_y.
5. A related point is that transverse normal strain ϵ_z is negligible. This leads to the result that the transverse displacement of a point of the plate is independent from its distance from the mid-plane, or in other words, all particles with the same xy-plane position but different z's will have the same deflection.

III.3 Definition of the FGM plate

We consider a rectangular plate of length a, width b and height h, as shown in Figure III.1. The associated coordinates system is such that the z axis starts from the middle plane and points upwards, and the x and y axes start from one corner with $0 \leqslant x \leqslant a$ and $0 \leqslant y \leqslant b$.

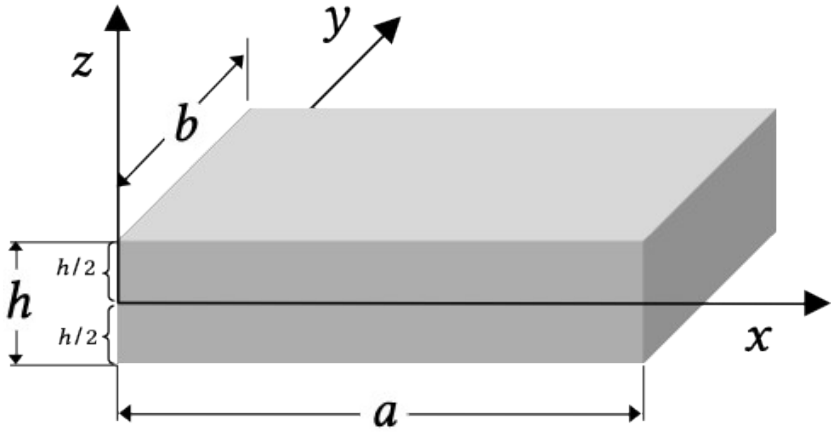

Figure III.1: Dimensions and coordinates system of the FGM plate.

The base matrix is made of a graded mixture with two components: metal (at the bottom surface) and ceramic (at the top surface), and they vary in volume ratio according to the power rule:

$$V(z)=\left(\frac{z}{h}+\frac{1}{2}\right)^{n} \tag{III.1}$$

Where V is ceramic volume fraction, noted hereafter as volume fraction shortly. V equals 1 at $z=h/2$ and 0 at $z=-h/2$. n is the power-law index (or exponent), which determines the variation profile of the FGM, and whether the FGM plate is ceramic-rich (for small values of n), or metal rich (for large values of n), Figure III.2 illustrates the volume fraction variation for different values of n.

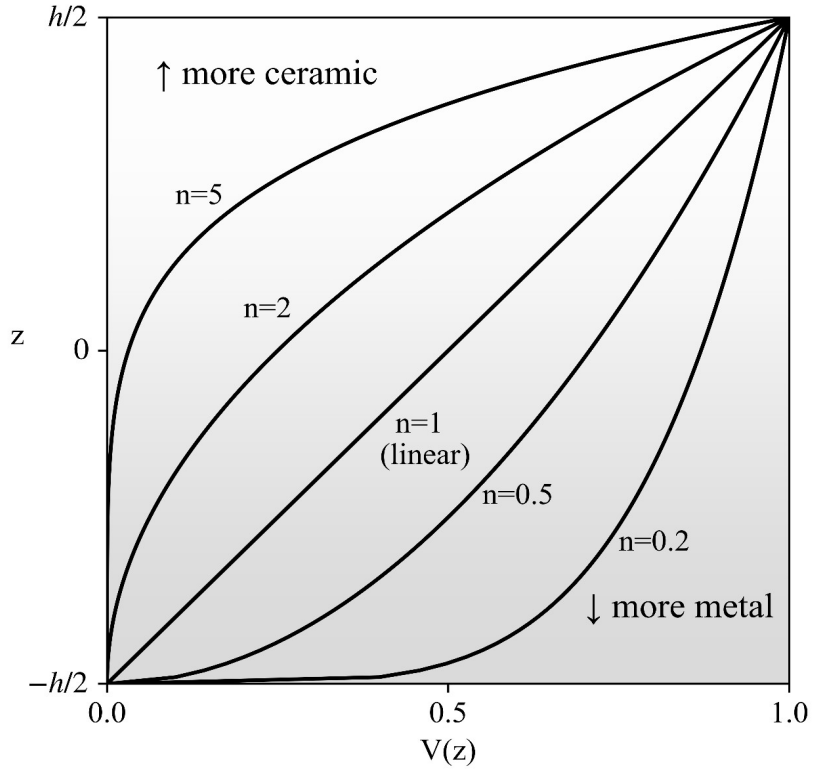

Figure III.2: Volume fraction of ceramic for different FGM power-law indices.

In addition to these illustrated examples, we have also two special cases: when $n=0$, which produces a fully ceramic plate, and when $n \to \infty$, which produces a fully metallic plate.

III.4 Effective properties of porous GPls-reinforced FGM plate

We start the procedure of FGM properties modelling from the base FGM. The effective properties of the ceramic-metal matrix are calculated by the rule of mixture:

$$P_{mat}(z) = P_c V(z) + P_m\left(1-V(z)\right) \tag{III.2}$$

Where P_{mat} denotes an equivalent material property such as the elastic modulus E_{mat}, mass density ρ_{mat} and Poisson ratio ν_{mat}.

Adding graphene nanoplatelets will enhance the mechanical properties of our FGM plate, and the new elastic modulus E_{mat}^{GPl} can be estimated using the Halpin-Tsai model [87]:

$$E_{mat}^{GPl}(z) = \frac{3}{8}\left(\frac{1+\xi_L\,\eta_L(z)V_{GPl}(z)}{1-\eta_L(z)V_{GPl}(z)}\right)E_{mat}(z) + \frac{5}{8}\left(\frac{1+\xi_T\,\eta_T(z)V_{GPl}(z)}{1-\eta_T(z)V_{GPl}(z)}\right)E_{mat}(z)$$

with:

$$\eta_L(z) = \frac{\left(E_{GPl}/E_{mat}(z)\right)-1}{\left(E_{GPl}/E_{mat}(z)\right)+\xi_L}, \qquad \eta_T(z) = \frac{\left(E_{GPl}/E_{mat}(z)\right)-1}{\left(E_{GPl}/E_{mat}(z)\right)+\xi_T} \tag{III.3}$$

$$\xi_L = 2\frac{a_{GPl}}{h_{GPl}}, \qquad \xi_T = 2\frac{b_{GPl}}{h_{GPl}}$$

Where the parameters a_{GPl}, b_{GPl} and h_{GPl} denote the average length, width and thickness of these nanoparticles, respectively. ξ_L and ξ_T are measures of reinforcements geometry, and η_L and η_T are efficiency parameters which were modified in the present analysis to be functions of z, because the matrix composition varies along the thickness.

Mass density ρ_{mat}^{GPl} and Poisson's ratio ν_{mat}^{GPl} are calculated by the rule of mixture between the matrix and GPls:

$$\begin{aligned}\rho_{mat}^{GPl}(z) &= \rho_{GPl}V_{GPl}(z) + \rho_{mat}(z)\left(1-V_{GPl}(z)\right)\\ \nu_{mat}^{GPl}(z) &= \nu_{GPl}V_{GPl}(z) + \nu_{mat}(z)\left(1-V_{GPl}(z)\right)\end{aligned} \tag{III.4}$$

Where ρ_{GPl} and ν_{GPl} are the corresponding properties of GPls, and V_{GPl} is GPls' volume fraction, which varies along the coordinate z. In the present thesis we propose the following variation patterns:

$$V_{GPl}(z)=\begin{cases}\frac{\pi}{2}\overline{V}_{GPl}\cos\left(\frac{\pi z}{h}\right) & \text{GPl-O (middle-rich GPls distibution)}\\ \frac{\pi}{2}\overline{V}_{GPl}\left|\sin\left(\frac{\pi z}{h}\right)\right| & \text{GPl-X (surface-rich GPls distibution)}\\ \frac{\pi}{2}\overline{V}_{GPl}\cos\left(\frac{\pi z}{2h}+\frac{\pi}{4}\right) & \text{GPl-A (bottom-rich GPls distibution)}\\ \frac{\pi}{2}\overline{V}_{GPl}\sin\left(\frac{\pi z}{2h}+\frac{\pi}{4}\right) & \text{GPl-V (top-rich GPls distibution)}\end{cases} \tag{III.5}$$

$\overline{V}_{GPl}$ denotes the global volume fraction of GPls with respect to the entire non-porous FGM. $\overline{V}_{GPl}$ is a volume quantity that is not practically measurable, but it can be obtained easily from the mass fraction w_{GPl} by the following relation:

$$\overline{V}_{GPl}=\frac{w_{GPl}}{w_{GPl}+\left(\rho_{GPl}/\rho_{mat}^{T}\right)\left(1-w_{GPl}\right)} \tag{III.6}$$

Where ρ_{mat}^{T} denotes the total mass density of the metal-ceramic FGM matrix, calculated by the integral:

$$\rho_{mat}^{T}=\frac{1}{h}\int_{-h/2}^{h/2}\rho_{mat}\,\mathrm{d}z \tag{III.7}$$

In addition to GPls, the plate has micro-scale pores which occur accidentally during manufacture stages. It is also possible to synthesize these porosities to improve the structure in certain aspects, such as the expected consequence of reducing weight, or relaxing stress at crack tips and increasing thermal insulation [208]. Modelling porosities is an active area of research which tries to approach the real behaviour of porous materials. Many mathematical models have been proposed with more or less accuracy in predicting the elastic properties of porous materials. In this analysis we will use the simple and accurate exponential model that was validated experimentally and theoretically, as we have discussed in section II.2.2.

For spherical and uniformly-dispersed pores, this model is expressed as:

$$E = E_0 e^{\frac{-2\phi}{1-\phi}}$$
$$\nu = \nu_0 e^{\frac{-2\phi}{1-\phi}} \tag{III.8}$$

Where E and E_0 denote respectively the elastic modulus of porous and solid (i.e non-porous) material, while ν and ν_0 denote Poisson's ratios in the same manner, and ϕ is porosity (pores volume fraction).

In our work we will assume pores density to vary along the thickness of the FGM, so that $\phi = \phi(z)$, and we set the solid material as the non-porous GPls-reinforced FGM. Then, the effective elastic properties of our porous GPls-reinforced FGM in their final form will be obtained as follows:

$$E(z) = E_{mat}^{GPl}(z)\, e^{\frac{-2\phi(z)}{1-\phi(z)}}$$
$$\nu(z) = \nu_{mat}^{GPl}(z)\, e^{\frac{-2\phi(z)}{1-\phi(z)}} \tag{III.9}$$

As for mass density, we know that this quantity should decreases linearly with porosities and not exponentially. Simply because mass is a linear superposition of individual masses, and pores are microscopic mass cuts from the solid matrix, where we cut a relative volume ϕ from the total (which corresponds to unity). Then mass density is calculated as follows:

$$\rho(z) = \rho_{mat}^{GPl}(z)(1-\phi(z)) \tag{III.10}$$

Porosity distribution function $\phi(z)$ will have similar forms as those of GPls. This is to ensure conformity and simplicity, while always considering various cases:

$$\phi(z) = \begin{cases} \frac{\pi}{2} P \cos\left(\frac{\pi z}{h}\right) & \text{P-O (middle-rich pores distibution)} \\ \frac{\pi}{2} P \left|\sin\left(\frac{\pi z}{h}\right)\right| & \text{P-X (surface-rich pores distibution)} \\ \frac{\pi}{2} P \cos\left(\frac{\pi z}{2h} + \frac{\pi}{4}\right) & \text{P-A (bottom-rich pores distibution)} \\ \frac{\pi}{2} P \sin\left(\frac{\pi z}{2h} + \frac{\pi}{4}\right) & \text{P-V (top-rich pores distibution)} \end{cases} \tag{III.11}$$

Where P is the mean volume-fraction of porosity for the entire reinforced FGM, and it is the same for all distributions.

Porosities patterns with their corresponding mathematical functions are illustrated in Figure III.3 together with the GPls distribution modes that we also described. The third case of porosities (P-A, bottom-rich distribution) may be very interesting to FGMs research, as some experimental works showed that pores are eliminated in the ceramic phase and increase along the metal phase [209]. However, this result may be technique-dependant only, and different procedures may reveal different results.

Any combination of porosities and GPls distributions can be chosen from 16 possible combination, which shows the variability of this analysis. This is in addition to the controllable FGM volume fraction using the index n.

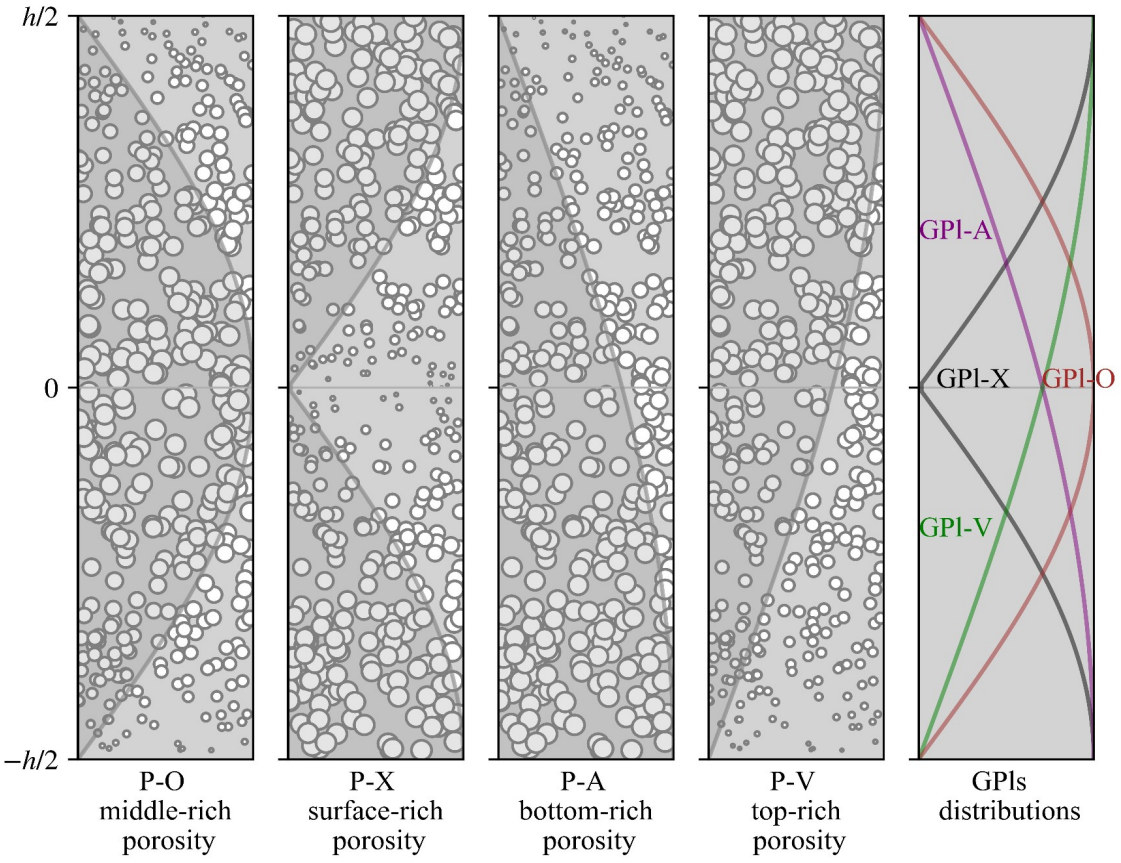

Figure III.3: Porosities distribution modes with illustrated pores density, and GPls distribution modes to the right.

III.5 Displacement field and shape function

The displacement field of the plate is expressed in a unified form as:

$$\begin{aligned} u(x,y,z,t) &= u_0(x,y,t) - z\,w_{0,x} + f(z)\left(\psi_x(x,y,t) + w_{0,x}\right) \\ v(x,y,z,t) &= v_0(x,y,t) - z\,w_{0,y} + f(z)\left(\psi_y(x,y,t) + w_{0,y}\right) \\ w(x,y,t) &= w_0(x,y,t) \end{aligned} \tag{III.12}$$

Where (u_0, v_0) are the longitudinal displacements at the mid-plane in the (x, y) directions, and w_0 is the deflection of the plate. ψ_x and ψ_y denote the bending rotations around the y and x axes at the middle plane level. A comma expresses spatial derivation and an upper dot will indicate time derivation.

$f(z)$ is the general shape function that determines the distribution of shear strains and stresses. Writing this function as a general parameter allows us to present the final equations of motion for any plate theory, including the first-order plate theory. Theory generalization also allows to test and compare different theories against the three-dimensional elasticity solution.

$f(z)$ is developed with consideration of the following criteria:

$$\begin{aligned} &f(z) = -f(-z) && \text{Odd function} \\ &f'(z=h/2) = f'(z=-h/2) = 0 && \text{Traction-free boundary condition} \end{aligned} \tag{III.13}$$

Figure III.4 illustrates a number of shape functions with their corresponding first derivatives. It can be seen that all HSDTs satisfy these conditions and have parabolic variations of the first derivative, but the FSDT fails to meet the traction-free condition. HSDTs shows little differences in functions plots, but these differences will make significant affect on the accuracy of results.

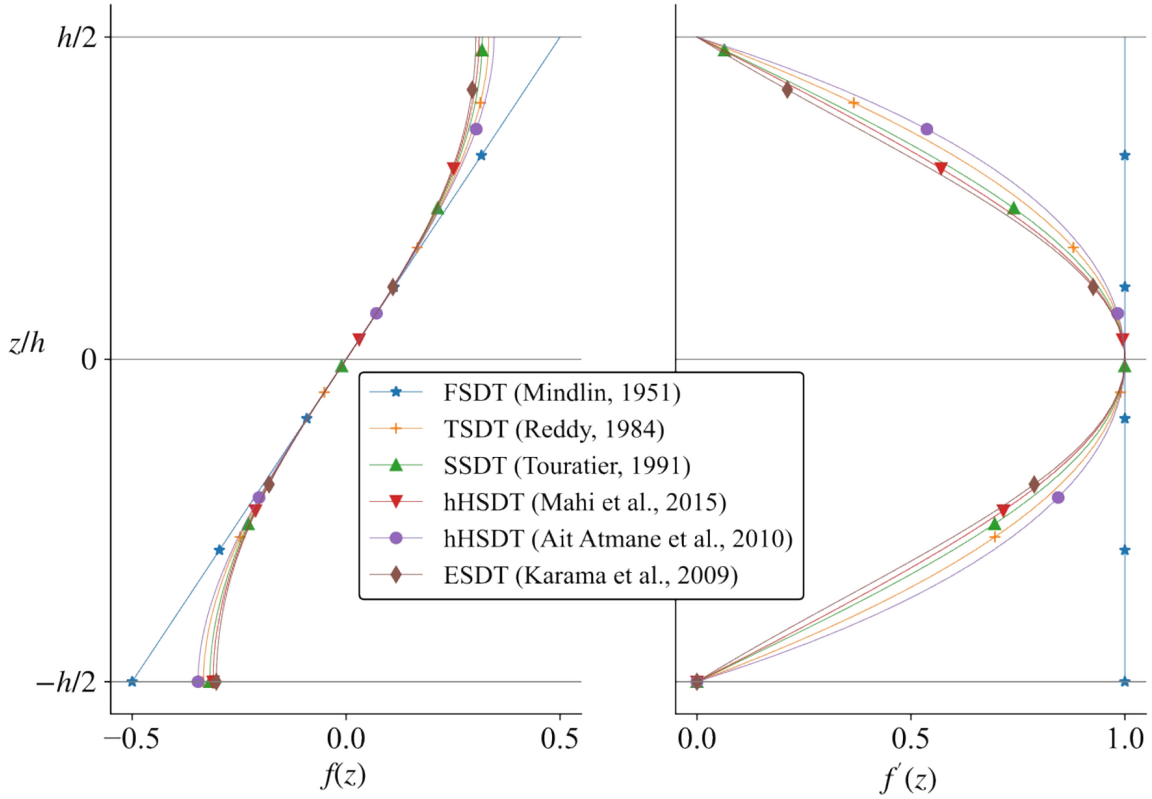

Figure III.4: Shape functions and their derivatives for various shear-deformation theories. For the shape functions expressions refer to Table 1.

In this analysis we will use the hHSDT proposed by Mahi [165]:

$$f(z) = \frac{h}{2}\tanh\left(\frac{2z}{h}\right) - \frac{4}{3\cosh^2(1)}\frac{z^3}{h^2} \tag{III.14}$$

The general strain tensor, known as Green's tensor, is given by [200]:

$$\epsilon_{ij} = \frac{1}{2}\left(\frac{\partial u_i}{\partial x_j} + \frac{\partial u_j}{\partial x_i} + \frac{\partial u_k}{\partial x_i}\frac{\partial u_k}{\partial x_j}\right) \quad i,j = \{x,y,z\} \tag{III.15}$$

As we have assumed infinitesimal deformations, the product of the derivatives of displacement components can be considered negligible next to the linear terms, which gives:

$$\epsilon_{ij} = \frac{1}{2}\left(\frac{\partial u_i}{\partial x_j} + \frac{\partial u_j}{\partial x_i}\right) \tag{III.16}$$

Or in the abridged notation:

$$\epsilon_{ij} = \frac{1}{2}\left(u_{i,j} + u_{j,i}\right) \tag{III.17}$$

By expanding this equation for strain components we obtain:

$$\begin{aligned}
\epsilon_x &= u_{,x} \\
\epsilon_y &= v_{,y} \\
\epsilon_z &= w_{,z} \\
\gamma_{yz} &= 2\,\epsilon_{yz} = v_{,z} + w_{,y} \\
\gamma_{xz} &= 2\,\epsilon_{xz} = u_{,z} + w_{,x}\ \gamma_{xy} = 2\,\epsilon_{xy} = u_{,y} + v_{,x}
\end{aligned} \tag{III.18}$$

Where γ is the engineering shear strain, which differs from the scientific strain $\epsilon_{ij(i\neq j)}$ by a factor of 2.

Substituting the displacements of equation (III.12) into the linear strain tensor gives the strain components of the FGM plate:

$$\begin{aligned}
\epsilon_x &= u_{0,x} - z\,w_{,xx} + f(z)\left(\psi_{x,x} + w_{,xx}\right) \\
\epsilon_y &= v_{0,y} - z\,w_{,yy} + f(z)\left(\psi_{y,y} + w_{,yy}\right) \\
\epsilon_z &= 0 \\
\gamma_{yz} &= f_{,z}(z)\left(\psi_y + w_{,y}\right) \\
\gamma_{xz} &= f_{,z}(z)\left(\psi_x + w_{,x}\right) \\
\gamma_{xz} &= f_{,z}(z)\left(\psi_x + w_{,x}\right) \\
\gamma_{xy} &= u_{0,y} + v_{0,x} - 2z\,w_{,xy} + f(z)\left(\psi_{x,y} + \psi_{y,x} + 2w_{,xy}\right)
\end{aligned} \tag{III.19}$$

III.6 Constitutive relations

We consider material properties by the constitutive equation which relates the internal stresses to strains through the stiffness matrix. For a linear and fully anisotropic material, this constitutive relation is given by the generalized Hooke's law [198]:

$$\begin{bmatrix} \sigma_x \\ \sigma_y \\ \sigma_{yz} \\ \sigma_{xz} \\ \sigma_{xy} \end{bmatrix} = \begin{bmatrix} C_{11} & C_{12} & C_{13} & C_{14} & C_{15} \\ C_{21} & C_{22} & C_{23} & C_{24} & C_{25} \\ C_{31} & C_{32} & C_{33} & C_{34} & C_{35} \\ C_{41} & C_{42} & C_{43} & C_{44} & C_{45} \\ C_{51} & C_{52} & C_{53} & C_{54} & C_{55} \end{bmatrix} \begin{bmatrix} \epsilon_x \\ \epsilon_y \\ \gamma_{yz} \\ \gamma_{xz} \\ \gamma_{xy} \end{bmatrix} \tag{III.20}$$

Where C_{ij} are the elastic constants containing 21 independent parameters, and σ_i are the components of stress tensor. It is noted that transverse stress σ_{zz} is omitted here because it is negligible in most plate problems, as Shames and Dym have demonstrated [200]. However, transverse shear stresses σ_{yz} and σ_{xz} are not neglected since thick and moderately-thick plates may have significant transverse shear stresses.

Equation (III.20) is the most general constitutive law for materials without any planes of symmetry. In practice however, most engineering materials have a certain degree of symmetry that will simplify this equation, and as assumed previously, our material has two orthogonal planes of symmetry. This will reduce the equation to:

$$\begin{bmatrix} \sigma_x \\ \sigma_y \\ \sigma_{yz} \\ \sigma_{xz} \\ \sigma_{xy} \end{bmatrix} = \begin{bmatrix} Q_{11} & Q_{12} & 0 & 0 & 0 \\ Q_{21} & Q_{22} & 0 & 0 & 0 \\ 0 & 0 & Q_{44} & 0 & 0 \\ 0 & 0 & 0 & Q_{55} & 0 \\ 0 & 0 & 0 & 0 & Q_{66} \end{bmatrix} \begin{bmatrix} \epsilon_x \\ \epsilon_y \\ \gamma_{yz} \\ \gamma_{xz} \\ \gamma_{xy} \end{bmatrix} \tag{III.21}$$

Where the elastic coefficients Q_{ij} are expressed as:

$$\begin{aligned} Q_{11} &= \frac{E(z)}{1-\nu^2(z)} \\ Q_{22} &= Q_{11} \\ Q_{12} &= \frac{\nu(z)E(z)}{1-\nu^2(z)} \\ Q_{21} &= Q_{12} \\ Q_{44} &= \frac{E(z)}{2(1+\nu(z))} \\ Q_{55} &= Q_{66} = Q_{44} \end{aligned} \tag{III.22}$$

Next we define the stresses and moments resultants applied on the plate per unit of length as:

$$\begin{aligned}
\left(N_x, M_x, M_x^a\right) &= \int_{-h/2}^{h/2} \left(1, z, f(z)\right)\sigma_x \, dz \\
\left(N_y, M_y, M_y^a\right) &= \int_{-h/2}^{h/2} \left(1, z, f(z)\right)\sigma_y \, dz \\
\left(Q_{xy}, M_{xy}, M_{xy}^a\right) &= \int_{-h/2}^{h/2} \left(1, z, f(z)\right)\sigma_{xy} \, dz \\
\left(Q_{yz}^a, Q_{xz}^a\right) &= \int_{-h/2}^{h/2} \left(\sigma_{yz}, \sigma_{xz}\right) f(z)_{,z} \, dz
\end{aligned} \tag{III.23}$$

Where:

N_x and N_y are the resultants of normal stresses in the x and y directions, respectively. M_x and M_y are the bending moments around the y and x axes, respectively, and M_{xy} is the torsion moment. M_x^a , M_y^a and M_{xy}^a are the corresponding moments of higher-order. Q_{xy}, Q_{yz}^a and Q_{xz}^a are the resultants of shear stresses in the xy, yz and xz planes, respectively.

Substituting the expressions of strains (equation (III.19)) and stresses (equation (III.21)) into equation (III.23), and writing the result in matrix form gives the following constitutive relation:

$$\begin{bmatrix} N_x \\ N_y \\ M_x \\ M_y \\ M_x^a \\ M_y^a \end{bmatrix} = \begin{bmatrix} A_{11} & A_{12} & B_{11} & B_{12} & B_{11}^a & B_{12}^a \\ A_{12} & A_{22} & B_{12} & B_{22} & B_{12}^a & B_{22}^a \\ B_{11} & B_{12} & D_{11} & D_{12} & D_{11}^a & D_{12}^a \\ B_{12} & B_{22} & D_{12} & D_{22} & D_{12}^a & D_{22}^a \\ B_{11}^a & B_{12}^a & D_{11}^a & D_{12}^a & D_{11}^{aa} & D_{12}^{aa} \\ B_{12}^a & B_{22}^a & D_{12}^a & D_{22}^a & D_{12}^{aa} & D_{22}^{aa} \end{bmatrix} \begin{bmatrix} u_{0,x} \\ v_{0,y} \\ -w_{0,xx} \\ -w_{0,yy} \\ \psi_{x,x} + w_{0,xx} \\ \psi_{y,y} + w_{0,yy} \end{bmatrix}$$

$$\begin{bmatrix} Q_{xy} \\ M_{xy} \\ M_{xy}^a \end{bmatrix} = \begin{bmatrix} A_{66} & B_{66} & B_{66}^a \\ B_{66} & D_{66} & D_{66}^a \\ B_{66}^a & D_{66}^a & D_{66}^{aa} \end{bmatrix} \begin{bmatrix} u_{0,y} + v_{0,x} \\ -2w_{0,xy} \\ \psi_{x,y} + \psi_{y,x} + 2w_{0,xy} \end{bmatrix} \tag{III.24}$$

$$\begin{bmatrix} Q_{xz}^a \\ Q_{yz}^a \end{bmatrix} = \begin{bmatrix} A_{55}^a & 0 \\ 0 & A_{44}^a \end{bmatrix} \begin{bmatrix} \psi_x + w_{0,x} \\ \psi_y + w_{0,y} \end{bmatrix}$$

Where the elements of stiffness matrices are defined as:

$$\begin{aligned}
\left(A_{ij}, B_{ij}, B_{ij}^{a}\right) &= \int_{-h/2}^{h/2} Q_{ij}\left(1, z, f(z)\right) \mathrm{d}z \quad (i,j=1,2,6) \\
\left(D_{ij}, D_{ij}^{a}, D_{ij}^{aa}\right) &= \int_{-h/2}^{h/2} Q_{ij}\left(z^2, z\, f(z), f^2(z)\right) \mathrm{d}z \quad (i,j=1,2,6) \\
A_{ij}^{a} &= \int_{-h/2}^{h/2} Q_{ij}\left(f_{,z}(z)\right)^2 \mathrm{d}z \quad (i,j=4,5)
\end{aligned} \tag{III.25}$$

Where:

A_{ij} coefficients represent the extension stiffness [Pa.m],

B_{ij} and B_{ij}^{a} coefficients represent the bending-extension coupling stiffness [Pa.m^2],

D_{ij}, D_{ij}^{a} and D_{ij}^{aa} coefficients represent the bending stiffness [Pa.m^3], and,

A_{ij}^{a} coefficients represent the transverse-shear stiffness [Pa.m].[6]

III.7 Hamilton's principle and the equilibrium equations

Having defined the stress resultants and stiffness coefficients, we proceed to derive the equations of equilibrium using the principle of Hamilton. This principle states that between two arbitrary time points $t\,1$ and $t\,2$, we have:

$$\int_{t\,1}^{t\,2} \left(\delta E_U + \delta W - \delta E_K\right) \mathrm{d}t = 0 \tag{III.26}$$

Where δ is the variational operator, and E_U is the strain energy, defined for the plate's volume V as:

$$E_U = \frac{1}{2} \int_V \sigma_{ij} \epsilon_{ij} \, \mathrm{d}V \tag{III.27}$$

6 If the FSDT is used, then a shear correction factor $k = 5/6$ is introduced so that: $A_{ij}^{a} = k \int_{-h/2}^{h/2} Q_{ij}\left(f_{,z}\right)^2 \mathrm{d}z$

E_K is the kinetic energy, defined as:

$$E_K = \frac{1}{2}\int_V \rho(z)\left(\dot{u}^2 + \dot{v}^2 + \dot{w}^2\right) \mathrm{d}V \tag{III.28}$$

And W is the work done by the external transverse and edge loads, which are illustrated in Figure III.5 and Figure III.6 bellow.

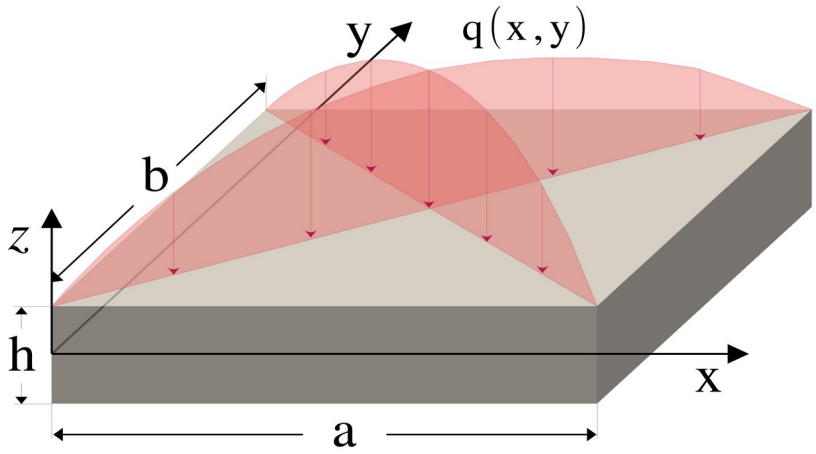

Figure III.5: Applied transverse load on the FGM plate (sinusoidal distribution).

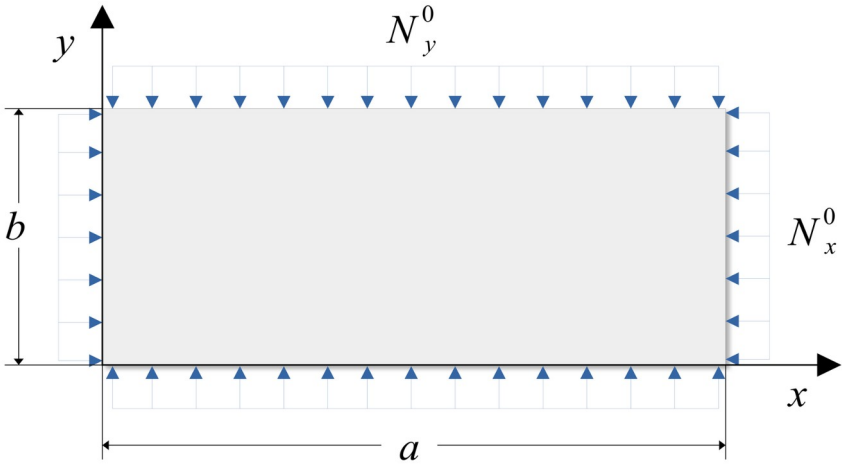

Figure III.6: Applied compressive loads on the FGM plate edges (uniform distribution).

The virtual work done by these loads is given by the formula [6]:

$$\delta W = -\int_0^b \int_0^a \left(q(x,y) + N_x^0 w_{0,xx} + N_y^0 w_{0,yy}\right)\delta w_0 \mathrm{d}x\,\mathrm{d}y \tag{III.29}$$

Where:

q is the transverse load or pressure on the top surface, and it causes plate flexure.

N_x^0 and N_y^0 are the in-plane loads applied on the edges $x=0,a$ and $y=0,b$, and they cause buckling when they are compressive and attain the critical magnitude. We set $N=N_x^0$ and relate N_y^0 to N_x^0 by a scalar μ so that $N_y^0=\mu N_x^0=\mu N$, which allows us to consider two cases:

- The bi-axial compression, for which: $\mu=1$ and $N_y^0=N_x^0=N$, and,
- The uni-axial compression, for which: $\mu=0$ and $N_y^0=0$.

By applying Hamilton's principle and performing long algebraic operations and integrations by parts, and then by setting the coefficients of δu_0, δv_0, δw_0, $\delta \psi_x$ and $\delta \psi_y$ to zero, separately, we obtained the governing equilibrium equations of the FGM plate:

$$
\begin{aligned}
&\delta u_0: \quad N_{x,x}+Q_{xy,y}=I_1\ddot{u}_0+I_2^a\ddot{\psi}_x+\left(I_2^a-I_2\right)\ddot{w}_{,x}\\
&\delta v_0: \quad N_{y,y}+Q_{xy,x}=I_1\ddot{v}_0+I_2^a\ddot{\psi}_y+\left(I_2^a-I_2\right)\ddot{w}_{,y}\\
&\delta w_0: \quad -M_{x,xx}+M_{x,xx}^a-M_{y,yy}+M_{y,yy}^a-Q_{yz,y}^a-Q_{xz,x}^a-2M_{xy,xy}\\
&\qquad +2M_{xy,xy}^a=q(x,y)+N\left(w_{0,xx}+\mu w_{0,yy}\right)+\left(I_2^a-I_2\right)\ddot{u}_{,x}\\
&\qquad +\left(I_3^{aa}-I_3^a\right)\ddot{\psi}_{x,x}+\left(I_3-2I_3^a+I_3^{aa}\right)\ddot{w}_{,xx}+\left(I_2^a-I_2\right)\ddot{v}_{,y}\\
&\qquad +\left(I_3^{aa}-I_3^a\right)\ddot{\psi}_{y,y}+\left(I_3-2I_3^a+I_3^{aa}\right)\ddot{w}_{,yy}-I_1\ddot{w}\\
&\delta\psi_x: \quad M_{x,x}^a-Q_{xz}^a+M_{xy,y}^a=I_3^{aa}\ddot{\psi}_x+I_2^a\ddot{u}_0+\left(I_3^{aa}-I_3^a\right)\ddot{w}_{0,x}\\
&\delta\psi_y: \quad M_{y,y}^a-Q_{yz}^a+M_{xy,x}^a=I_3^{aa}\ddot{\psi}_y+I_2^a\ddot{v}_0+\left(I_3^{aa}-I_3^a\right)\ddot{w}_{0,y}
\end{aligned}
\tag{III.30}
$$

Where the inertia coefficients are calculated as follows:

$$
\begin{aligned}
\left(I_1,I_2,I_3\right)&=\int_{-h/2}^{h/2}\rho(z)\left(1,z,z^2\right)\mathrm{d}z,\\
\left(I_2^a,I_3^a,I_3^{aa}\right)&=\int_{-h/2}^{h/2}\rho(z)f(z)\left(1,z,f(z)\right)\mathrm{d}z
\end{aligned}
\tag{III.31}
$$

III.8 Solution procedure

The governing equations (equations (III.30)) will be solved analytically using Navier's method, which can solve simply-supported plates along the four edges (SSSS). For this case, the boundary conditions are given as follows:

$$\begin{aligned} &\text{At edges } x=0,a: \quad v_0=w_0=\psi_y=N_x=M_x=M_x^a=0 \\ &\text{At edges } y=0,b: \quad u_0=w_0=\psi_x=N_y=M_y=M_y^a=0 \end{aligned} \tag{III.32}$$

It can be verified that writing displacements in the following trigonometric series will satisfy the boundary conditions of equation (III.32):

$$\begin{aligned} u_0(x,y,t) &= \sum_{m=1}^{\infty}\sum_{n=1}^{\infty} U_{mn}\cos(\alpha x)\sin(\beta y)\sin(\omega t) \\ v_0(x,y,t) &= \sum_{m=1}^{\infty}\sum_{n=1}^{\infty} V_{mn}\sin(\alpha x)\cos(\beta y)\sin(\omega t) \\ w_0(x,y,t) &= \sum_{m=1}^{\infty}\sum_{n=1}^{\infty} W_{mn}\sin(\alpha x)\sin(\beta y)\sin(\omega t) \\ \psi_x(x,y,t) &= \sum_{m=1}^{\infty}\sum_{n=1}^{\infty} X_{mn}\cos(\alpha x)\sin(\beta y)\sin(\omega t) \\ \psi_y(x,y,t) &= \sum_{m=1}^{\infty}\sum_{n=1}^{\infty} Y_{mn}\sin(\alpha x)\cos(\beta y)\sin(\omega t) \end{aligned} \tag{III.33}$$

Where $U_{mn}, V_{mn}, W_{mn}, X_{mn}$, and Y_{mn} are the amplitudes of displacements for each pair (m,n), $\alpha=m\pi/a$ and $\beta=n\pi/b$.

In vibration analysis, m and n represent the numbers of half-waves formed by the plate along the x and y directions, when vibrating at mode mn.

The applied transverse load is also expanded in a double trigonometric series:

$$q(x,y)=\sum_{m=1}^{\infty}\sum_{n=1}^{\infty} Q_{mn}\sin(\alpha x)\sin(\beta y) \tag{III.34}$$

In which Q_{mn} is obtained for any arbitrary form of loads by the formula:

$$Q_{mn}=\int_0^b\int_0^a q(x,y)\sin(\alpha x)\sin(\beta y)\,\mathrm{d}x\,\mathrm{d}y \tag{III.35}$$

The conventional forms of transverse load in the literature are:

a) Sinusoidally-distributed load, for which Q_{mn} is simplified to:

$$Q_{mn} = q_0 , \quad \text{with} \quad m = n = 1 \tag{III.36}$$

Where q_0 is the maximum magnitude of the sinusoidal load at the centre of the plate (see Figure III.5).

a) Uniformly-distributed load, for which Q_{mn} is simplified to:

$$Q_{mn} = \sum_{m=1}^{\infty} \sum_{n=1}^{\infty} \frac{16 q_0}{m\, n\, \pi^2} , \quad \text{with} \quad m, n = 1, 3, 5 \ldots \tag{III.37}$$

Where q_0 here is the constant magnitude of transverse load.

By substituting the series of equations (III.33) and (III.34) into equation (III.30) we obtain the following algebraic system, which translates mathematically the motion of our simply-supported FGM plate:

$$\left(\mathbf{K} + N\, \mathbf{Kg} - \omega_{mn}^2 \mathbf{M} \right) \begin{pmatrix} U_{mn} \\ V_{mn} \\ W_{mn} \\ X_{mn} \\ Y_{mn} \end{pmatrix} = \begin{pmatrix} 0 \\ 0 \\ Q_{mn} \\ 0 \\ 0 \end{pmatrix} \tag{III.38}$$

Where **K** represents the stiffness matrix, N is the critical buckling load, **Kg** is the geometric stiffness matrix, ω is the natural frequency and **M** is the inertia matrix.

To solve the dynamic problem we omit the buckling load and load vector, so we will have in expanded form:

$$\left(\begin{bmatrix} k_{11} & k_{12} & k_{13} & k_{14} & k_{15} \\ k_{21} & k_{22} & k_{23} & k_{24} & k_{25} \\ k_{31} & k_{32} & k_{33} & k_{34} & k_{35} \\ k_{41} & k_{42} & k_{43} & k_{44} & k_{45} \\ k_{51} & k_{52} & k_{53} & k_{54} & k_{55} \end{bmatrix} - \omega^2 \begin{bmatrix} m_{11} & m_{12} & m_{13} & m_{14} & m_{15} \\ m_{21} & m_{22} & m_{23} & m_{24} & m_{25} \\ m_{31} & m_{32} & m_{33} & m_{34} & m_{35} \\ m_{41} & m_{42} & m_{43} & m_{44} & m_{45} \\ m_{51} & m_{52} & m_{53} & m_{54} & m_{55} \end{bmatrix} \right) \begin{pmatrix} U_{mn} \\ V_{mn} \\ W_{mn} \\ X_{mn} \\ Y_{mn} \end{pmatrix} = \begin{pmatrix} 0 \\ 0 \\ 0 \\ 0 \\ 0 \end{pmatrix} \tag{III.39}$$

Where the coefficients of **K** and **M** are given in Appendix A.

For the static problem, we set the buckling load and natural frequency to zero:

$$\begin{bmatrix} k_{11} & k_{12} & k_{13} & k_{14} & k_{15} \\ k_{21} & k_{22} & k_{23} & k_{24} & k_{25} \\ k_{31} & k_{32} & k_{33} & k_{34} & k_{35} \\ k_{41} & k_{42} & k_{43} & k_{44} & k_{45} \\ k_{51} & k_{52} & k_{53} & k_{54} & k_{55} \end{bmatrix} \begin{pmatrix} U_{mn} \\ V_{mn} \\ W_{mn} \\ X_{mn} \\ Y_{mn} \end{pmatrix} = \begin{pmatrix} 0 \\ 0 \\ Q_{mn} \\ 0 \\ 0 \end{pmatrix} \qquad \text{(III.40)}$$

And for the buckling problem, we omit the natural frequency and the transverse load:

$$\left(\begin{bmatrix} k_{11} & k_{12} & k_{13} & k_{14} & k_{15} \\ k_{21} & k_{22} & k_{23} & k_{24} & k_{25} \\ k_{31} & k_{32} & k_{33} & k_{34} & k_{35} \\ k_{41} & k_{42} & k_{43} & k_{44} & k_{45} \\ k_{51} & k_{52} & k_{53} & k_{54} & k_{55} \end{bmatrix} + N \begin{bmatrix} 0 & 0 & 0 & 0 & 0 \\ 0 & 0 & 0 & 0 & 0 \\ 0 & 0 & kg_{33} & 0 & 0 \\ 0 & 0 & 0 & 0 & 0 \\ 0 & 0 & 0 & 0 & 0 \end{bmatrix} \right) \begin{pmatrix} U_{mn} \\ V_{mn} \\ W_{mn} \\ X_{mn} \\ Y_{mn} \end{pmatrix} = \begin{pmatrix} 0 \\ 0 \\ 0 \\ 0 \\ 0 \end{pmatrix} \qquad \text{(III.41)}$$

With $kg_{33} = \alpha^2 + \mu\beta^2$.

Chapter IV: Results and discussion

IV.1 Introduction

This fourth chapter is dedicated to the presentation and discussion of the results of the dynamic, bending and buckling investigations of porous GPls-reinforced FGM plates. Obtaining the results of such multi-parametric structures required the use of a performant programming language. Initially, the choice was between Fortran, Maple, and Python. After weighting the advantages and limits of each language, Python was easily chosen for many reasons:

- Python has a large number of libraries and packages in all domains, and particularly in scientific computing.
- It is open-source and free, unlike Maple.
- Extensive maintenance and constant upgrading to match modern computing technologies, unlike Fortran.
- User-friendly interface and rich graphing tools.
- Active community and dedicated help forums.

The general organigram of our in-house developed Python algorithms is depicted in Appendix B. Using that programming procedure, we have performed the computational solution and obtained our numerical and graphical results for each of the elastic properties, natural frequencies, stresses and displacements, critical buckling loads, and vibration and buckling modes shapes.

IV.2 Material constants and non-dimensional quantities

In the following examples, and except otherwise indicated, we define metal and ceramic of our FGM matrix as aluminium (Al) and alumina (Al_2O_3). Aluminium alloys have extensive use in automobiles, aircrafts, and space vehicles for their

suitable mechanical characteristics that come with low weight penalty. On the other hand, alumina is an excellent thermal insulator that is incorporated in thermal protection systems of space structures and in engines components. This suggests that Al–Al_2O_3 FGMs have a good potential for transportation and aerospace uses, and it also justifies their choice for the present investigation.

The properties of metal and ceramic are [38]: $E_m = 70$ GPa, $\rho_m = 2702$ kg/m^3, $E_c = 380$ GPa, $\rho_c = 3800$ kg/m^3, and $\nu_m = \nu_c = 0.3$

As for GPls, we have from the data of [52]: $a_{GPl} = 2.5$ μm, $b_{GPl} = 1.5$ μm, $h_{GPl} = 1.5$ nm, $E_{GPl} = 1010$ GPa, $\nu_{GPl} = 0.186$ and $\rho_{GPl} = 1060$ kg/m^3.

Also, we will adopt the following non-dimensional parameters to conveniently present the results of mechanical response:

$$
\begin{aligned}
\overline{\omega} &= \frac{a^2}{h}\sqrt{\frac{\rho_c}{E_c}}\cdot\omega && \text{(frequency parameter)}\\
\overline{u} &= \frac{100\,h^3 E_c}{q_0 a^4}\cdot u\left(\frac{a}{4},\frac{b}{4},z\right) && \text{(extension parameter)}\\
\overline{w} &= \frac{10\,h^3 E_c}{q_0 a^4}\cdot w\left(\frac{a}{2},\frac{b}{2}\right) && \text{(deflection parameter)}\\
\overline{\sigma}_x &= \frac{h}{q_0 a}\cdot \sigma_x\left(\frac{a}{2},\frac{b}{2},\frac{h}{3}\right) && \text{(bending stress parameter)}\\
\overline{\sigma}_{xz} &= \frac{h}{q_0 a}\cdot \sigma_{xz}\left(0,\frac{b}{2},0\right) && \text{(transverse-shear stress parameter)}\\
\overline{N} &= \frac{b^2}{h^3 E_c}\cdot N && \text{(critical buckling load parameter)}
\end{aligned}
\qquad \text{(IV.1)}
$$

IV.3 Effects of GPls on elastic properties

In this section we will investigate the impact of GPls distributions on the profile of elastic modulus. Significant improvement is expected since GPls' modulus is 14.43 times higher than that of Al, and 2.66 times higher than that of Al_2O_3. We will study different base-FGMs with $n = \{0, 0.1, 1, 10\}$, which represent FGMs with ceramic isotropic composition (CI), ceramic-rich composition (CR), equal ceramic and metal composition (CM), and metal-rich composition (MR), respectively. GPls are included in the distributions given in equation (III.5), and have average mass ratios of $w_{Gpl} = \{0.5\%, 2\%, 8\%\}$. The results of all these parameters are given graphically in Figure IV.1 (CI FGM), Figure IV.2 (CR FGM), Figure IV.4 (CM FGM), and Figure IV.3 (MR FGM).

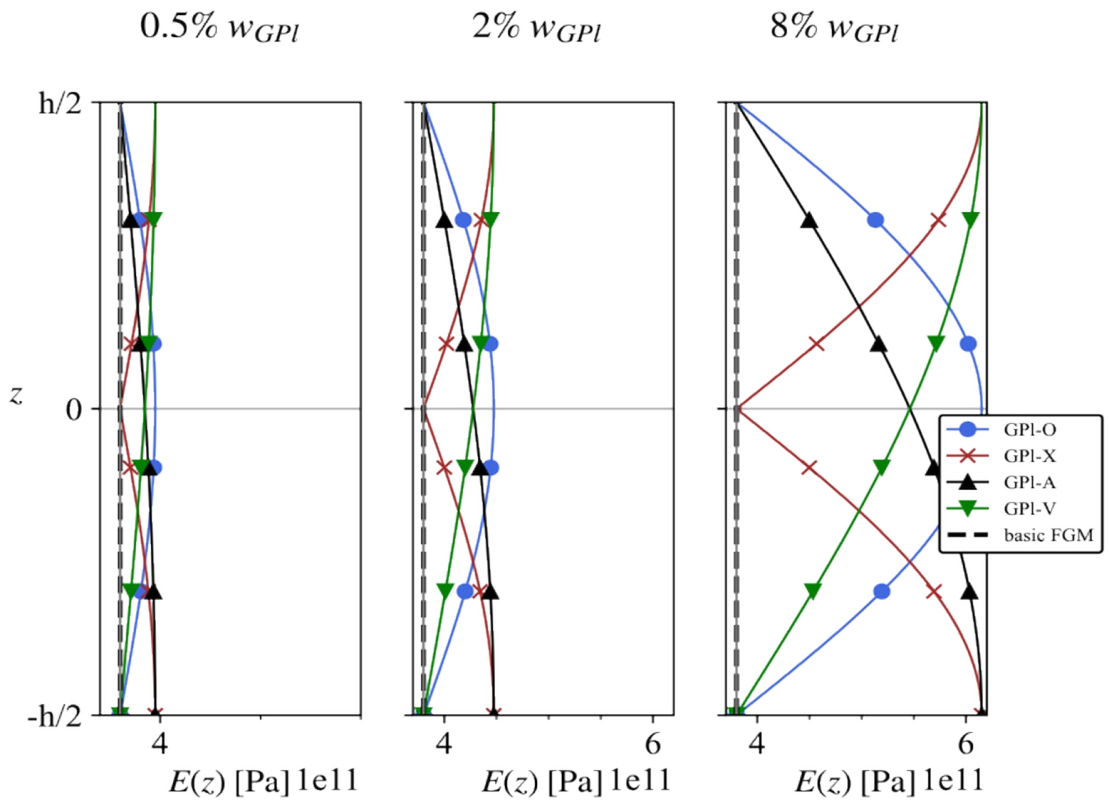

Figure IV.1: Effects of GPls on the profile and magnitude of elastic modulus of CI FGM plate.

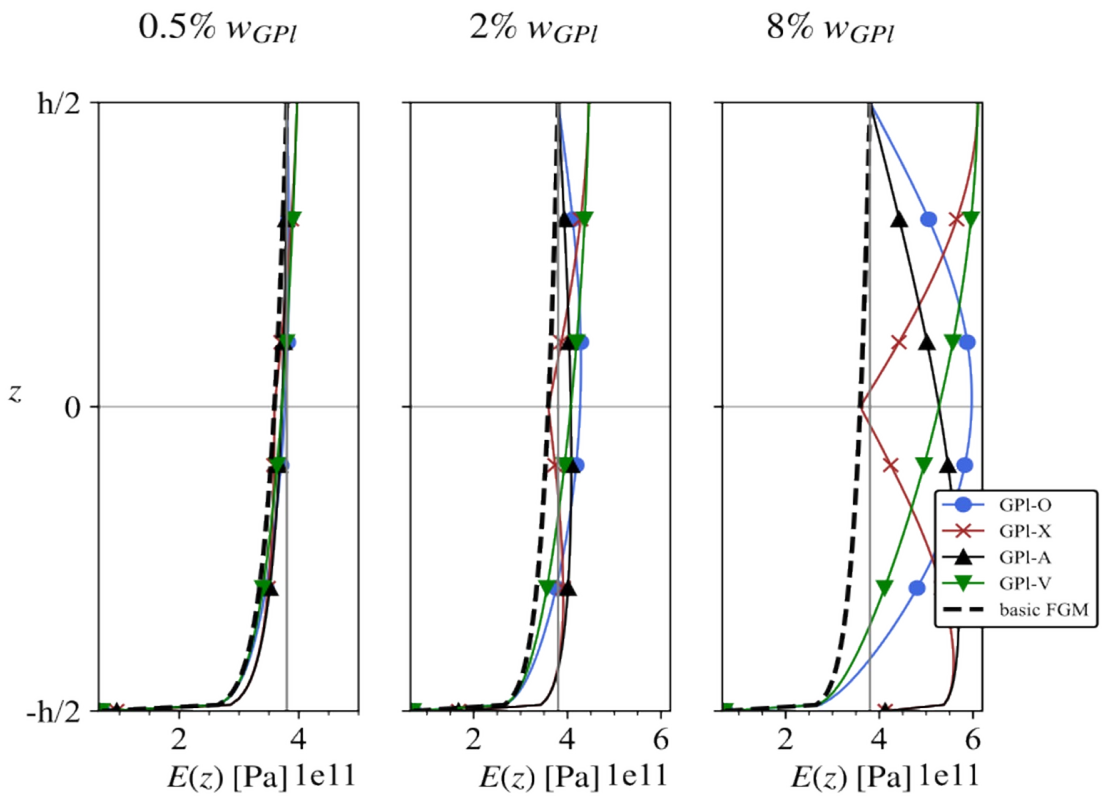

Figure IV.2: Effects of GPls on the profile and magnitude of through-thickness elastic modulus of CR FGM plate.

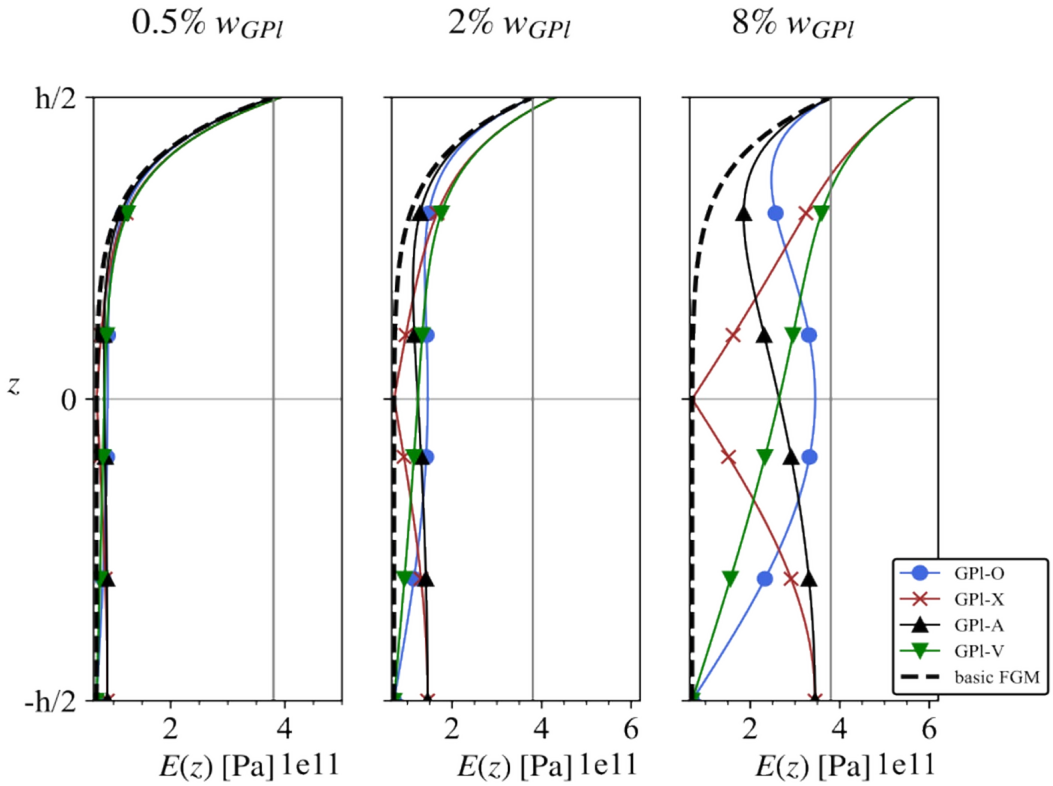

Figure IV.3: Effects of GPls on the profile and magnitude of through-thickness elastic modulus of MR FGM plate.
modulus of CM FGM plate.

Starting by the CI FGM plate in Figure IV.1, the initial elastic modulus has the constant value of $E=E_c$, and then it increases by GPls according to their dispersion pattern: GPl-O will stiffen the inner core-region, GPl-X will stiffen the outer surface-regions, GPl-A will stiffen the lower metal-rich region, and GPl-V will stiffen the upper ceramic-rich region.

For the CR FGM plate in Figure IV.2, the elastic modulus of the base FGM has a value close to E_c across most of the plate, but it rapidly reduces to E_m in the lower quarter. The CM FGM in Figure IV.4 shows a linear transition from E_m to E_c, and the MR FGM in Figure IV.3 has a modulus value adjacent to E_m except in the upper quarter where it shifts rapidly to E_c. GPls reinforcements are reflected in the increased modulus in a proportional manner to w_{GPl}, similarly to CI FGM.

We also note that the elastic modulus of GPls-reinforced CI FGM has the same sinusoidal profiles as GPls distributions. This is not the case in the CR, CM, and MR FGMs, whose variable initial moduli influence the sinusoidal profiles after GPls addition. GPls loading of 0.5 % has very small effect on the FGM, and the increase is noticeable from 2% and .

It is also interesting to observe the tendency of balancing of elastic modulus through the thickness by GPl-A in CR, CM, and MR FGMs, which results from the reinforcing of the softer metal region. Oppositely, GPl-V will further intensify the variation of $E(z)$ along the thickness, increasing the degree of transverse anisotropy.

Changing elastic modulus magnitude and profile will directly affect the stiffness coefficients given in equation (III.25). Therefore, we present in Figure IV.5 the variation of coefficients A_{11}, B_{11}, D_{11}, and A^a_{44} with GPls weight-fraction for CM FGM. We note that because of the isotropy in the xy plane we have: $A_{11}=A_{22}$. $B_{11}=B_{22}, \ldots, A^a_{44}=A^a_{55}$. Also, we have found in our article [6] that all the coefficients of each stiffness category exhibit the same variation with GPls as the representative coefficients of this example.

We can observe in the figure that the extension stiffness A_{11} increases in similar manners for different GPls distributions. Coupling stiffness B_{11} increases with GPl-V, but decreases with the other distributions. Bending stiffness D_{11} will increase for all GPls distribution with a maximum rate in GPl-X. Transverse-shear stiffness A^a_{44} shows maximum increase in GPl-O. Notice that the graph scales are not equal, and the bending stiffness is smaller by at least one order of magnitude than the other stiffness coefficients, which reflects plates structures being more compliant in flexure than the other types of deformation (ie shear and extension).

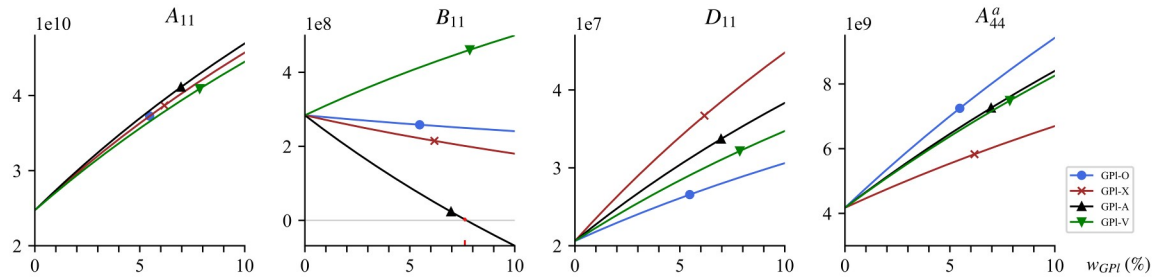

Figure IV.5: Change of stiffness coefficients with GPls weight-fraction under different distributions (n=1, h=0.1 m).

IV.4 Effects of porosity on elastic properties

Although that certain amounts of porosity are desired in many engineering fields for the reduction of total weight and minimization of materials consumption, porosities also affect negatively the structural rigidity and mechanical resistance.

To study this effect, we show in Figure IV.6, Figure IV.7, Figure IV.8, and Figure IV.9 how the elastic modulus is modified from the base FGM by porosities in different kinds of FGMs (GPls are not considered). The effects of 0.5% porosities are hardly discerned, but a small decrease of elastic modulus magnitude can be seen in P=2%. The effect of porosity on elastic modulus does not become significant until P=8%, where we can see manifest decrease. Each porosity pattern will touch and modify the region where it is concentrated: P-O will soften the inner region, P-X will soften the uppermost and lowermost regions, P-A will soften the lower region, and P-V will soften the upper region. Upon close observation, we can see that P-V tends to reduce the variance of $E(z)$ across the thickness, while P-A has a contrary effect.

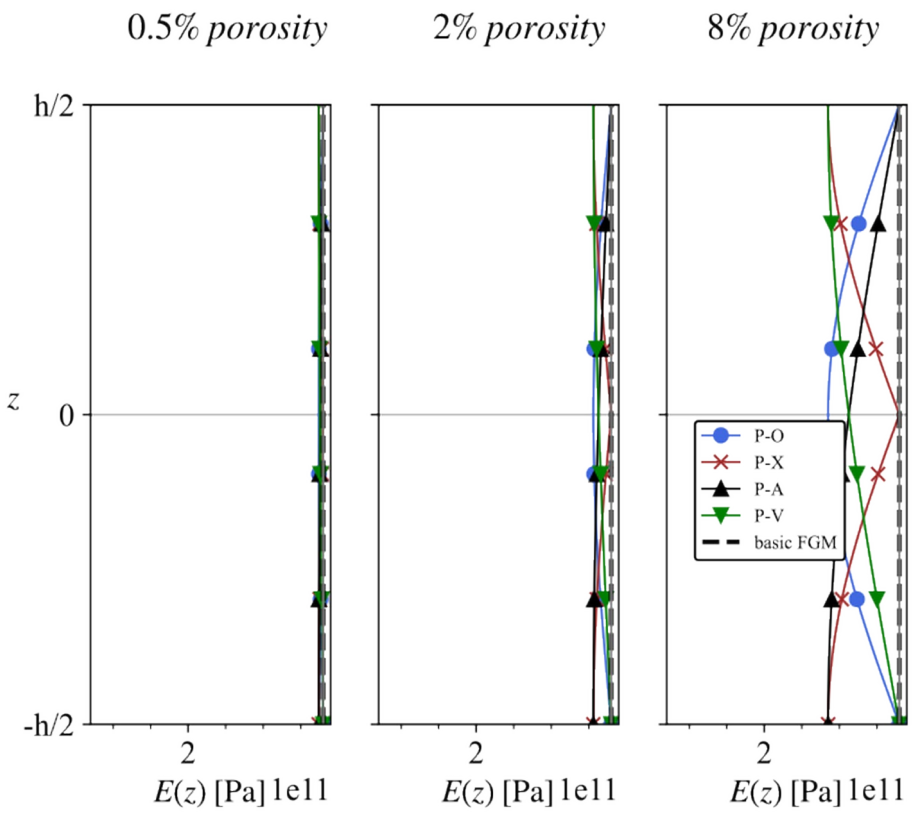

Figure IV.6: Effects of porosity volume-fraction on the profile and magnitude of through-thickness elastic modulus of CI FGM plate.

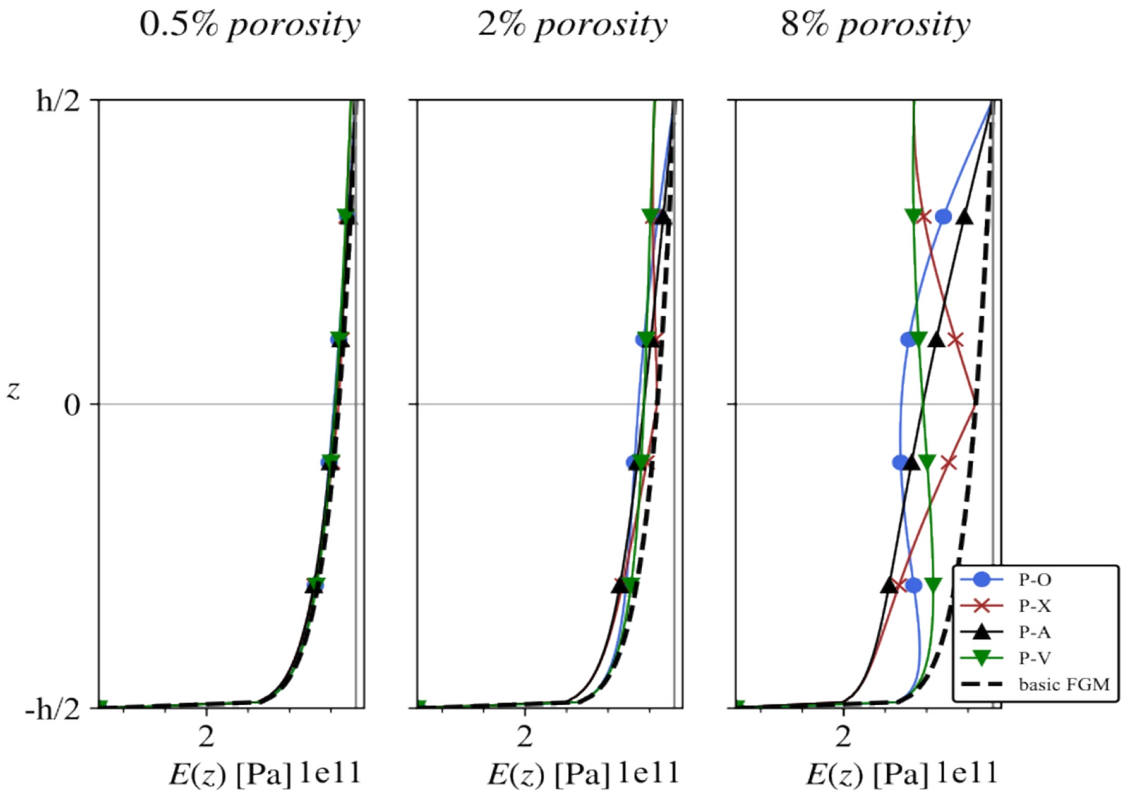

Figure IV.7: Effects of porosity volume-fraction on the profile and magnitude of through-thickness elastic modulus of CR FGM plate.

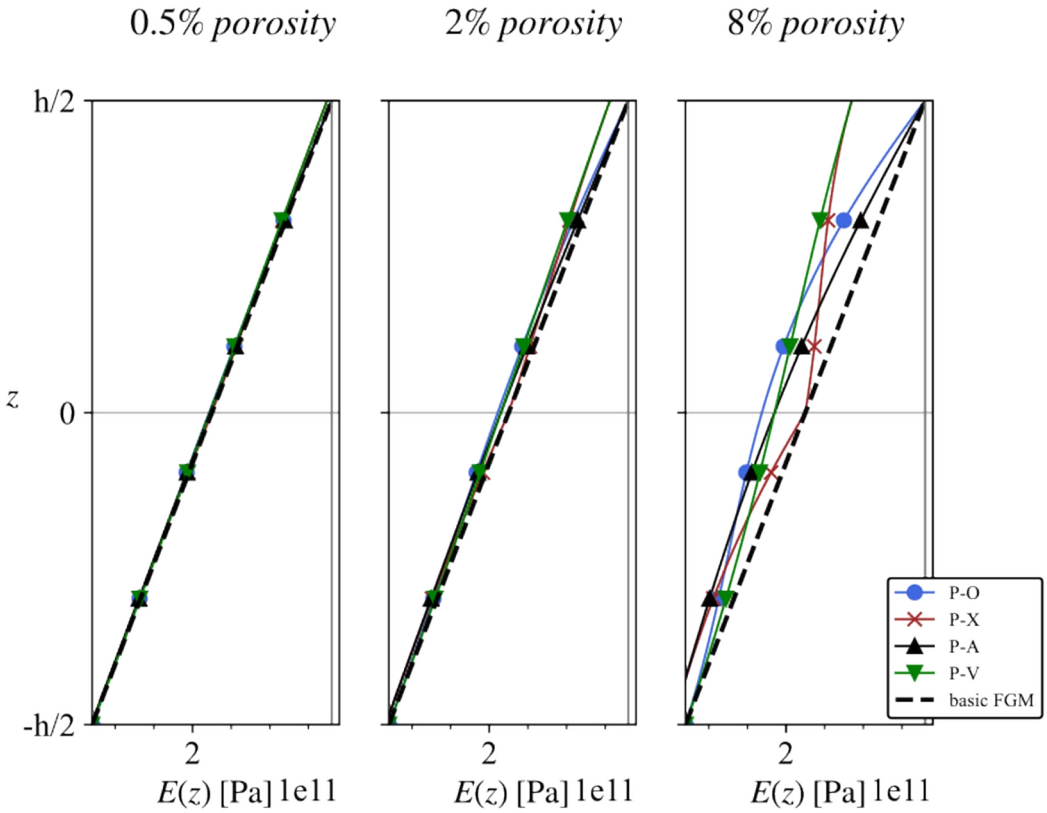

Figure IV.8: Effects of porosity volume-fraction on the profile and magnitude of through-thickness elastic modulus of CM FGM plate.

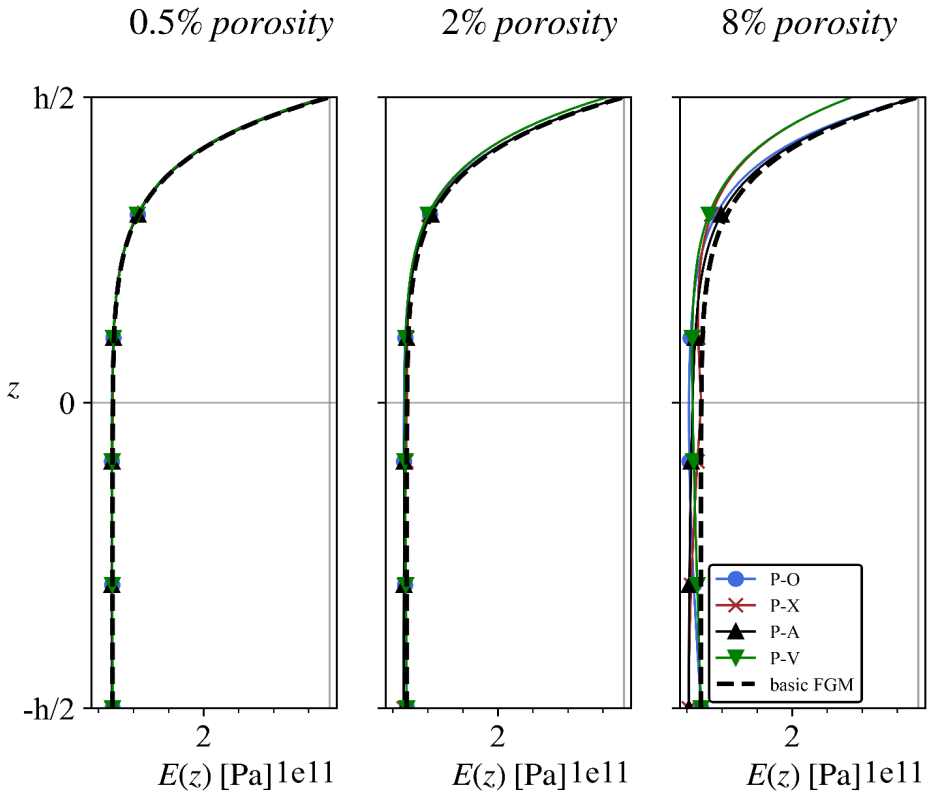

Figure IV.9: Effects of porosity volume-fraction on the profile and magnitude of through-thickness elastic modulus of MR FGM plate.

The effect of porosity on stiffness coefficients is illustrated in Figure IV.10 for a CM FGM plate with porosity volume-fraction up to 30%, which includes the range of porosity in many porous engineering materials. We can see that these material defects will induce a remarkable loss in stiffness resulting from compromised elastic modulus. However, coupling stiffness increases in P-A, which is due to the reduction of the elastic modulus in the softer metal-rich region, which increased the modulus discrepancy with the stiffer ceramic-rich region.

P-V, in an opposite action, has made the elastic modulus more uniform by softening the ceramic-rich region, which has eventually cancel B_{11} at a porosity amount of ~25 % (as marked by the red tick). This suggests that increasing porosity in proportion with the local volume-fraction of ceramic will reduce and possibly eliminate the bending-extension coupling of metal-ceramic FGMs.

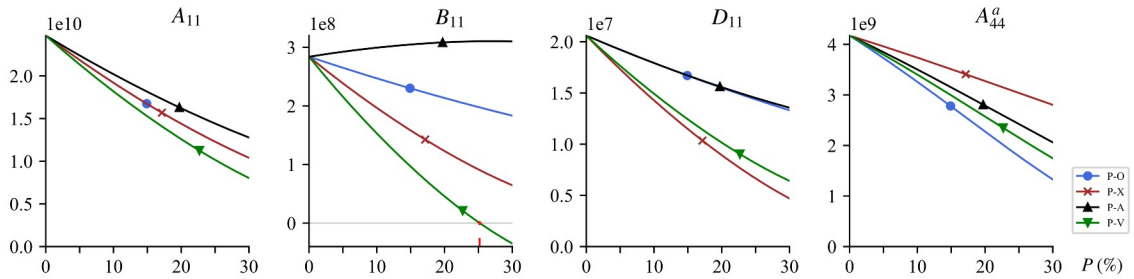

Figure IV.10: Change of stiffness coefficients with porosity volume-fraction under different distributions (n=1, h=0.1 m).

IV.5 Investigation of the mechanical behaviour

After investigating materials properties of porous GPls-reinforced FGM plates, we will now analyse their mechanical behaviour. Because of the absence of previous studies on GPls-reinforced metal-ceramic FGM plates, the only sources which can be compared with are those treating porous metal-ceramic FGM plates, or isotropic plates with GPls reinforcement. First, a number of validation examples will be undertaken to show the accuracy of our method. Then we will investigate the dynamic, static, and stability results of our porous GPls-reinforced FGM plate.

IV.5.1 Free vibration response

IV.5.1.1 Validation examples

In order to demonstrate the accuracy of our method in free vibration analysis, we will show the frequency results of the present method using three theories:

- FSDT (with a shear correction factor k),
- TSDT,
- hHSDT.

Then the calculated frequencies are normalized to the exact elasticity solution of Jin et al. [210], i.e:

$$\text{normalized frequency} = \frac{\overline{\omega}}{\overline{\omega}_{exact}} \tag{IV.2}$$

This form of presentation offers a visual indication on the accuracy of each theory by comparing the distance to 1. It is also possible to estimate the relative error from graph values by using the following expression:

$$\text{relative error } (\%) = \frac{\overline{\omega}_{exact} - \overline{\omega}}{\overline{\omega}_{exact}} \cdot 100 = (1 - \text{normalized frequency}) \cdot 100 \tag{IV.3}$$

We consider a moderately-thick square FGM plate with $a/h = 10$ (Figure IV.11) and a thick plate with $a/h = 5$ (Figure IV.12). Both graphs are presented with equal y-axis gradations to view the change of accuracy with thickness ratio.

For the moderately-thick plate in Figure IV.11, the two HSDT models show excellent accuracy, and their relative frequency errors did not exceed 0.16 %. On the other hand, the FSDT overestimates the frequencies but with tolerable error (maximum error $\approx$ 1.4 %). The divergence of the FSDT is more pronounced in thick plate (Figure IV.12), where maximum error was $\approx$ 1.49 %. The TSDT and hHSDT remain accurate for thick plate, with less than 0.5 % error. Overall, the present generalized formulation is highly effective in predicting the natural frequencies using HSDTs, even for thick plates which are difficult to calculate accurately. The FSDT is less accurate, especially for thick plates and also for larger power-low exponents. After this validation example, we will use the hHSDT except otherwise indicated.

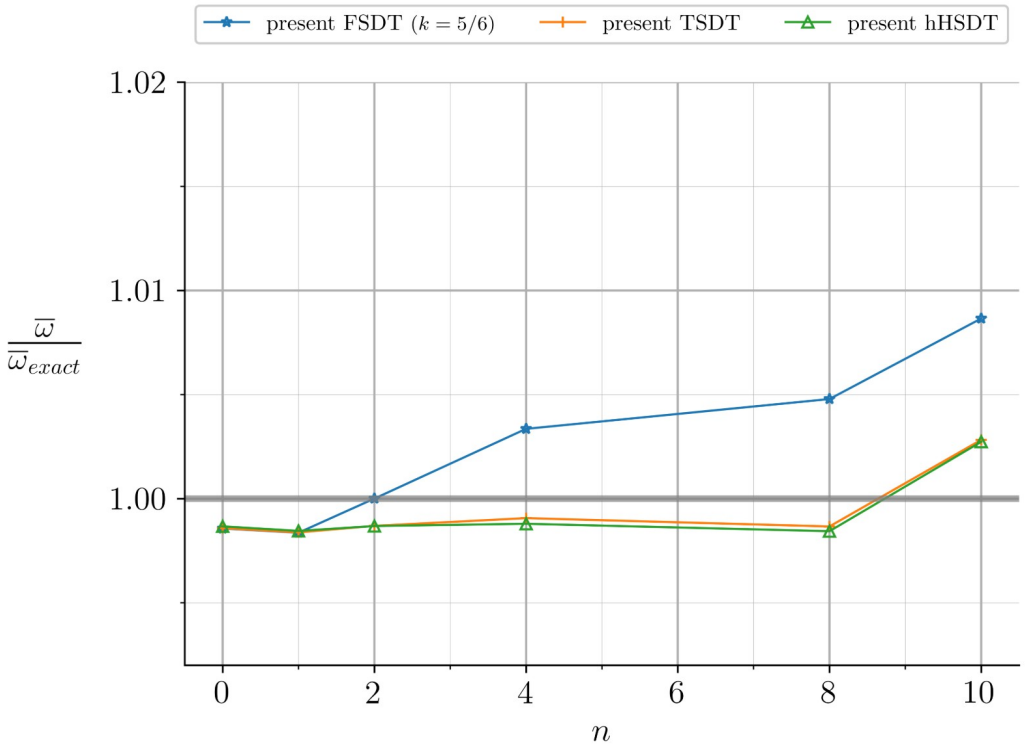

Figure IV.11: Natural frequency normalized to the exact solution of reference [210] for a moderately-thick FGM plate (a/h=10).

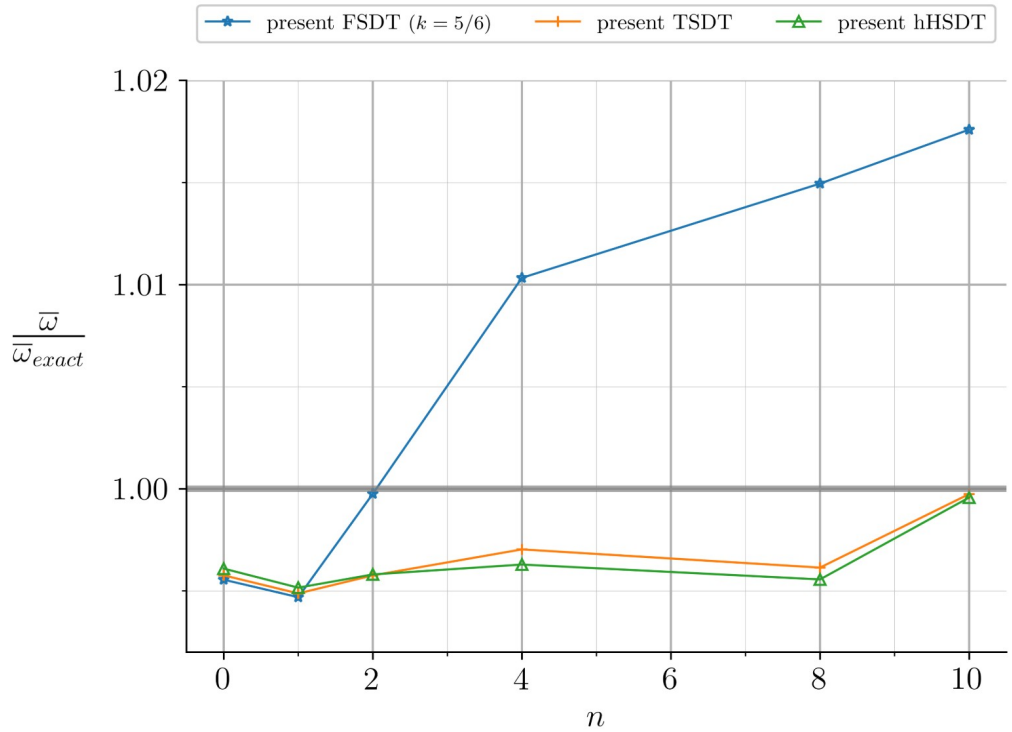

Figure IV.12: Natural frequency normalized to the exact solution of reference [210] for a thick FGM plate (a/h=5).

In the second example we will study the free vibration behaviour of porous FGM plates with different geometric and material settings. The results are compared with the 3D meshless solution of Lahdiri and Kadri [38], where the modified rule of mixtures was used to obtain the equivalent material properties. The results are obtained from our article [6], and they show that our solution for porous FGM plates is excellently accurate compared to the 3D solution.

Table 2: Validation of the results of fundamental frequency parameter $\overline{\omega}$ for porous FGM plates with different settings.

a/b	n	porosity	method	porosities distribution mode	
				even	uneven
1	0	0	present	5.9200	5.9200
			3D	5.9258	5.9258
		0.1	present	5.9507	5.9912
			3D	5.9564	5.9975
		0.2	present	6.0026	6.0694
			3D	6.0082	6.0772
	1	0	present	4.5229	4.5229
			3D	4.5279	4.5279
		0.1	present	4.3830	4.5343
			3D	4.3881	4.5397
		0.2	present	4.2069	4.5463
			3D	4.2120	4.5528
	5	0	present	3.8880	3.8880
			3D	3.8909	3.8909
		0.1	present	3.5636	3.8423
			3D	3.5659	3.8446
		0.2	present	3.0173	3.7783
			3D	3.0188	3.7796
2	0	0	present	3.7124	3.7124
			3D	3.7168	3.7168
		0.1	present	3.7312	3.7571
			3D	3.7357	3.7618
		0.2	present	3.7634	3.8063
			3D	3.7679	3.8119

	1	0	present	2.8353	2.8353
			3D	2.8392	2.8392
		0.1	present	2.7472	2.8425
			3D	2.7511	2.8467
		0.2	present	2.6363	2.8502
			3D	2.6404	2.8550
	5	0	present	2.4401	2.4401
			3D	2.4424	2.4424
		0.1	present	2.2363	2.4122
			3D	2.2384	2.4143
		0.2	present	1.8930	2.3731
			3D	1.8948	2.3748

In the third validation example we present the natural frequencies results of GPls-reinforced composite plates for the first six modes of vibration. Frequencies are given in the following non-dimensional form:

$$\hat{\omega} = \omega h \sqrt{\frac{\rho_m}{E_m}}$$

We use here the tabulated results that we obtained in our article [6] employing the same procedure as herein. Our results are given for both the FSDT and hHSDT, while those of the comparison sources ([52], [211]) use the FSDT. It can be seen that FSDT results agree well since the same plate theory is used. The hHSDT is also close but it shows higher difference, which is because the FSDT is less accurate than the hHSDT and does not satisfy the boundary conditions like other HSDTs.

Table 3: Validation of non-dimensional frequency results for GPls-reinforced laminated FGM plates with different GPls distributions.

Distribution pattern	Method	Modes					
		(1,1)	(1,2)	(2,2)	(1,3)	(2,3)	(3,3)
UD	Present hHSDT	0.1250	0.3086	0.4880	0.6053	0.7781	1.058
	Present FSDT	0.1215	0.2893	0.4433	0.5396	0.6762	0.8863
	Song et al. [52]	0.1216	0.2895	0.4436	0.5400	0.6767	0.8869
	Guo et al. [211]	0.1216	0.2895	0.4434	0.5400	0.6763	-
FG-O	Present hHSDT	0.1040	0.2569	0.4062	0.5039	0.6476	0.8805

	Present FSDT	0.1020	0.2454	0.3794	0.4642	0.5856	0.7750
	Song et al.	0.1020	0.2456	0.3796	0.4645	0.5860	0.7755
	Guo et al.	0.1020	0.2455	0.3793	0.4645	0.5855	-
FG-X	Present hHSDT	0.1428	0.3528	0.5579	0.6920	0.8894	1.2090
	Present FSDT	0.1377	0.3247	0.4935	0.5980	0.7449	0.9684
	Song et al.	0.1378	0.3249	0.4939	0.5984	0.7454	0.9690
	Guo et al.	0.1378	0.3249	0.4937	0.5985	0.7452	-
FG-V	Present hHSDT	0.1143	0.2813	0.4434	0.5489	0.7033	0.9513
	Present FSDT	0.1117	0.2671	0.4107	0.5010	0.6295	0.8282
	Song et al.	0.1118	0.2673	0.4110	0.5013	0.6299	0.8287
	Guo et al.	0.1118	0.2673	0.4108	0.5013	0.6293	-

IV.5.1.2 Parametric analysis

Having verified the solution method for the free vibration of FGM plates made of porous metal-ceramic FGM or GPls-reinforced polymer FGM, we will now extend our analysis to the dynamic response of metal-ceramic FGM plates with both porosities and GPls.

In Figure IV.13 we present the evolution of natural frequency with GPls addition for CI, CR, CM, and MR FGM plates. We can see that frequencies always increase with GPls weight-fraction, and that the most pronounced increment occurs in GPl-X, which reflects its optimal enhancement of bending stiffness. GPl-A gives the second highest increase in frequencies (for isotropic plates this distribution is identical to GPl-V because of material symmetry around the mid-plane). The least favourable distributions are GPl-O and GPl-V. We can also see that the increase of volume index n (i.e. moving towards more metal-rich FGM) decreases the fundamental frequency, which leads to the conclusion that the frequencies of GPls-reinforced FGM plates are intermediate to those of GPls-reinforced isotropic plates.

In Figure IV.14 we show the variation of fundamental frequency parameter $\overline{\omega}$ with porosity volume fraction for various power-indices. We can see that P-O has the least effect on natural frequencies, while P-X is the most disadvantageous distribution on frequencies. This is explained by the contrasting effects of these two distributions on bending stiffness coefficients as we have showed in Figure IV.10. The frequencies of P-A and P-V patterns always lie in an intermediate place, and for CI plate, they are are identical. For CR, CM, and MR FGMs, P-V cause less decrease than P-A.

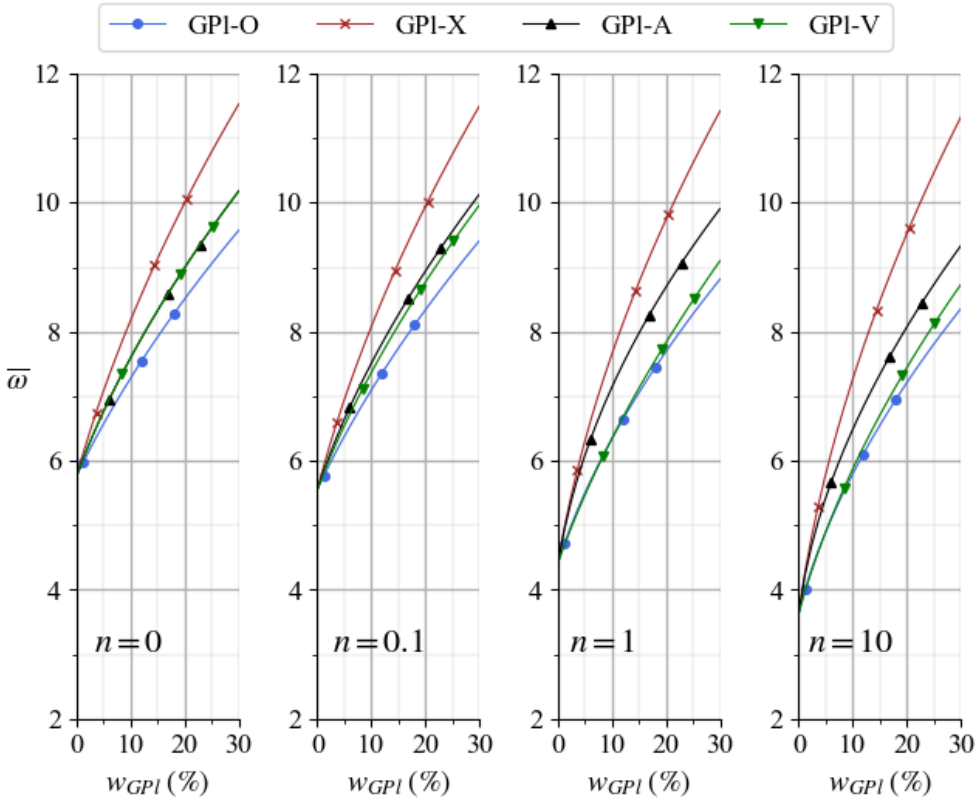

Figure IV.13: Evolution of non-dimensional frequency with GPls weight fraction for different FGMs.

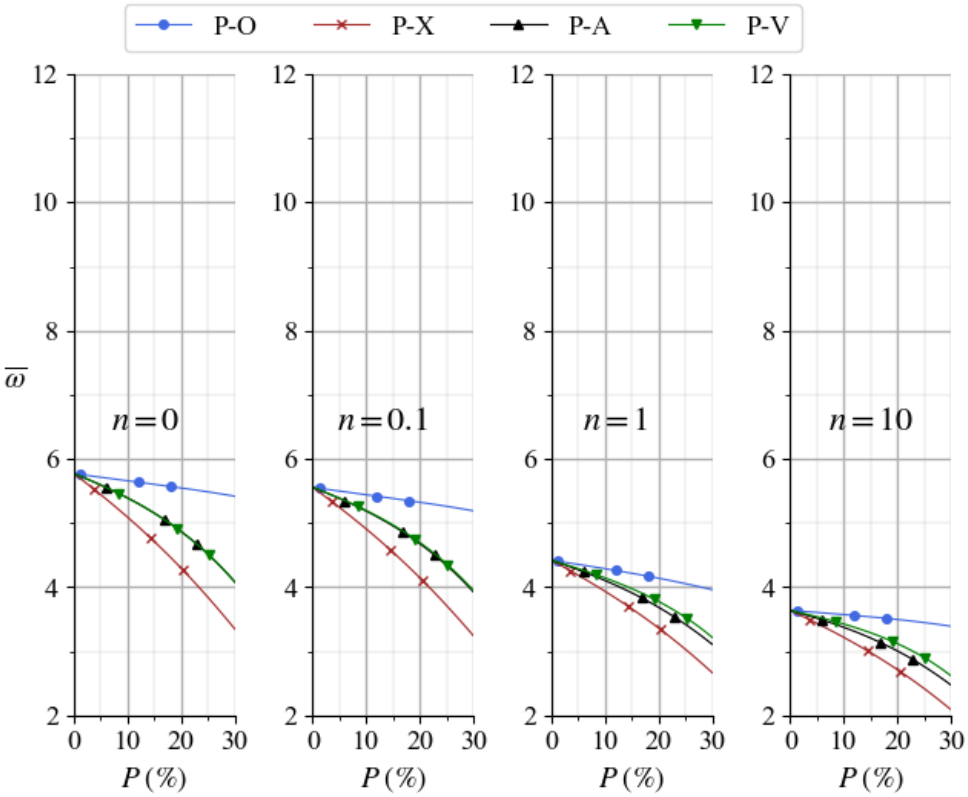

Figure IV.14: Evolution of non-dimensional frequency with porosity volume fraction for different FGMs.

A further parameter that affects the dynamic behaviour of FGM plates is the thickness ratio a/h. In Figure IV.15 we show the variation of the relative change of fundamental frequency against a/h for different GPls distributions with $w_{GPl}=5\%$. The relative change is defined by $\left(\left(\overline{\omega}-\overline{\omega}_{mat}\right)/\overline{\omega}_{mat}\right)\cdot 100$, where $\overline{\omega}_{mat}$ is the natural frequency of the FGM matrix plate sans GPls. In all configurations, the relative change by GPls takes a constant value for thickness ratios greater than 10. For thicker plates, the sensitivity to GPls shows slight changes but with no great significance. It is also seen that the increase of n will increase the relative effect of GPls addition.

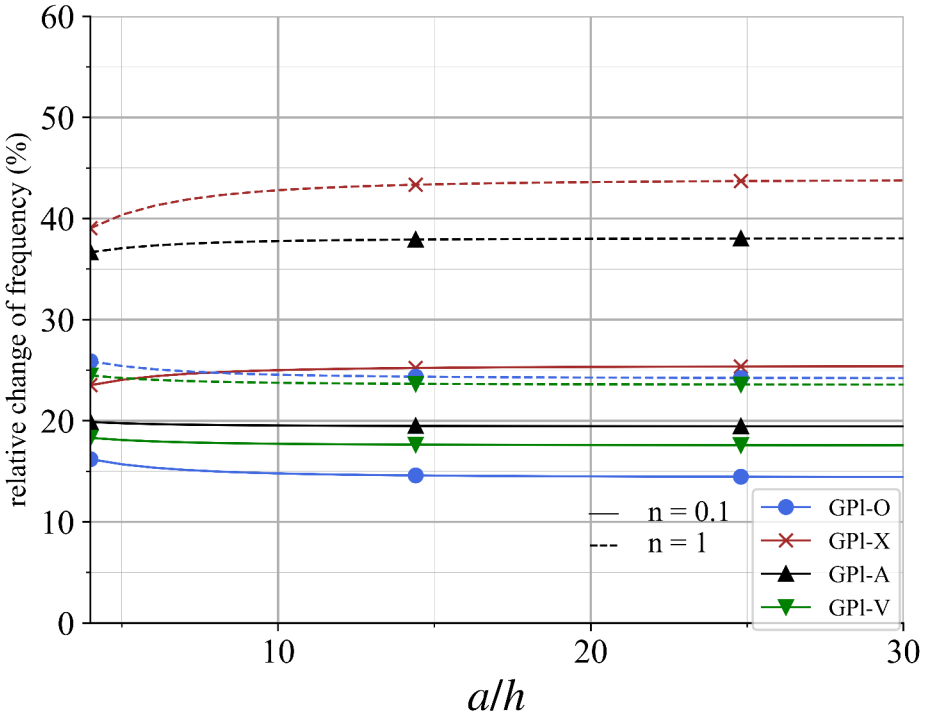

Figure IV.15: Relative change of natural frequency from the non-reinforced case for different thickness ratios (with w_{GPl}=5%).

Next we show in Figure IV.16 the variation of the first four non-dimensional frequencies with GPls (in GPl-A) for a moderately-thick FGM plate. It is found that $\overline{\omega}$ increases as the nano-additive content increases whatever is the vibration mode of the plate. It further shows that the natural frequencies of FGM plates decrease with the increase of metal fraction. In Figure IV.17 we analyse the same behaviour for thick FGM plate. The same remarks are obtained as with the moderately-thick plate. We can also see that the thickness ratio influences the modes frequencies, which are reduced from those of moderately-thick FGM plate, and have also approached to each others.

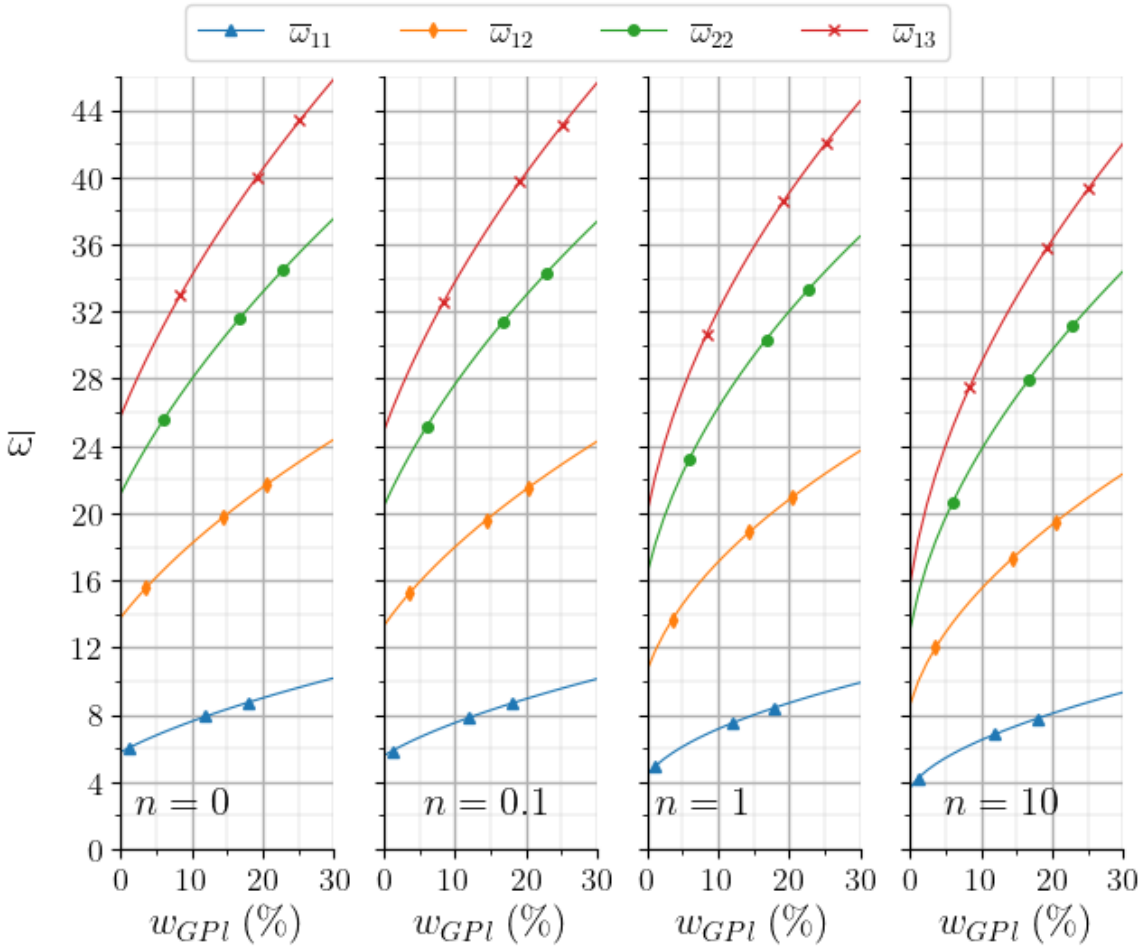

Figure IV.16: Variation of the first four frequencies with the increase of GPls weight fraction for different moderately-thick FGM plates (a/h=10).

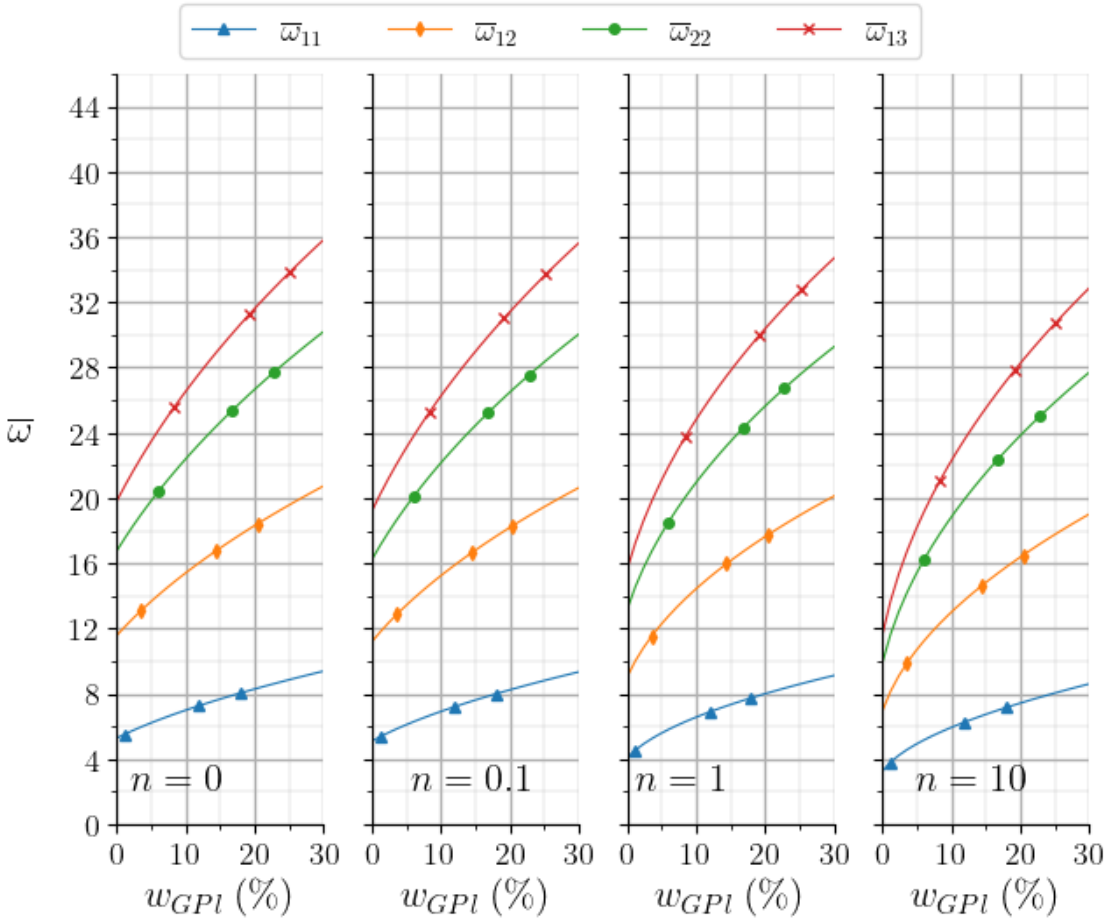

Figure IV.17: Variation of the first four frequencies with the increase of GPls weight fraction for different thick FGM plates (a/h=5).

In Figure IV.18 we present the first three modes shapes of vibration for an FGM plate with $b=2a$, $a/h=10$, $n=1$ and $P=5\%$ in P-O pattern. Dimensionless frequencies are given for the non-reinforced FGM and also for GPls-reinforced FGM with $w_{GPl}=5\%$ in GPl-X distribution. The relative increase of frequency is 44.2% for mode (1,1), 42.7% for mode (2,1), and 43.8% for mode (1,2), which makes very similar changes for the three modes. The rest of modes shapes for this FGM configuration until the ninth mode are given in our article [6].

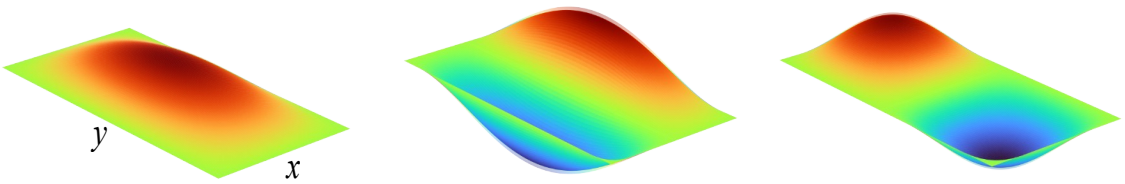

mode (1,1)
$\bar{\omega}$=2.7536 (without GPls)
$\bar{\omega}$=3.9703 (with 5% GPls)

mode (2,1)
$\bar{\omega}$=8.9558 (without GPls)
$\bar{\omega}$=12.7774 (with 5% GPls)

mode (1,2)
$\bar{\omega}$=4.3549 (without GPls)
$\bar{\omega}$=6.2611 (with 5% GPls)

Figure IV.18: First three modes shapes and dimensionless frequencies of a rectangular FGM plate with and without GPls.

IV.5.2 Bending response

IV.5.2.1 Validation examples

As we have mentioned earlier, the existing literature works on metal-ceramic FGM plates have focused only on FGMs with or without pores imperfections, but not with GPls reinforcement. Therefore, we will assess the validity of our analysis using the available three-dimensional solutions of metal-ceramic FGMs. The first validation example studies the non-dimensional deflection parameter $\overline{w}$ normalized to the exact solution of Nguyen and Nguyen-Xuan [212] for a square FGM plate carrying a sinusoidally-distributed load with various power-law exponents. The results are illustrated in Figure IV.19 for moderately-thick plate, and in Figure IV.20 for thick plate.

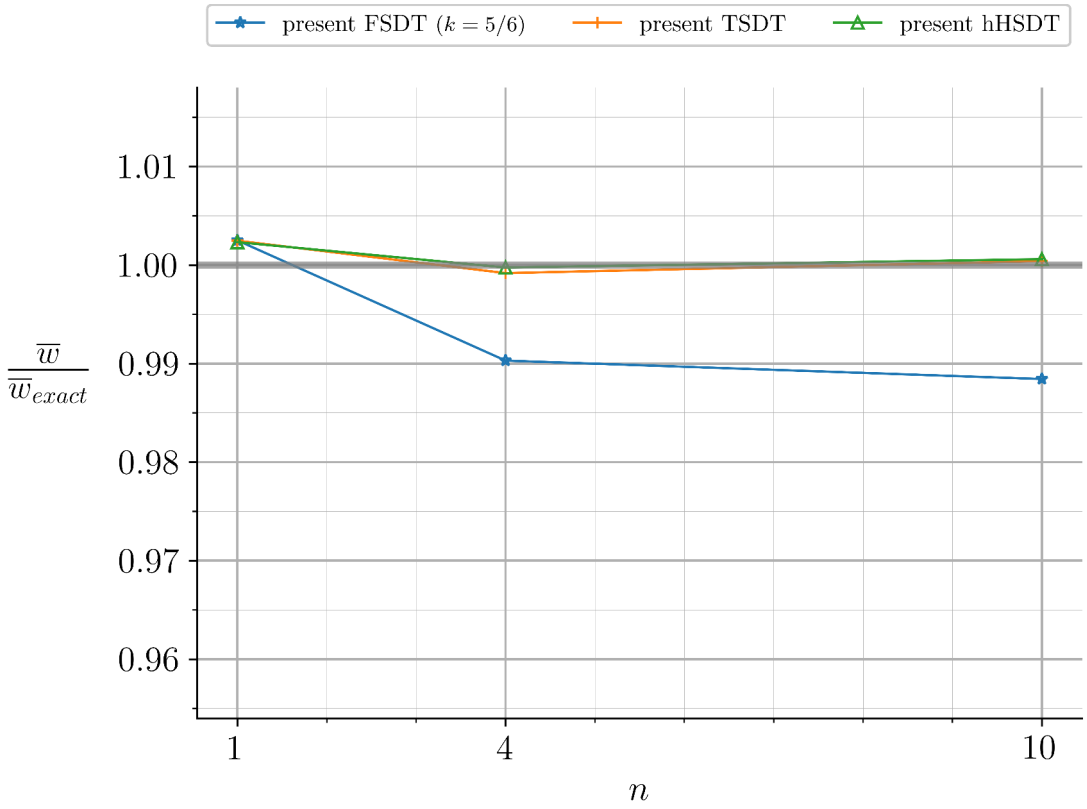

Figure IV.19: Deflection parameter normalized to the exact solution of reference [212] for a moderately-thick FGM plate (a/h=10).

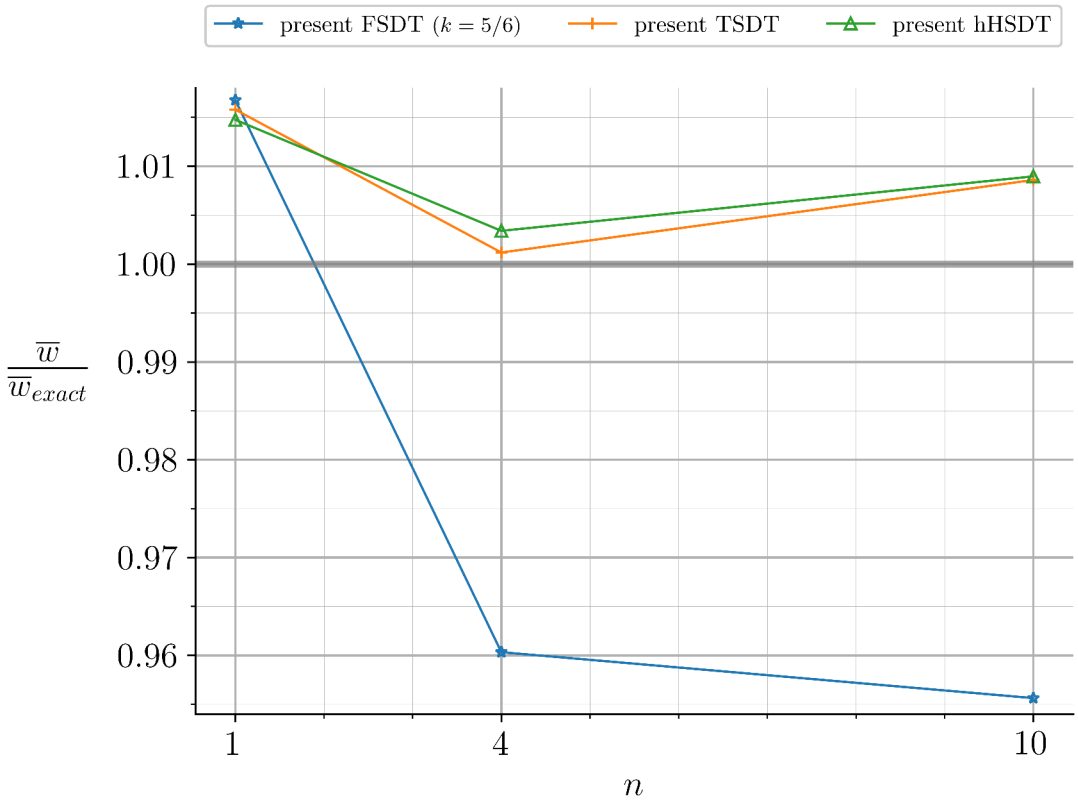

Figure IV.20: Deflection parameter normalized to the exact solution of reference [212] for a thick FGM plate (a/h=4).

Our method based on the hHSDT and TSDT shows excellent agreement with the three-dimensional elasticity solution, even for thick plates. These HSDTs yield close results to each others overall, and their maximum error for moderately-thick and thick plates was 0..25 % and 1.58 %, respectively. On the other hand, the accuracy of the FSDT is much lower, and the maximum error was 1.16 % for the moderately-thick plate, and 4.44 % for the thick plate. It is also remarked that the FSDT accuracy is good and comparable to the HSDTs for small power indices, but it becomes unreliable for large power-law exponents, which was also observed in the vibration analysis.

IV.5.2.2 Parametric analysis

After validating our bending solution method, we start to analyse GPls-reinforced FGM plates under sinusoidally-distributed loads. The transverse load is taken positively (ie traction), which allows to obtain positive values of deflection. We show in Figure IV.21, Figure IV.22, Figure IV.23, and Figure IV.24 the change of centre deflection parameter $\overline{w}$ with GPls weight-fraction for $n=0$ (CI plate), $n=0.1$ (CR plate), $n=1$ (CM plate) and $n=10$ (MR plate), in that order. Isotropic metal plate was not considered since the similar case of ceramic isotropic (CI) plate was considered. Porosities are included by $P=10\,\%$ in P-O distribution.

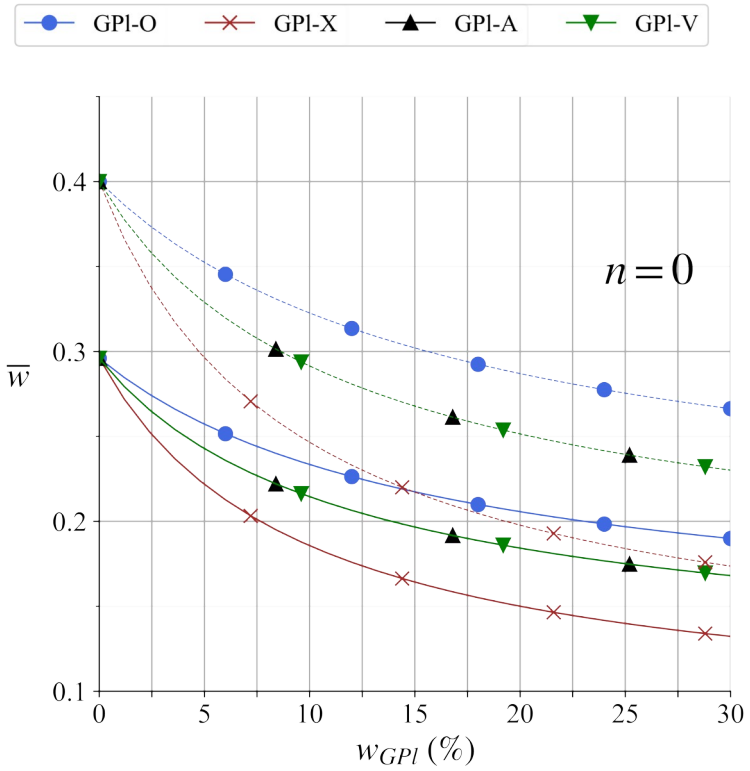

Figure IV.21: Variation of non-dimensional deflection with GPls weight fraction for solid (–) and porous (--) CI FGM.

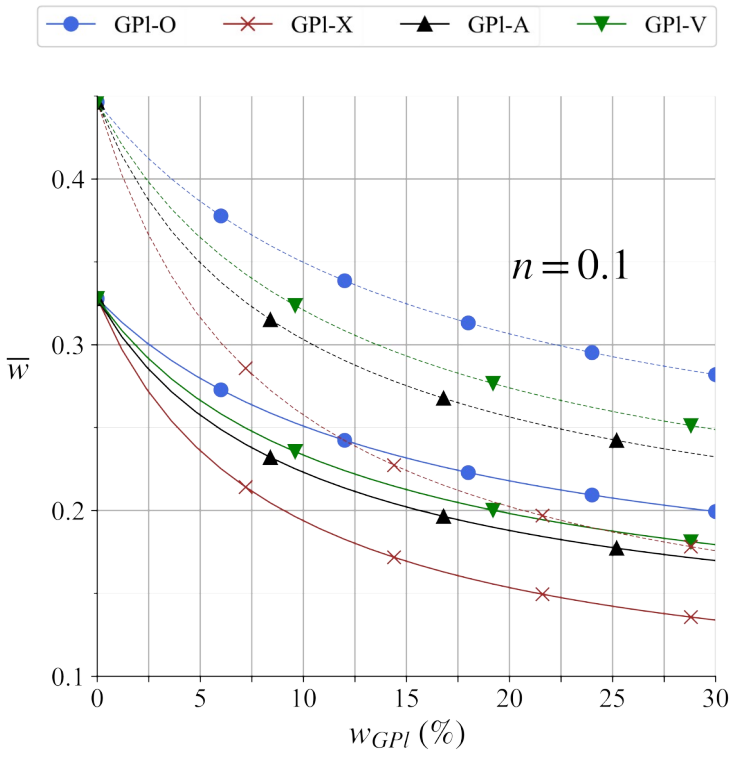

Figure IV.22: Variation of non-dimensional deflection with GPls weight fraction for solid (–) and porous (--) CR FGM.

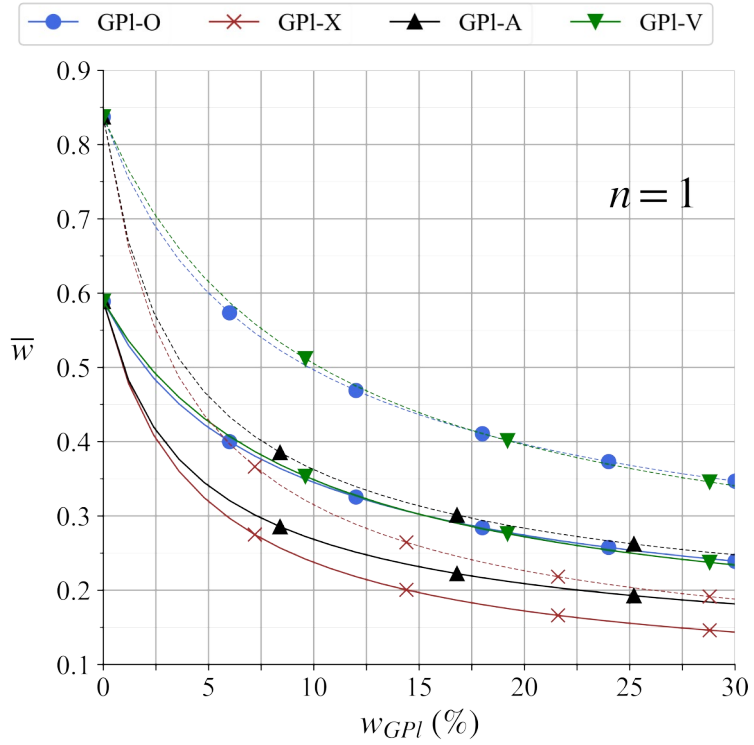

Figure IV.23: Variation of non-dimensional deflection with GPls weight fraction for solid (–) and porous (--) CM FGM.

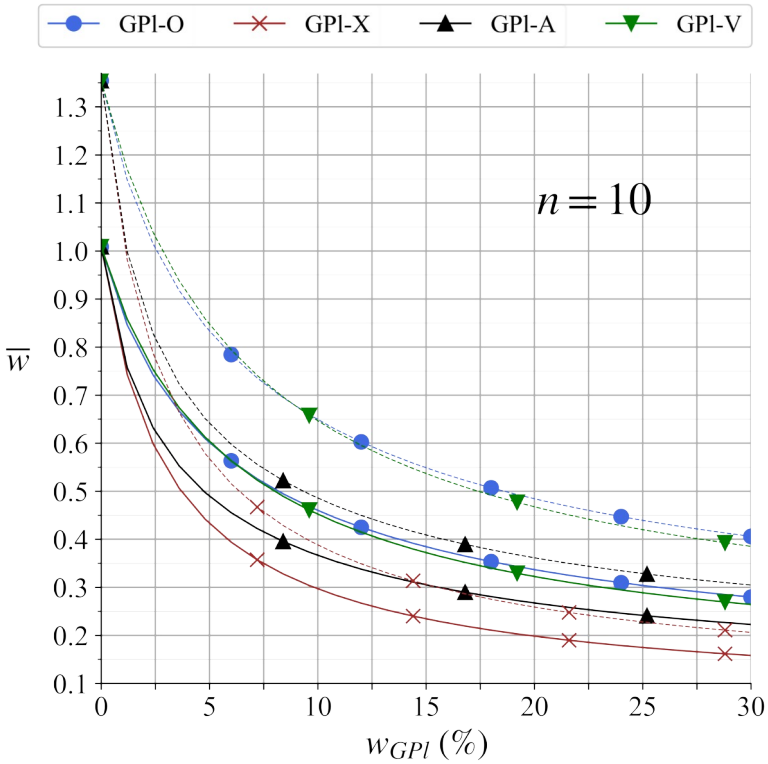

Figure IV.24: Variation of non-dimensional deflection with GPls weight fraction for solid (–) and porous (--) MR FGM.

We can see that GPls incorporation reduces the plate's deflection in all distributions, and that the greatest reduction occurs in GPl-X, followed secondly by GPl-A. The least reduction occurs in GPl-O for CI and CR FGMs, and in both GPl-O and GPl-V for CM and MR FGMs. For CI FGM plate, GPl-A and GPl-V results coincide since they are equivalent distributions for symmetric plates. It can be also seen that the slope of the plots decreases as the weight fraction of GPls increases, indicating that the relative change in deflection decreases for higher amounts of nano-additive. It is also observed that increasing n increases the centre deflection, which results from the lower stiffness of metal compared to ceramic. Porous FGMs will have increased deflections due the impact of porosities on stiffness. The change from non-porous case seems to be insignificantly changed through the range of GPls weight-fraction.

Figure IV.25, Figure IV.26, Figure IV.27 and Figure IV.28 show the effects of GPls on the mid-plane extension parameter $u_{z=0}=u_0$. Initially when no GPls are included, the mid-plane extension of CI plate is zero because of material symmetry. But for non-symmetric CR, CM and MR FGMs, always at $w_{GPl}=0\%$, non-zero values of extension occurs because of the existence of bending-extension coupling that causes mid-plane extension in this bending state.

When GPls amount is increased in CI FGM, u_0 increases for GPl-A and GPl-V in opposite but equal magnitudes, but it remains null in for symmetric GPl-O and GPl-X distributions. For the other FGMs, the mid-plane extension is reduced with increasing GPls in GPl-O, GPl-X and GPl-A. GPl-A has the greatest effect on u_0, which will vanish in this distribution at 2.5%, 7.5%, and 3.75% of nano-additive in CR, CM, and MR FGMs, respectively. At those points, the elastic modulus was equilibrated by GPls with respect to the middle plane, which resulted in uncoupled response of the FGM plate, then bending the plate will no longer causes mid-plane extension.

It is also noted that porosity increases the longitudinal displacement in absolute value, which reflects its weakening effect on the FGM plate stiffness.

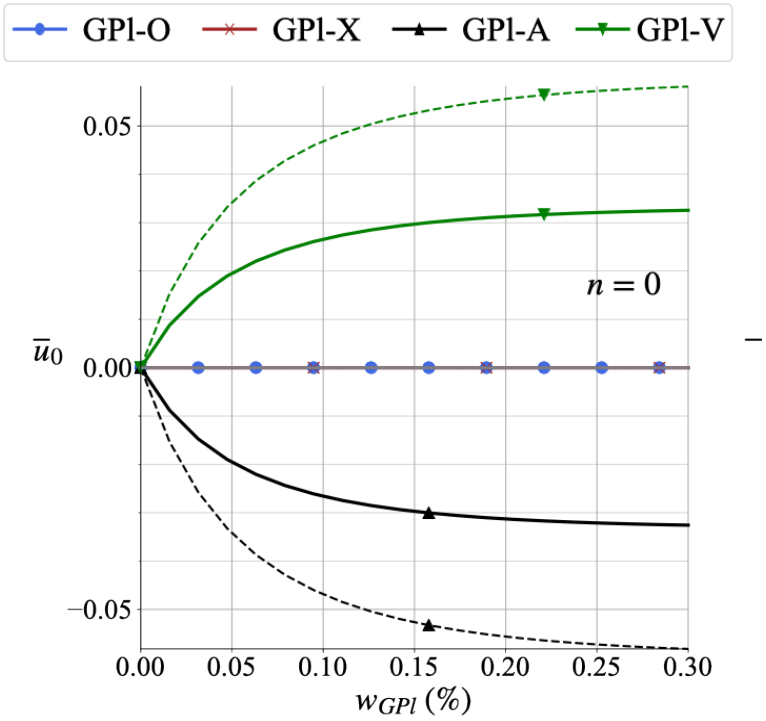

Figure IV.25: Variation of non-dimensional mid-plane extension with GPls weight fraction for solid (–) and porous (--) CI FGM plate.

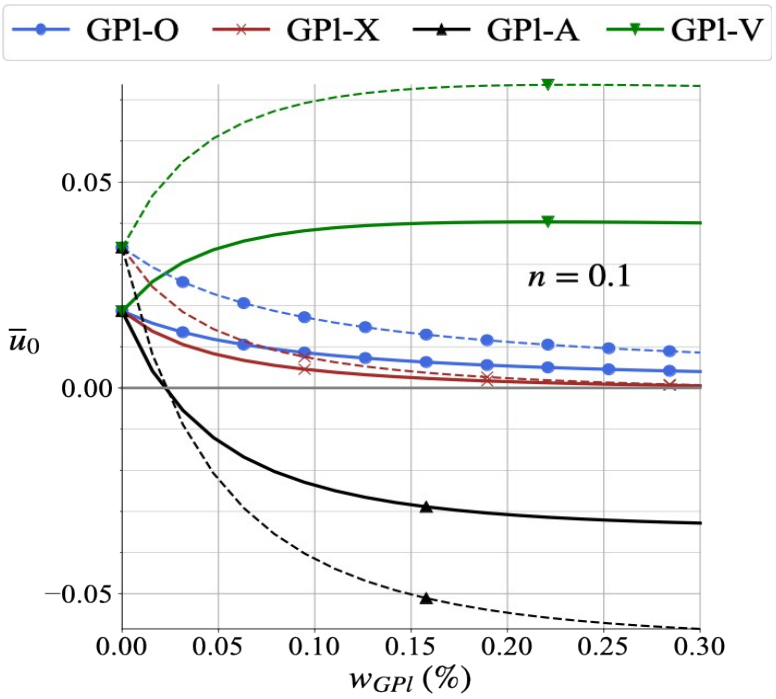

Figure IV.26: Variation of non-dimensional mid-plane extension with GPls weight fraction for solid (–) and porous (--) CR FGM plate.

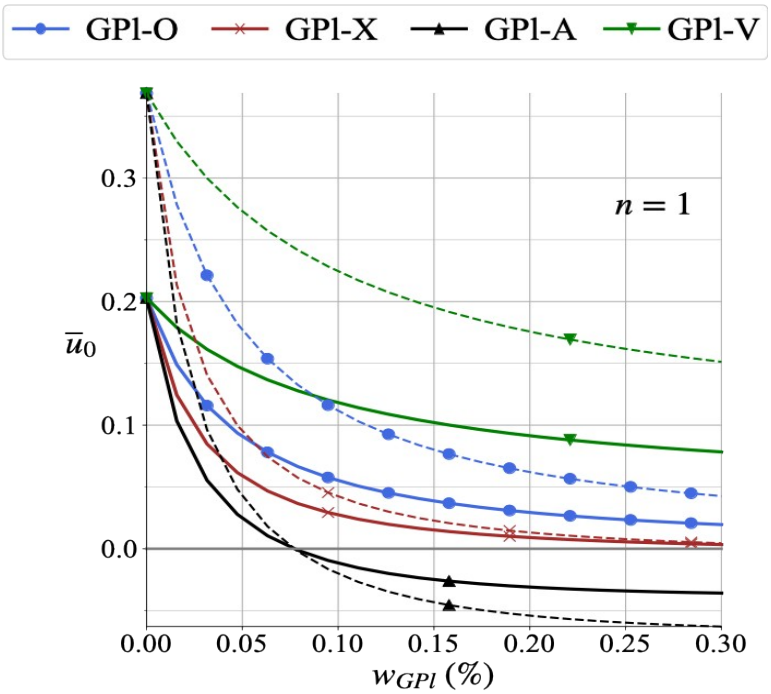

Figure IV.27: Variation of non-dimensional mid-plane extension with GPls weight fraction for solid (–) and porous (--) CM FGM plate.

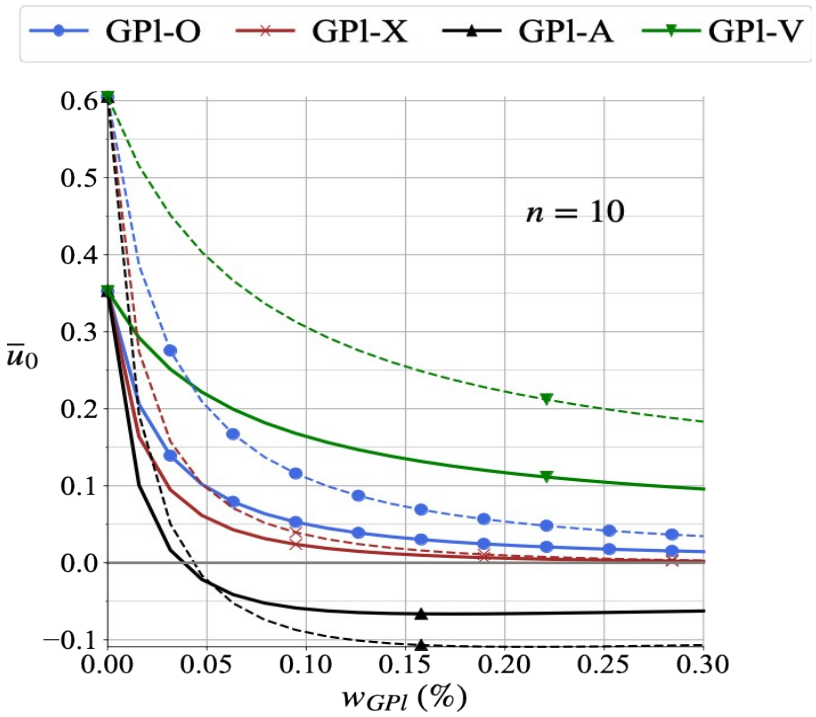

Figure IV.28: Variation of non-dimensional mid-plane extension with GPls weight fraction for solid (–) and porous (--) MR FGM plate.

In Figure IV.29, Figure IV.30, Figure IV.31 and Figure IV.32 we show the effects of GPls on through-thickness distribution of bending stress parameter $\overline{\sigma}_x$ for FGM plates with $n=0$, $n=0.1$, $n=1$ and $n=10$, respectively. The FGMs are reinforced by $10\,\%w_{GPl}$.

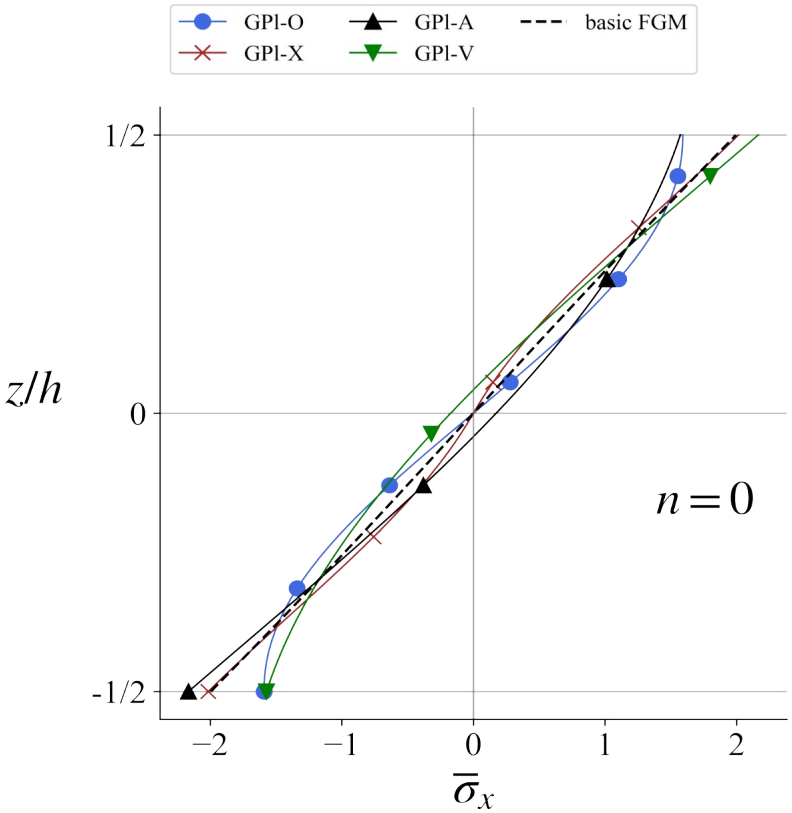

Figure IV.29: Through-thickness variation of dimensionless bending stress of CI FGM plate with different GPls distributions.

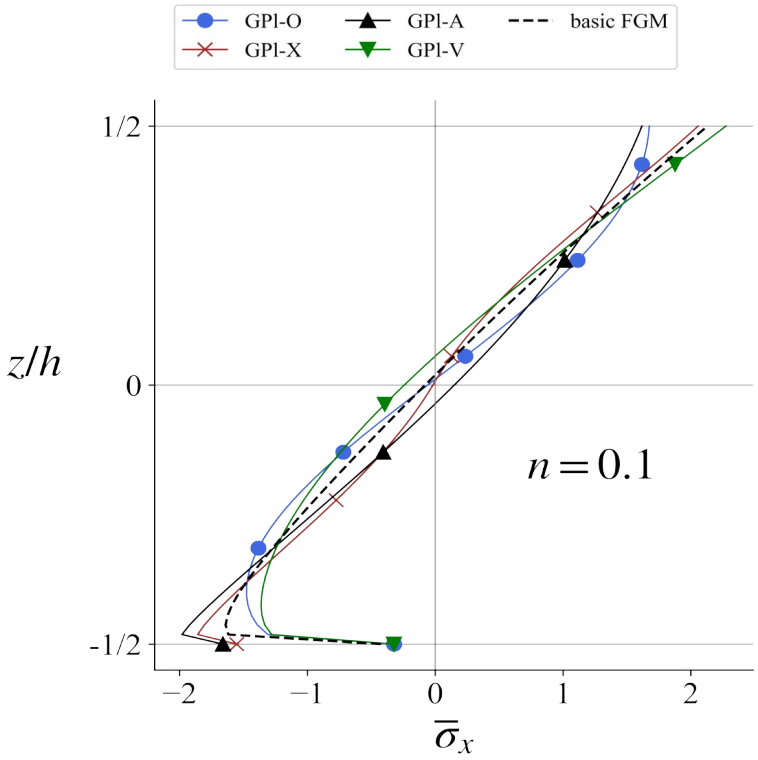

Figure IV.30: Through-thickness variation of dimensionless bending stress of CR FGM plate with different GPls distributions.

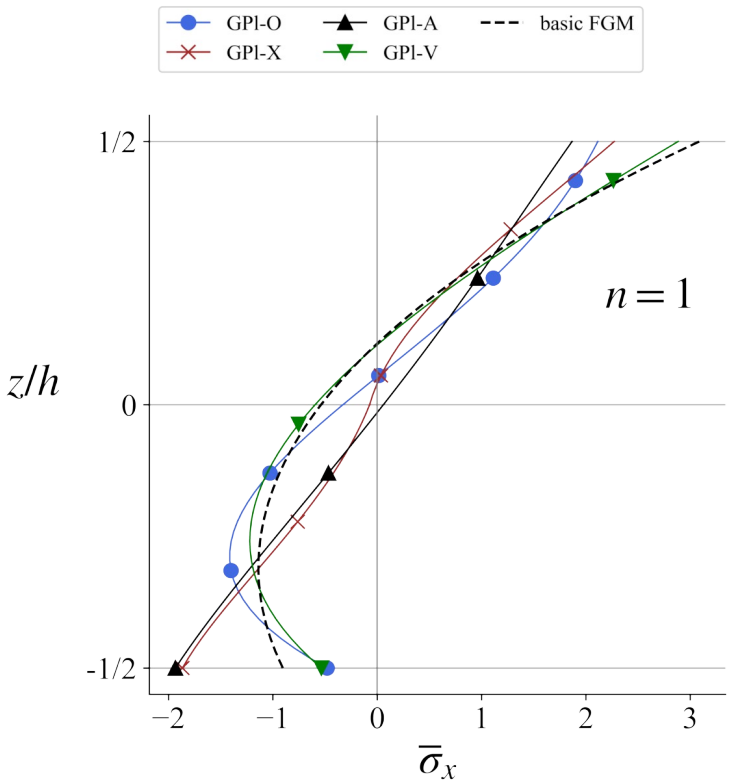

Figure IV.31: Through-thickness variation of dimensionless bending stress of CM FGM plate with different GPls distributions.

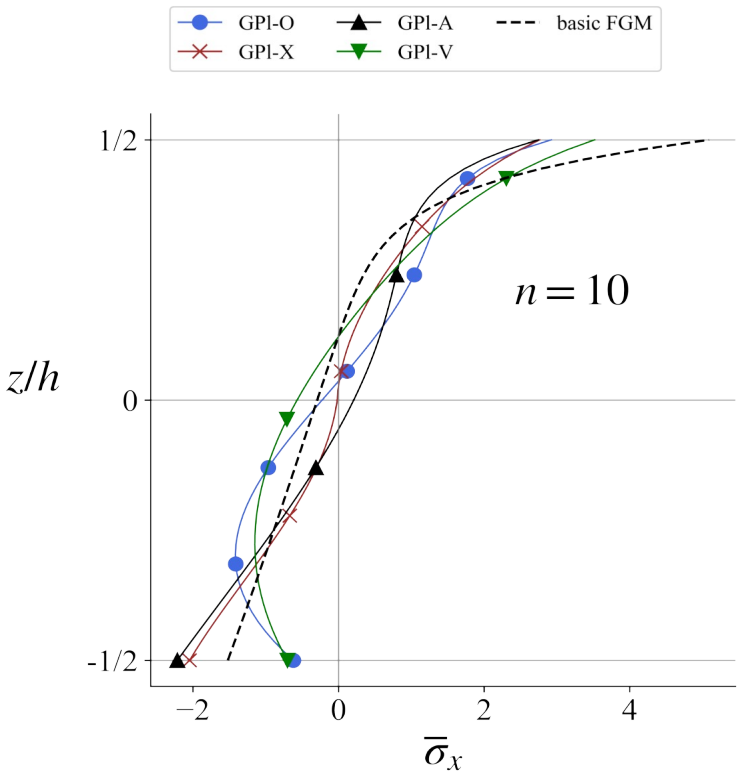

Figure IV.32: Through-thickness variation of dimensionless bending stress of MR FGM plate with different GPls distributions.

We can see that the normal stress is always tensile at the upper region and compressive at the lower region, but the transition point (which determines the neutral plane) changes with the FGM composition and GPls distribution.

Focusing on the non-reinforced FGMs, we can see that $\overline{\sigma}_x$ varies linearly in CI FGM and has zero value in the mid-plane. In CR FGM, it varies quasi-linearly where ceramic is dominant but reduces abruptly in the lowermost region because metal fraction increases rapidly their. In CM FGM, $\overline{\sigma}_x$ varies non linearly and vanish in displaced position from the mid-plane. In MR FGM, $\overline{\sigma}_x$ varies quasi-linearly in the lower region where metal is dominant, but at the uppermost region it increases suddenly following the rapid increase of ceramic volume fraction.

As for reinforced FGMs, we can see that GPls change the bending stress in noticeable manners which are quit complicated. GPl-O decreases the maximum tensile stress at the upper region and maximum compressive stress at the lower region in all FGMs, but it increases the stress magnitude in the proximity of the middle region. Other GPls distributions cause a decrease of maximum tensile stress in most FGMs. Maximum compressive stress in the lower region is increased by GPl-X and GPl-A, and is reduced by GPl-O and GPl-V.

Next we investigate the effects of GPls on transverse-shear of FGM plates. This time we fix the FGM composition by $n=1$, and instead we vary the plate theory to see whether the traction-free boundary condition is satisfied in each case or not. Figure IV.33 shows the non-dimensional parameter of transverse shear stress $\overline{\sigma}_{xz}$ using the FSDT.

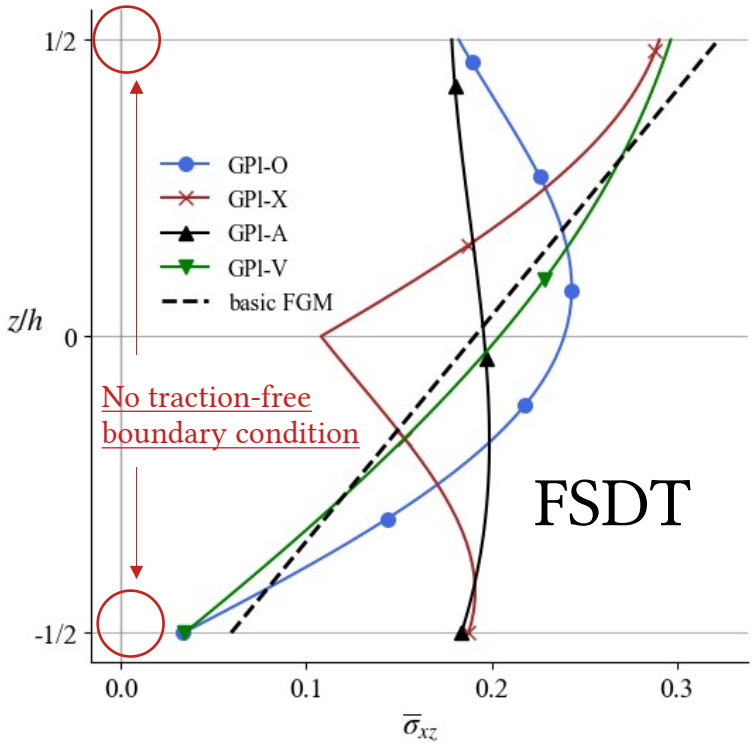

Figure IV.33: Through-thickness variation of $\overline{\sigma}_{xz}$ for different GPls distributions using the FSDT calculation (with k=5/6).

We can see that the transverse shear stress does not vanish at the top and bottom surfaces with the FSDT calculation, which violates the boundary conditions of no traction at the bottom and top surfaces of the FGM plate. Also, $\overline{\sigma}_{xz}$ should follow a parabolic-like through-thickness variation, which isn't satisfied either.

In Figure IV.34 and Figure IV.35 we use Reddy's TSDT and the hHSDT for transverse shear stress calculation. It is easily seen that both HSDTs satisfy the traction free boundary condition by having $\overline{\sigma}_{xz}(z=\pm h/2)=0$. For the base FGM plate, transverse shear stress varies parabolically but non-symmetrically, because of transverse anisotropy that results from non-symmetric elastic modulus across the FGM. On the other hand, GPl-A FGM exhibits a perfect parabolic variation with mid-plane symmetry, as an isotropic plate would have. GPl-O also has a nearly-symmetric profile of transverse shear stress.

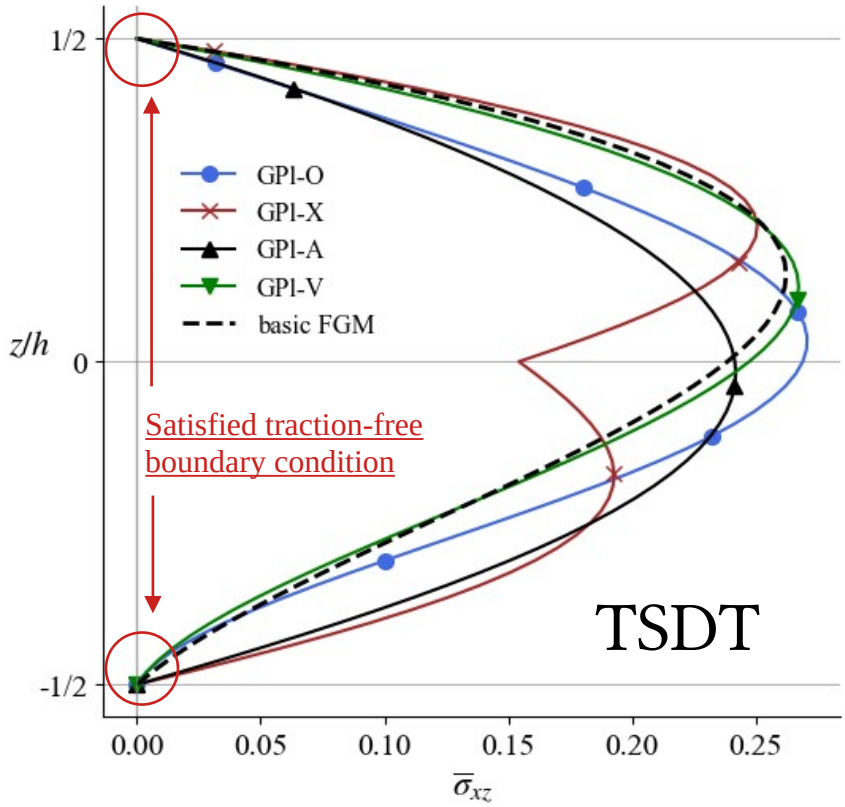

Figure IV.34: Through-thickness variation of $\overline{\sigma}_{xz}$ for different GPls distributions using the TSDT calculation.

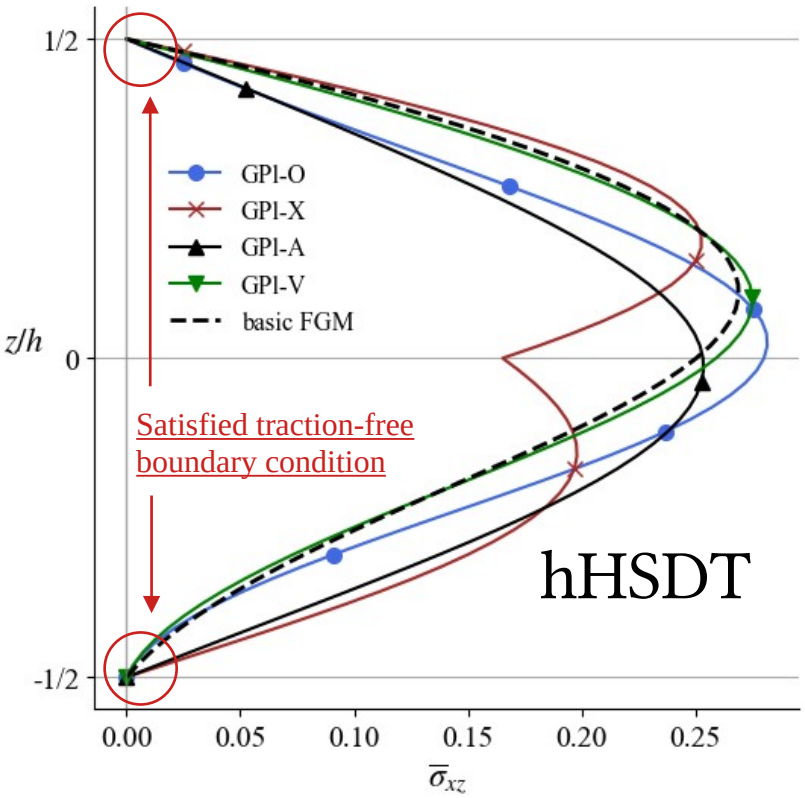

Figure IV.35: Through-thickness variation of $\overline{\sigma}_{xz}$ for different GPls distributions using the hHSDT calculation.

GPl-X affects the transverse shear stress by inducing sharp kink in the centre region. It is also noted that the maximum shearing stress in the initial FGM was decreased in both GPl-X and GPl-A, which helps to provide larger resistance to shear failure in FGM plates.

The comparison of the TSDT and hHSDT shows very similar features with hardly observed differences. The positions of maximums and minimus are also the same. On the other hand, the FSDT maximum and minimum values are totally erroneous and unreliable.

IV.5.3 Buckling response

IV.5.3.1 Validation examples

To validate the accuracy of our method in predicting the critical buckling loads we illustrate in Figure IV.36 the results of uni-axial buckling parameter:

$$\hat{N} = \frac{1-\nu^2}{Eh} \cdot N$$

We consider in this example a GPls-reinforced laminated plate and compare our results with the quasi-3D hHSDT solution of Ghandourah et al. [213] that considers the stretching effect. The epoxy matrix data are: $E = 3$ GPa and $\nu = 0.34$.

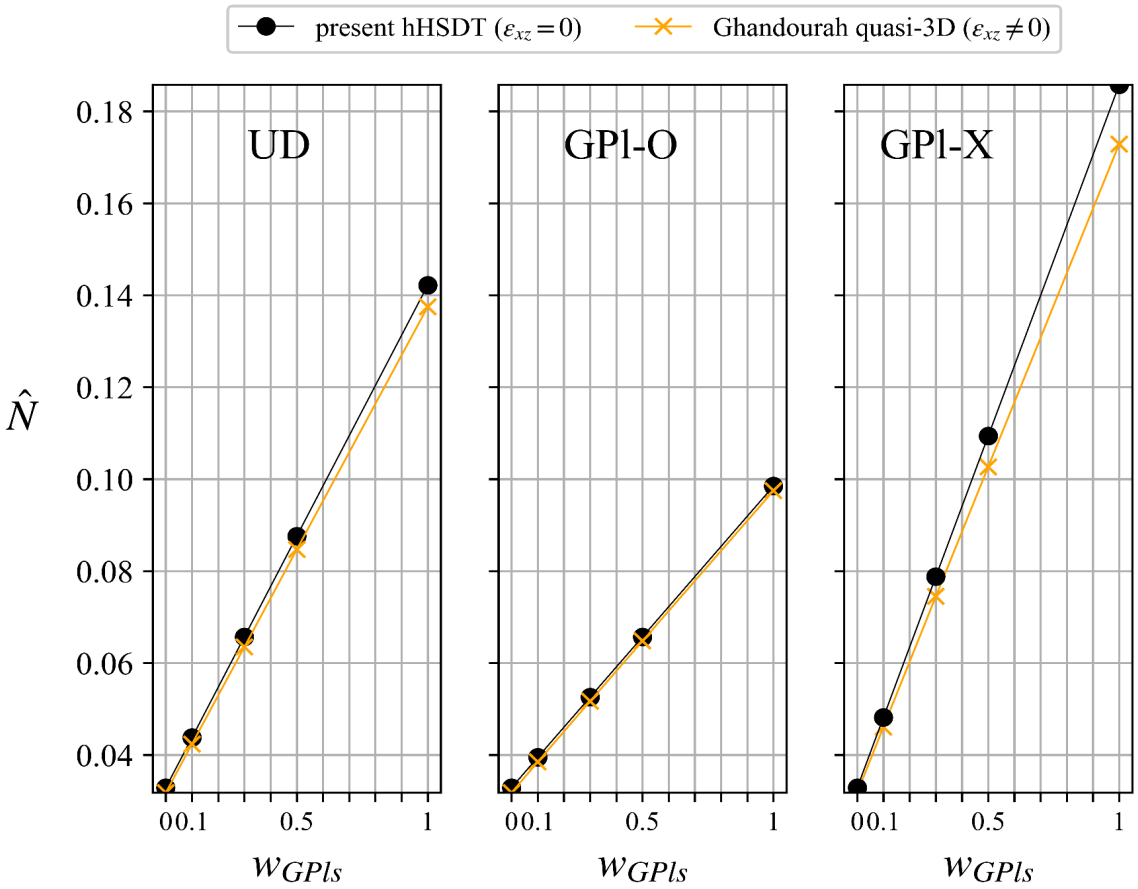

Figure IV.36: Validation of uni-axial buckling results of laminated plates reinforced with GPls in various distributions.

The comparison of our results with the quasi-3D solution for each distribution mode reveals excellent accuracy in predicting the critical buckling loads of FGM plates with GPls reinforcement.

IV.5.3.2 Parametric analysis

After validating our buckling analysis we will study the buckling of porous GPls-reinforced FGM plates. The typical bifurcation-type buckling does not occur in non-symmetric FGM plates –except the case of a completely-clamped plate–, which is caused by the existence of bending–extension coupling in this type of FGMs [6]. Therefore, we will consider a different symmetric FGM with a metal-rich core and ceramic-rich surfaces. This FGM is modelled by the following modified volume-fraction function:

$$V(z)=2\left|\frac{z}{h}\right|^{n} \tag{IV.4}$$

This volume-fraction rule will result in symmetric variations as illustrated bellow:

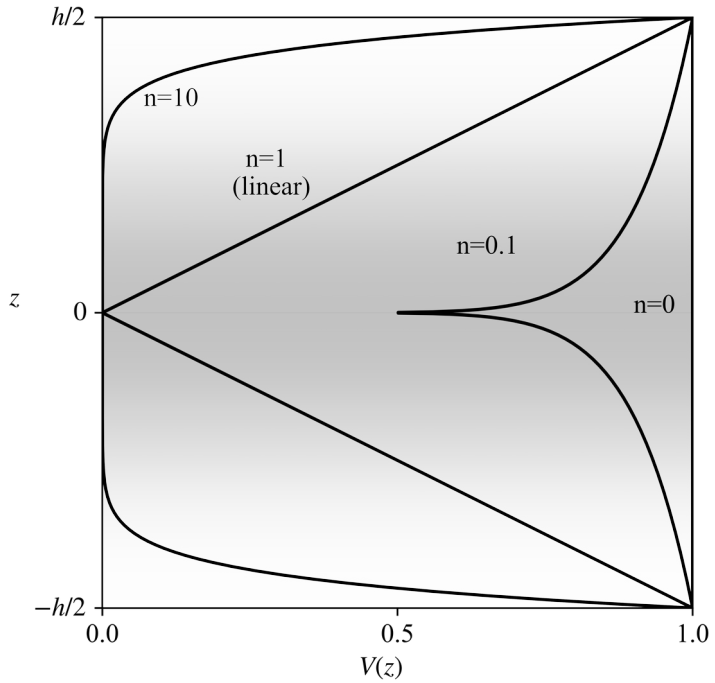

Figure IV.37: Symmetric ceramic-metal-ceramic FGM with various power-law indices.

Adopting this rule, the variation of the critical buckling load for a square FGM plate with GPls volume-fraction is plotted in Figure IV.38 for CR, CM and MR FGM plates with $a/h=10$. Porosity parameter is also considered by 15% volume fraction in P-O and P-X distributions. P-A and P-V were not included as they will cause asymmetry around the mid-plane, which renders the buckling impossible. The buckling mode considered here is the first mode: $(m,n)=(1,1)$.

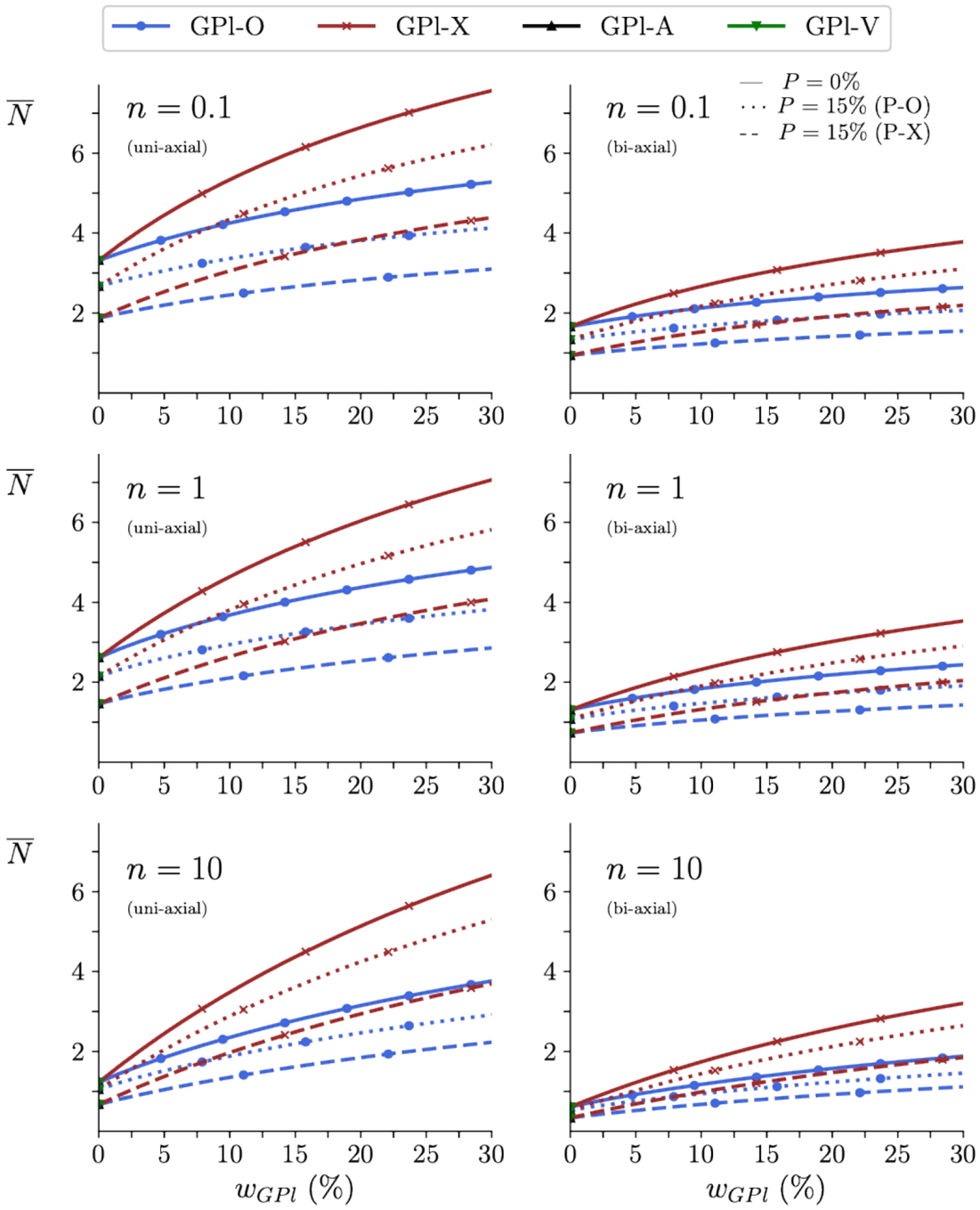

Figure IV.38: Variation of non-dimensional critical buckling load for GPls-reinforced FGM plates with and without porosities.

We can see that the buckling load increases with the increase of GPls weight-fraction. The gains are greater in GPl-X than GPl-O, and the difference between the two distributions becomes larger with the increase of nano-additive amount. Buckling did not occur in GPl-A and GPl-V, which confirms that non-symmetric simply-supported plates do not experience this phenomenon.

We observe also that porosities will reduce the supported buckling load by the FGM plate, with a greater impact in P-X than P-O. Increasing the power-law exponent will also reduce the buckling loads in a continuous manner, indicating that the buckling loads of GPls-reinforced FGM plates lie between those of GPls-reinforced isotropic plates. The case of bi-axial compression shows similar results and trends, except the magnitude of loads which is precisely halved (because the square plate is stressed from two direction instead of one).

In the next example we will extend our analysis from square FGM plates to rectangular ones. Unlike beams which normally buckle in the first mode (ie with a single bump), plates will buckle in modes different than the first if they have rectangular shapes. To find the mode number at which a rectangular plate of a given aspect ratio will buckle at, an inspection must be done by plotting the buckling loads against the aspect ratio a/b for different values of the half-wave number m. The resulting graph for a CI FGM plate is presented in Figure IV.39.

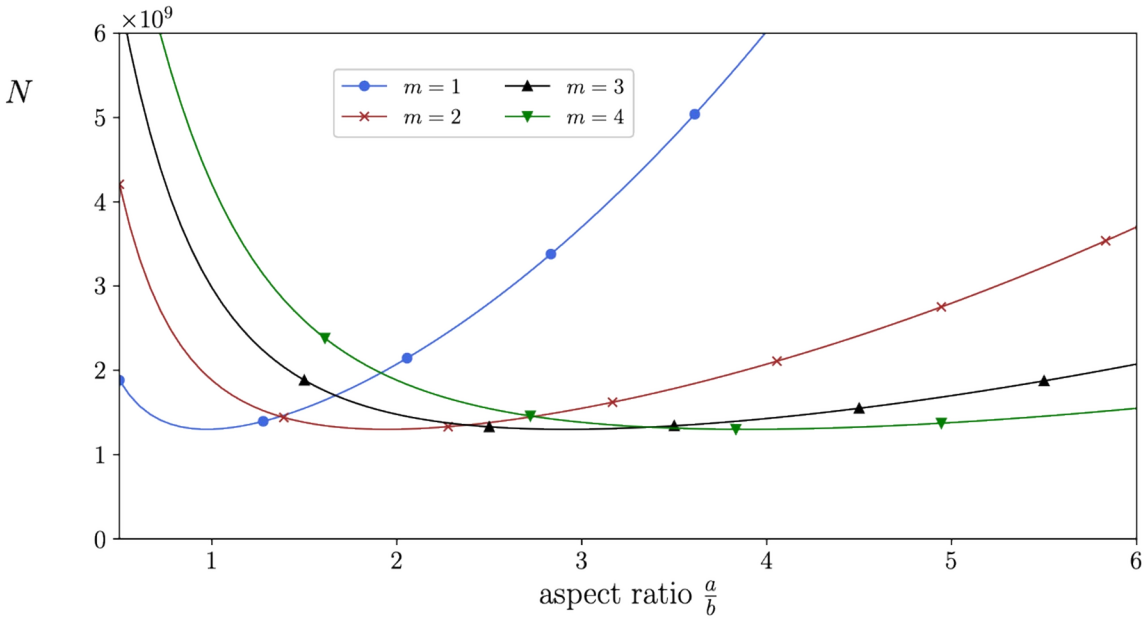

Figure IV.39: Critical buckling load versus the aspect ratio *a/b*. *m* indicates the buckling mode number along the *x* direction (*a/h*=10).

For a fixed aspect ratio in the graph above, increasing the compressive load to the critical level will cause the plate to buckle in the mode m that has a minimum N. For example, the square plate ($a/b=1$) can support a compressive load up to $N \approx 1.3 \cdot 10^9$ N/m, at which buckling will occur in the first mode with a single hump. For a rectangular plate with $a/b=2$, buckling will occur in the second mode with two humps on each side of the plane.

Physically, the buckled rectangular plate divides itself into a whole number of sub-squares which alternate in convex and concave humps. In the y-direction, which is unloaded, only one half-wave shows. For a better visualization of this phenomenon, we have joined in Appendix C the buckling modes shapes of rectangular FGM plates under uniaxial loading for multiple length-to-width ratios. We like to mention that these useful graphs were accomplished using Matplotlib Python library.

Next, the influence of grading exponent on uni-axial buckling load is studied in Figure IV.40 for rectangular FGM plates with different length-to-width ratios. We can also see here that the buckling mode changes with the aspect ratio of the FGM plate, and the transition from one mode to another takes place for the same aspect ratio for the different FGMs (ie, it is independent of the plate composition). The increase of FGM power-law exponent reduces the critical buckling loads, which is a consequence of the change towards softer metal-rich FGMs. It is interesting to note that for a fixed FGM power-law index, the critical buckling load reduces with the increase of aspect ratio from 0.5 to a minimum of 0.9 approximately, and then it increases until $a/b \approx 1.3$, where it shifts to the second mode and repeats the same variation, and so on.

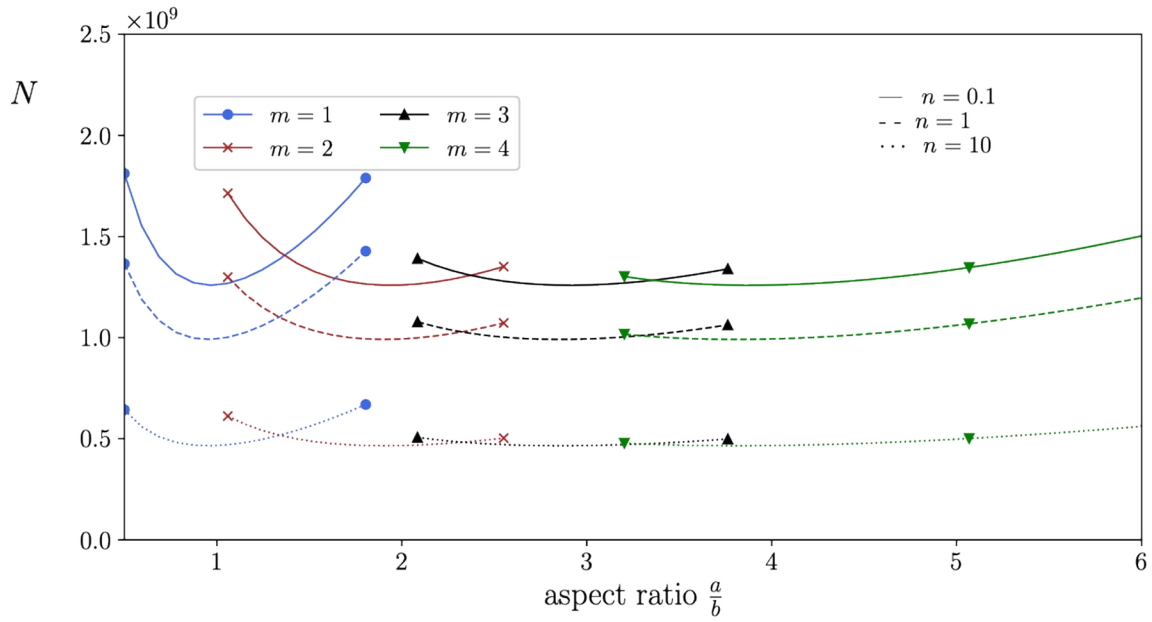

Figure IV.40: Critical buckling load versus the aspect ratio for different FGM gradation indices.

The influence of GPls on buckling loads is investigated in Figure IV.41, which reveals that nano-additives increase the resistance to buckling, and that the enhancement is exactly the same for different aspect ratios. It is also interesting

that the absolute increase in critical buckling loads is higher for the first 5%w_{GPls}, and adding another 5% will continue to increase the buckling load but with less magnitude. This means that that the relative effect of GPls on buckling resistance is most significant in the first amounts and decreases afterwards. This conclusion is consistent with what we have found on GPls effects on vibration frequencies [6].

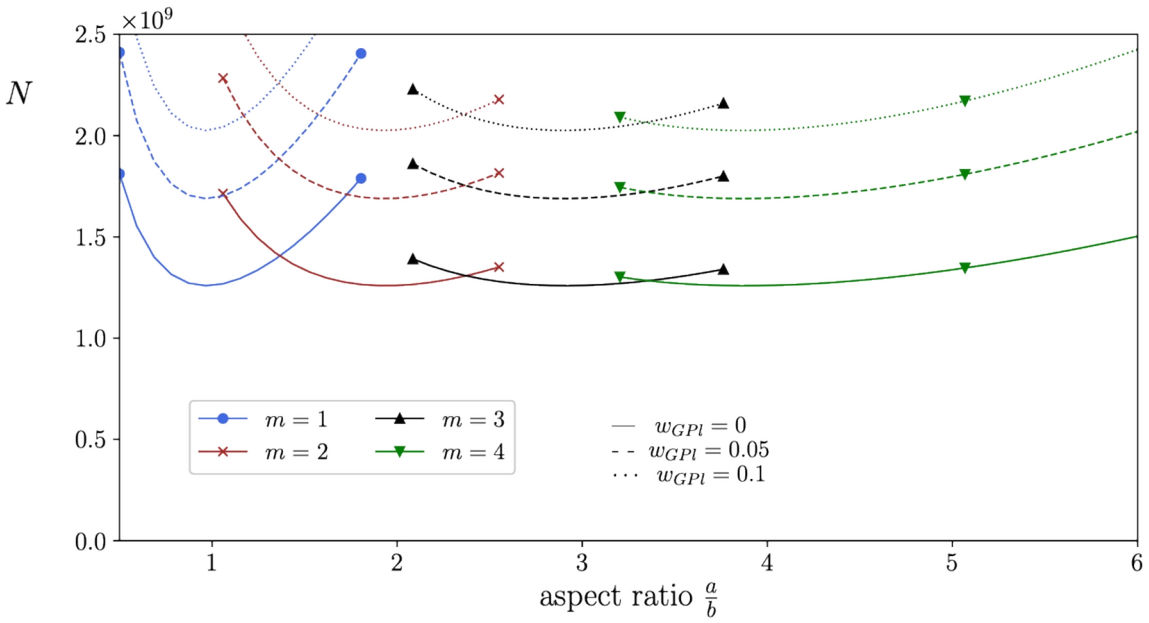

Figure IV.41: Critical buckling load versus the aspect ratio for different values of GPls weight fraction (n=0.1).

Conclusion

Summary and key results

We have investigated in this thesis the free vibration, static bending, and buckling behaviours of rectangular metal-ceramic FGM plates with porosities defects and GPls reinforcements (porous GPls-reinforced FGM plates). We started the theoretical analysis by the definition of the FGM power-law, in the constitutive aspect, and in parallel the choice of the HSDT and displacements field model, in the kinematic aspect. The resulting deformation field satisfies the boundary conditions of zero traction at the upper and lower surfaces.

By adopting the assumption of linear elasticity to obtain stresses, and by applying the principle of Hamilton, we derived the differential equations of equilibrium. These equations were then solved by using Navier's analytical method for a simply-supported plate.

Solution was carried out using a set of Python codes that were developed in-house. We have found during this research experience that the line-by-line programming method has many advantages, which appeared in the richness of parametric examples that we could treat, and also in the graphical presentations of results. Therefore, we have concluded that programming scientific codes is a more efficient way to investigate structural mechanics problems than computational simulation. In validation examples, our programmed method showed very good accuracy compared to the exact solutions based on meshed or meshless simulation methods. We note that calculation time was of the order of seconds only, which is a great advantage over simulation methods that may take minutes or even hours, depending on the refinement of mesh.

After confirming our method's efficiency in each of the dynamic, static, and stability analyses, we have carried out a number of parametric investigations, which consider a wide range of parameters relating to the base-FGM composition, GPls amount and distribution, porosities amount and distribution, and geometric dimensions of the FGM plate.

The obtained results of this work are summarized as follows:

- The present method and mathematical models can be applied efficiently to study the mechanical problems of elastic FGM plates.

- In the validation examples, the generalized plate formulation showed excellent accuracy even for thick plates, and in particular with the adopted hHSDT.
- Reddy's TSDT also yielded very accurate results.
- The FSDT is obviously less accurate than 2-D HSDTs, and significantly less than the exact 3D solution.
- HSDTs slightly underestimate the natural frequency, while the FSDT largely overestimates this quantity.
- HSDTs give very close deflection results to the exact solution, but the FSDT results are highly underestimated.
- HSDTs satisfy the boundary condition of zero transverse stresses at the bottom and top surface of the FGM plate, which is totally neglected by the FSDT.
- We have found that the FSDT is inaccurate to a large degree for:

  a) thicker plates,

  b) larger values of FGM power-index (that is, more metal-rich plates).

  c) calculating the magnitude and distribution of transverse shear stress.
- Increasing power-law index, which corresponds to the increase of total metal fraction, will reduce the rigidity of the FGM plate. This will lead to lower frequencies, larger deformations, and lower buckling resistance capacity.
- GPls have a positive impact on the FGM stiffness, which is reflected in increased natural frequency, reduced deflection and membrane extension, and higher critical buckling loads.
- GPl-X is the most advantageous distribution for a given amount of nano-additive, followed by GPl-A. The latter has the interesting effect of reducing and vanishing the bending-extension coupling at certain weight fractions.
- Uncoupling the static response in GPl-A results from the quasi-symmetric elastic modulus profile along the thickness, which has shifted the neutral plane back to the middle-plane.
- Uncoupled FGM plates show zero mid-plane extension in bending response, and a linear variation of bending stress σ_x, which is a property that characterizes isotropic plates.

- P-O distribution is the most advantageous porosity distribution for FGM plates rigidity. P-V showed comparable results to GPl-A in uncoupling the static response.
- GPl-O and P-X are the most unfavourable distributions of GPls and porosities, respectively.
- The vibration frequencies, bending response, and critical buckling loads of GPls-reinforced metal-ceramic FGM plates lie in an intermediate place between those of GPls-reinforced isotropic plates.
- Bifurcation buckling does not take place when GPls are asymmetrically distributed through the thickness of symmetric FGM plates.
- Square FGM plates always buckle at the first mode with a single hump. But for rectangular plates, the buckling mode changes with the aspect ratio a/h. This behaviour is invariant with the composition of the FGM.
- The relative effect of GPls on the mechanical response is maximal at the first added amounts.

Potential applications of the present FGM model

The explored metal-ceramic FGM plate model has promising aerospace engineering applications. The most suitable application the amelioration of FGM thermal protection systems in space vehicles, which occur in engines combustion compartments, and in outer protection shields that face the extreme environments in atmospheric re-entry. FGMs were already proposed for this usage, where ceramic serves as a heat insulation material, while metal gives structural integrity and ductility. The novelty here is that GPls are added to enhance structural stiffness, to dampen vibration amplitudes, and to reduce static deformations. This nano-additive may also aid to reduce total structural weight, as it has less mass density than most metals and ceramics.

On the other hand, porosities are incorporated in balanced amounts to reduce weight and to cut off material consumption. Material voids will also help to increase thermal resistance, as air or vacuum –which may compose pores– are very good insulators.

Another interesting application to be considered is that of combustion chambers walls in automotive vehicles, which can attain very high thermal stresses. Incorporating GPls and porosities in studied amounts can improve the rigidity and thermal resistance of these components.

Future recommendations

We have presented this work on porous GPls-reinforced FGM plates with the aim of giving valuable contribution to the field of composite materials, and particularly FGMs. This analysis can be further enriched by considering these additional parameters:

- We recommend to apply the present method to different boundary conditions other than simple supports. This can be done by using the analytical method of Levy for certain support combinations, or by the Ritz or Galerkin methods for all types of supports. Tackling this problem using simulation methods like the FEM is also encouraged.
- We also suggest the extension of this analysis to shells structures, which feature special geometric complexity that can reveal more interesting results.
- A useful extension of this work would be the combination of piezoelectric actuator layers with the studied FGM plate model. Piezoelectric devices are very interesting for the domain of structural dynamics as they have the potential of damping vibration.
- As for the experimental part, we suggest the realization of this FGM model using an appropriate experimental technique. We suggest the sophisticated technique of 3D printing that we described well in the first chapter, or by the long-standing method of powder-metallurgy.
- Finally, in order to fully characterize the combined microstructural interactions between the base FGM, GPls, and porosities, we advise other researchers to include 3D molecular dynamics modelling in the analysis. This approach may be very expensive in terms of computational resources and time, but it will predict the mechanical behaviour of porous GPls-reinforced FGM plates in a very realistic way.

Bibliography

[1] M. Abualnour, M. S. A. Houari, A. Tounsi, E. A. A. Bedia, and S. R. Mahmoud, 'A novel quasi-3D trigonometric plate theory for free vibration analysis of advanced composite plates', *Composite Structures*, vol. 184, pp. 688–697, Jan. 2018, doi: 10.1016/j.compstruct.2017.10.047.

[2] M. Sheikholeslami, A. Adamian, and K. H. Safari, 'Nonlinear vibrations of doubly curved micropanels reinforced by graphene nanoplates in length direction under non-uniform thermal loading', *Journal of Vibration and Control*, p. 1 077 546 323 1 194 266, Aug. 2023, doi: 10.1177/1 077 546 323 1 194 266.

[3] B. W. Abuteir and D. Boutagouga, 'Free-vibration response of functionally graded porous shell structures in thermal environments with temperature-dependent material properties', *Acta Mechanica*, vol. 233, no. 11, pp. 4877–4901, Oct. 2022, doi: 10.1007/s00 707-022-03 351-y.

[4] A. M. Zenkour and M. H. Aljadani, 'Thermo-electrical buckling response of actuated functionally graded piezoelectric nanoscale plates', *Results in Physics*, vol. 13, p. 102 192, Jun. 2019, doi: 10.1016/j.rinp.2019.102192.

[5] C. Petit, L. Montanaro, and P. Palmero, 'Functionally graded ceramics for biomedical application: Concept, manufacturing, and properties', *International Journal of Applied Ceramic Technology*, vol. 15, no. 4, pp. 820–840, 2018, doi: 10.1111/ijac.12878.

[6] A. Hassaine and A. Mahi, 'Effects of graphene-platelets reinforcement on the free vibration, bending, and buckling of porous functionally-graded metal-ceramic plates', *Journal of Composite Materials*, p. 0 021 998 323 1 196 276, Aug. 2023, doi: 10.1177/0 021 998 323 1 196 276.

[7] Hassaine Abdellah and Amale Mahi, 'Improving Photovoltaic Technology by Nanomaterials: a Brief Review', presented at the The First International Conference on Advanced Renewable Energy Systems, BouIsmail Tipaza, Dec. 2022.

[8] A. Hassaine and A. Mahi, 'Improving photovoltaic technology by nanomaterials: a brief review', *Journal of Renewable Energies*, vol. 1, no. 1, pp. 83–92, 2023, doi: https://doi.org/10.54966/jreen.v1i1.1101.

[9] Hassaine Abdellah and Amale Mahi, 'Analyzing the accuracy of various quasi-three-dimensional higher-order plate theories in predicting the deflection of FGM plates', presented at the Second International Conference on Mathematics and Applications (ICMA'2023), University of Blida 1, Blida, Sep. 2023.

[10] Amale Mahi and Abdellah Hassaine, 'Analytical solution for free vibration analysis of graphene-reinforced porous FGM beams under different boundary conditions', presented at the ICCESEN-2023: 10th International Conference on Computational and Experimental Science and Engineering, Antalya, Turkey, Oct. 2023.

[11] Amale Mahi and Abdellah Hassaine, 'An accurate analytical approach for the free vibration analysis of CNT-reinforced porous composite beams under different boundary conditions', presented at the ICCESEN-2023: 10th International Conference on Computational and Experimental Science and Engineering, Antalya, Turkey, Oct. 2023.

[12] N. Bertolino *et al.*, 'Self-propagating high-temperature synthesis of functionally graded materials as thermal protection systems for high-temperature applications', in *Journal of Materials Research*, Springer, 2003, pp. 448–455. [Online]. Available: https://link.springer.com/article/10.1557/JMR.2003.0057

[13] B. Saleh *et al.*, '30 Years of functionally graded materials: An overview of manufacturing methods, Applications and Future Challenges', *Composites Part B: Engineering*, vol. 201, p. 108 376, Nov. 2020, doi: 10.1016/j.compositesb.2020.108376.

[14] A. Razaq, F. Bibi, X. Zheng, R. Papadakis, S. H. M. Jafri, and H. Li, 'Review on Graphene-, Graphene Oxide-, Reduced Graphene Oxide-Based Flexible Composites: From Fabrication to Applications', *Materials*, vol. 15, no. 3, Art. no. 3, Jan. 2022, doi: 10.3390/ma15 031 012.

[15] T. D. Ngo, A. Kashani, G. Imbalzano, K. T. Q. Nguyen, and D. Hui, 'Additive manufacturing (3D printing): A review of materials, methods, applications and challenges', *Composites Part B: Engineering*, vol. 143, pp. 172–196, Jun. 2018, doi: 10.1016/j.compositesb.2018.02.012.

[16] X. Tian, Z. Zhao, H. Wang, X. Liu, and X. Song, 'Progresses on the additive manufacturing of functionally graded metallic materials', *Journal of Alloys and Compounds*, vol. 960, p. 170 687, Oct. 2023, doi: 10.1016/j.jallcom.2023.170687.

[17] J. P. Kelly, J. W. Elmer, F. J. Ryerson, J. R. I. Lee, and J. J. Haslam, 'Directed energy deposition additive manufacturing of functionally graded Al-W composites', *Additive Manufacturing*, vol. 39, p. 101 845, Mar. 2021, doi: 10.1016/j.addma.2021.101845.

[18] T. Fujii, K. Tohgo, H. Isono, and Y. Shimamura, 'Fabrication of a PSZ-Ti functionally graded material by spark plasma sintering and its fracture toughness', *Materials Science and Engineering: A*, vol. 682, pp. 656–663, Jan. 2017, doi: 10.1016/j.msea.2016.11.091.

[19] J. Matějíček, R. Mušálek, and J. Veverka, 'Materials and processing factors influencing stress evolution and mechanical properties of plasma sprayed coatings', *Surface and Coatings Technology*, vol. 371, pp. 3–13, Aug. 2019, doi: 10.1016/j.surfcoat.2019.01.105.

[20] Y. Su, B. Chen, C. Tan, X. Song, and J. Feng, 'Influence of composition gradient variation on the microstructure and mechanical properties of 316 L/Inconel718 functionally graded material fabricated by laser additive manufacturing', *Journal of Materials Processing Technology*, vol. 283, p. 116 702, Sep. 2020, doi: 10.1016/j.jmatprotec.2020.116702.

[21] T. Nakamura, T. Wang, and S. Sampath, 'Determination of properties of graded materials by inverse analysis and instrumented indentation', *Acta*

Materialia, vol. 48, no. 17, pp. 4293–4306, Nov. 2000, doi: 10.1016/S1359-6454(00)00217-2.

[22] B. Koohbor, S. Mallon, A. Kidane, A. Anand, and V. Parameswaran, 'Through Thickness Elastic Profile Determination of Functionally Graded Materials', *Exp Mech*, vol. 55, no. 8, pp. 1427–1440, Oct. 2015, doi: 10.1007/s11340-015-0043-z.

[23] N. Noda, 'Thermal stresses in functionally graded materials', *Journal of Thermal Stresses*, vol. 22, no. 4–5, pp. 477–512, Jun. 1999, doi: 10.1080/01495739928041.

[24] J. R. Cho and J. T. Oden, 'Functionally graded material: a parametric study on thermal-stress characteristics using the Crank–Nicolson–Galerkin scheme', *Computer Methods in Applied Mechanics and Engineering*, vol. 188, no. 1, pp. 17–38, Jul. 2000, doi: 10.1016/S0045-7825(99)00289-3.

[25] X. Zhao, Y. Y. Lee, and K. M. Liew, 'Thermoelastic and vibration analysis of functionally graded cylindrical shells', *International Journal of Mechanical Sciences*, vol. 51, no. 9–10, pp. 694–707, 2009, doi: 10.1016/j.ijmecsci.2009.08.001.

[26] S. Trabelsi, A. Frikha, S. Zghal, and F. Dammak, 'Thermal post-buckling analysis of functionally graded material structures using a modified FSDT', *International Journal of Mechanical Sciences*, vol. 144, pp. 74–89, Aug. 2018, doi: 10.1016/j.ijmecsci.2018.05.033.

[27] B. Yildirim, S. Dag, and F. Erdogan, 'Three dimensional fracture analysis of FGM coatings under thermomechanical loading', *Int J Fract*, vol. 132, no. 4, pp. 371–397, Apr. 2005, doi: 10.1007/s10704-005-2527-9.

[28] Z. Mohammadzaki Goudarzi, Z. Valefi, and P. Zamani, 'Effect of functionally graded structure design on durability and thermal insulation capacity of plasma-sprayed thick thermal barrier coating', *Ceramics International*, vol. 47, no. 24, pp. 34361–34379, Dec. 2021, doi: 10.1016/j.ceramint.2021.08.349.

[29] B. Saeedi, A. Sabour, and A. M. Khoddami, 'Study of microstructure and thermal shock behavior of two types of thermal barrier coatings', *Materials and Corrosion*, vol. 60, no. 9, pp. 695–703, 2009, doi: 10.1002/maco.200905111.

[30] H. Shi, P. Zhou, J. Li, C. Liu, and L. Wang, 'Functional Gradient Metallic Biomaterials: Techniques, Current Scenery, and Future Prospects in the Biomedical Field', *Front Bioeng Biotechnol*, vol. 8, p. 616845, Jan. 2021, doi: 10.3389/fbioe.2020.616845.

[31] J. Yang and H.-S. Shen, 'VIBRATION CHARACTERISTICS AND TRANSIENT RESPONSE OF SHEAR-DEFORMABLE FUNCTIONALLY GRADED PLATES IN THERMAL ENVIRONMENTS', *Journal of Sound and Vibration*, vol. 255, no. 3, pp. 579–602, Aug. 2002, doi: 10.1006/jsvi.2001.4161.

[32] X.-L. Huang and H.-S. Shen, 'Nonlinear vibration and dynamic response of functionally graded plates in thermal environments', *International Journal of Solids and Structures*, vol. 41, no. 9, pp. 2403–2427, May 2004, doi: 10.1016/j.ijsolstr.2003.11.012.

[33] A. M. Zenkour, 'A comprehensive analysis of functionally graded sandwich plates: Part 1—Deflection and stresses', *International Journal of Solids and*

Structures, vol. 42, no. 18, pp. 5224–5242, Sep. 2005, doi: 10.1016/j.ijsolstr.2005.02.015.

[34] Q. Li, V. P. Iu, and K. P. Kou, 'Three-dimensional vibration analysis of functionally graded material plates in thermal environment', *Journal of Sound and Vibration*, vol. 324, no. 3–5, pp. 733–750, 2009, doi: 10.1016/j.jsv.2009.02.036.

[35] L. F. Qian, R. C. Batra, and L. M. Chen, 'Static and dynamic deformations of thick functionally graded elastic plates by using higher-order shear and normal deformable plate theory and meshless local Petrov–Galerkin method', *Composites Part B: Engineering*, vol. 35, no. 6, pp. 685–697, Sep. 2004, doi: 10.1016/j.compositesb.2004.02.004.

[36] S.-C. Han, W.-T. Park, and W.-Y. Jung, 'A four-variable refined plate theory for dynamic stability analysis of S-FGM plates based on physical neutral surface', *Composite Structures*, vol. 131, pp. 1081–1089, Nov. 2015, doi: 10.1016/j.compstruct.2015.06.025.

[37] W. Huang, K. Xue, and Q. Li, 'Three-Dimensional Solution for the Vibration Analysis of Functionally Graded Rectangular Plate with/without Cutouts Subject to General Boundary Conditions', *Materials*, vol. 14, no. 22, Art. no. 22, Jan. 2021, doi: 10.3390/ma14 227 088.

[38] A. Lahdiri and M. Kadri, 'Free vibration behaviour of multi-directional functionally graded imperfect plates using 3D isogeometric approach', *Earthquakes and Structures*, vol. 22, no. 5, pp. 527–538, 2022, doi: 10.12989/eas.2022.22.5.527.

[39] T. P. Nguyen, T. Nguyen-Thoi, D. K. Tran, D. T. Ho, and H. N. Vu, 'Nonlinear vibration of full-filled fluid corrugated sandwich functionally graded cylindrical shells', *Journal of Vibration and Control*, vol. 27, no. 9–10, pp. 1020–1035, May 2021, doi: 10.1177/1 077 546 320 936 537.

[40] Ç. Bolat, C. Bekar, and A. Göksenli, 'Mechanical and Physical Characteristics of Bubble Alumina Reinforced Aluminum Syntactic Foams Made Through Recyclable Pressure Infiltration Technique', *Gazi University Journal of Science*, vol. 35, no. 1, Art. no. 1, Mar. 2022, doi: 10.35378/gujs.855321.

[41] K. Kim, D. Kim, S. Ryu, S. Yoon, and H. Park, 'Porous mullite/alumina-layered composites with a graded porosity fabricated by camphene-based freeze casting', *Journal of Composite Materials*, vol. 54, no. 12, pp. 1527–1534, May 2020, doi: 10.1177/0 021 998 316 636 460.

[42] Bin Liu, Huihui Chen, and Wei Cao, 'A novel method for tailoring elasticity distributions of functionally graded porous materials', *International Journal of Mechanical Sciences*, vol. 157–158, pp. 457–470, Jul. 2019, doi: 10.1016/j.ijmecsci.2019.05.002.

[43] E. K. Baghtifouni and A. H. Monazzah, 'Longitudinal graded porous titanium fabricated by spark plasma sintering: Design of layers, direction of crack path', *Journal of Manufacturing Processes*, vol. 81, pp. 738–747, Sep. 2022, doi: 10.1016/j.jmapro.2022.07.036.

[44] A. Díaz and S. Hampshire, 'Characterisation of porous silicon nitride materials produced with starch', *Journal of the European Ceramic Society*, vol. 24, no. 2, pp. 413–419, Jan. 2004, doi: 10.1016/S0955-2219(03)00 212-7.
[45] W. Pabst, E. Gregorová, and G. Tichá, 'Elasticity of porous ceramics—A critical study of modulus–porosity relations', *Journal of the European Ceramic Society*, vol. 26, no. 7, pp. 1085–1097, Jan. 2006, doi: 10.1016/j.jeurceramsoc.2005.01.041.
[46] R. Vemoori, S. Bejugama, and A. K. Khanra, 'Fabrication and characterization of alumina and zirconia-toughened alumina porous structures', *Ceramics International*, vol. 49, no. 13, pp. 21 708–21 715, Jul. 2023, doi: 10.1016/j.ceramint.2023.03.310.
[47] Y. Tang, C. Wu, and K. Zhao, 'Fabrication of lamellar porous alumina with graded structures by combining centrifugal and directional freeze casting', *Ceramics International*, vol. 44, no. 5, pp. 5794–5798, Apr. 2018, doi: 10.1016/j.ceramint.2017.12.120.
[48] M. Coffigniez, L. Gremillard, and X. Boulnat, 'Sinter-Based Additive Manufacturing of Graded Porous Titanium Scaffolds by Multi-Inks 3D Extrusion', *Advanced Engineering Materials*, vol. 25, no. 4, p. 2 201 159, 2023, doi: 10.1002/adem.202201 159.
[49] L. Bai *et al.*, 'Quasi-Static compressive responses and fatigue behaviour of Ti-6Al-4V graded lattice structures fabricated by laser powder bed fusion', *Materials & Design*, vol. 210, p. 110 110, Nov. 2021, doi: 10.1016/j.matdes.2021.110110.
[50] L. Yang *et al.*, 'Insights into unit cell size effect on mechanical responses and energy absorption capability of titanium graded porous structures manufactured by laser powder bed fusion', *Journal of the Mechanical Behavior of Biomedical Materials*, vol. 109, p. 103 843, Sep. 2020, doi: 10.1016/j.jmbbm.2020.103843.
[51] K. Cao *et al.*, 'Elastic straining of free-standing monolayer graphene', *Nat Commun*, vol. 11, no. 1, Art. no. 1, Jan. 2020, doi: 10.1038/s41 467-019-14 130-0.
[52] M. Song, S. Kitipornchai, and J. Yang, 'Free and forced vibrations of functionally graded polymer composite plates reinforced with graphene nanoplatelets', *Composite Structures*, vol. 159, pp. 579–588, Jan. 2017, doi: 10.1016/j.compstruct.2016.09.070.
[53] H. Wu, J. Yang, and S. Kitipornchai, 'Parametric instability of thermo-mechanically loaded functionally graded graphene reinforced nanocomposite plates', *International Journal of Mechanical Sciences*, vol. 135, pp. 431–440, 2018, doi: 10.1016/j.ijmecsci.2017.11.039.
[54] E. García-Macías, L. Rodríguez-Tembleque, and A. Sáez, 'Bending and free vibration analysis of functionally graded graphene vs. carbon nanotube reinforced composite plates', *Composite Structures*, vol. 186, pp. 123–138, 2018, doi: 10.1016/j.compstruct.2017.11.076.
[55] J. Yang, D. Chen, and S. Kitipornchai, 'Buckling and free vibration analyses of functionally graded graphene reinforced porous nanocomposite plates

based on Chebyshev-Ritz method', *Composite Structures*, vol. 193, pp. 281–294, Jun. 2018, doi: 10.1016/j.compstruct.2018.03.090.

[56] J. Zhao, K. Choe, F. Xie, A. Wang, C. Shuai, and Q. Wang, 'Three-dimensional exact solution for vibration analysis of thick functionally graded porous (FGP) rectangular plates with arbitrary boundary conditions', *Composites Part B: Engineering*, vol. 155, pp. 369–381, Dec. 2018, doi: 10.1016/j.compositesb.2018.09.001.

[57] F. Pashmforoush, 'Statistical analysis on free vibration behavior of functionally graded nanocomposite plates reinforced by graphene platelets', *Composite Structures*, vol. 213, pp. 14–24, Apr. 2019, doi: 10.1016/j.compstruct.2019.01.066.

[58] C. H. Thai and P. Phung-Van, 'A meshfree approach using naturally stabilized nodal integration for multilayer FG GPLRC complicated plate structures', *Engineering Analysis with Boundary Elements*, vol. 117, pp. 346–358, Aug. 2020, doi: 10.1016/j.enganabound.2020.04.001.

[59] Q. H. Nguyen, L. B. Nguyen, H. B. Nguyen, and H. Nguyen-Xuan, 'A three-variable high order shear deformation theory for isogeometric free vibration, buckling and instability analysis of FG porous plates reinforced by graphene platelets', *Composite Structures*, vol. 245, p. 112 321, Aug. 2020, doi: 10.1016/j.compstruct.2020.112321.

[60] J. Zheng, C. Zhang, F. Musharavati, A. Khan, T. A. Sebaey, and A. Eyvazian, 'Forced vibration characteristics of embedded graphene oxide powder reinforced metal foam nanocomposite plate in thermal environment', *Case Studies in Thermal Engineering*, vol. 27, p. 101 167, Oct. 2021, doi: 10.1016/j.csite.2021.101167.

[61] V. Nguyen Van Do and C.-H. Lee, 'Isogeometric analysis for buckling and postbuckling of graphene platelet reinforced composite plates in thermal environments', *Engineering Structures*, vol. 244, p. 112 746, Oct. 2021, doi: 10.1016/j.engstruct.2021.112746.

[62] E. I. Salama, S. S. Morad, and A. M. K. Esawi, 'Fabrication and mechanical properties of aluminum-carbon nanotube functionally-graded cylinders', *Materialia*, vol. 7, p. 100 351, Sep. 2019, doi: 10.1016/j.mtla.2019.100351.

[63] A. A. Daikh, M. S. A. Houari, M. O. Belarbi, S. A. Mohamed, and M. A. Eltaher, 'Static and dynamic stability responses of multilayer functionally graded carbon nanotubes reinforced composite nanoplates via quasi 3D nonlocal strain gradient theory', *Defence Technology*, vol. 18, no. 10, pp. 1778–1809, Oct. 2022, doi: 10.1016/j.dt.2021.09.011.

[64] M. Alinia, S. Saber-Samandari, and S. A. Sadough Vanini, 'On the mechanical properties and vibrational characteristics of the nanoparticle-reinforced composite cylindrical panels in the acidic environment: Numerical and experimental investigation', *Journal of Reinforced Plastics and Composites*, p. 0 731 684 423 1 197 256, Aug. 2023, doi: 10.1177/0 731 684 423 1 197 256.

[65] S. K. Sahu and P. S. R. Sreekanth, 'Experimental investigation of in-plane compressive and damping behavior anisotropic graded honeycomb

structure', *Arab J Sci Eng*, vol. 47, no. 12, pp. 15 741–15 753, Dec. 2022, doi: 10.1007/s13 369-022-06 771-z.

[66] D. Mahmoud and M. A. Elbestawi, 'Lattice Structures and Functionally Graded Materials Applications in Additive Manufacturing of Orthopedic Implants: A Review', *Journal of Manufacturing and Materials Processing*, vol. 1, no. 2, Art. no. 2, Dec. 2017, doi: 10.3390/jmmp1 020 013.

[67] W. Alhazmi *et al.*, 'Mechanical and Tribological Behavior of Functionally Graded Unidirectional Glass Fiber-Reinforced Epoxy Composites', *Polymers*, vol. 14, no. 10, Art. no. 10, Jan. 2022, doi: 10.3390/polym14 102 057.

[68] J. Kupski and S. Teixeira de Freitas, 'Design of adhesively bonded lap joints with laminated CFRP adherends: Review, challenges and new opportunities for aerospace structures', *Composite Structures*, vol. 268, p. 113 923, Jul. 2021, doi: 10.1016/j.compstruct.2021.113923.

[69] W. Voigt, 'Ueber die Beziehung zwischen den beiden Elasticitätsconstanten isotroper Körper (On the relationship between the two elasticity constants of isotropic bodies)', *Annalen der Physik*, vol. 274, no. 12, pp. 573–587, 1889, doi: https://doi.org/10.1002/andp.18892 741 206.

[70] S. S. Vel and R. C. Batra, 'Three-dimensional exact solution for the vibration of functionally graded rectangular plates', *Journal of Sound and Vibration*, vol. 272, no. 3–5, pp. 703–730, 2004, doi: 10.1016/S0022-460X(03)00 412-7.

[71] A. J. M. Ferreira, R. C. Batra, C. M. C. Roque, L. F. Qian, and P. A. L. S. Martins, 'Static analysis of functionally graded plates using third-order shear deformation theory and a meshless method', *Composite Structures*, vol. 69, no. 4, pp. 449–457, Aug. 2005, doi: 10.1016/j.compstruct.2004.08.003.

[72] A. H. Akbarzadeh, A. Abedini, and Z. T. Chen, 'Effect of micromechanical models on structural responses of functionally graded plates', *Composite Structures*, vol. 119, pp. 598–609, Jan. 2015, doi: 10.1016/j.compstruct.2014.09.031.

[73] A. M. Zenkour, 'Benchmark trigonometric and 3-D elasticity solutions for an exponentially graded thick rectangular plate', *Arch Appl Mech*, vol. 77, no. 4, pp. 197–214, Apr. 2007, doi: 10.1007/s00 419-006-0084-y.

[74] A. Fekrar, M. S. A. Houari, A. Tounsi, and S. R. Mahmoud, 'A new five-unknown refined theory based on neutral surface position for bending analysis of exponential graded plates', *Meccanica*, vol. 49, no. 4, pp. 795–810, Apr. 2014, doi: 10.1007/s11 012-013-9827-3.

[75] A. F. Mota, M. A. R. Loja, J. I. Barbosa, and J. A. Rodrigues, 'Porous Functionally Graded Plates: An Assessment of the Influence of Shear Correction Factor on Static Behavior', *Mathematical and Computational Applications*, vol. 25, no. 2, Art. no. 2, Jun. 2020, doi: 10.3390/mca25 020 025.

[76] P. V. Vinh, N. V. Chinh, and A. Tounsi, 'Static bending and buckling analysis of bi-directional functionally graded porous plates using an improved first-order shear deformation theory and FEM', *European Journal of Mechanics - A/Solids*, vol. 96, p. 104 743, 2022, doi: https://doi.org/10.1016/j.euromechsol.2022.104743.

[77] P. A. Demirhan and V. Taskin, 'Bending and free vibration analysis of Levy-type porous functionally graded plate using state space approach',

Composites Part B: Engineering, vol. 160, pp. 661–676, Mar. 2019, doi: 10.1016/j.compositesb.2018.12.020.

[78] A. Gupta and M. Talha, 'An assessment of a non-polynomial based higher order shear and normal deformation theory for vibration response of gradient plates with initial geometric imperfections', *Composites Part B: Engineering*, vol. 107, pp. 141–161, Dec. 2016, doi: 10.1016/j.compositesb.2016.09.071.

[79] A. M. Zenkour and M. H. Aljadani, 'Buckling Response of Functionally Graded Porous Plates Due to a Quasi-3D Refined Theory', *Mathematics*, vol. 10, no. 4, Art. no. 4, Jan. 2022, doi: 10.3390/math10040565.

[80] W. Pabst and E. Gregorová, 'Critical Assessment 18: elastic and thermal properties of porous materials – rigorous bounds and cross-property relations', *Materials Science and Technology*, vol. 31, no. 15, pp. 1801–1808, Dec. 2015, doi: 10.1080/02670836.2015.1114697.

[81] F. Ternero, L. G. Rosa, P. Urban, J. M. Montes, and F. G. Cuevas, 'Influence of the Total Porosity on the Properties of Sintered Materials—A Review', *Metals*, vol. 11, no. 5, p. 730, Apr. 2021, doi: 10.3390/met11050730.

[82] S. K. Jalali, M. J. Beigrezaee, and N. M. Pugno, 'Reporting a misunderstanding in relating the Young's modulus to functionally graded porosity', *Composite Structures*, vol. 281, p. 115007, 2022, doi: https://doi.org/10.1016/j.compstruct.2021.115007.

[83] T. Uhlířová and W. Pabst, 'Poisson's ratio of porous and cellular materials with randomly distributed isometric pores or cells', *J Am Ceram Soc*, vol. 103, no. 12, pp. 6961–6977, Dec. 2020, doi: 10.1111/jace.17139.

[84] M. Shen *et al.*, 'Mechanical properties of 3D printed ceramic cellular materials with triply periodic minimal surface architectures', *Journal of the European Ceramic Society*, vol. 41, no. 2, pp. 1481–1489, 2021, doi: https://doi.org/10.1016/j.jeurceramsoc.2020.09.062.

[85] W. Pabst, T. Uhlířová, E. Gregorová, and A. Wiegmann, 'Young's modulus and thermal conductivity of closed-cell, open-cell and inverse ceramic foams – model-based predictions, cross-property predictions and numerical calculations', *Journal of the European Ceramic Society*, vol. 38, no. 6, pp. 2570–2578, Jun. 2018, doi: 10.1016/j.jeurceramsoc.2018.01.019.

[86] M. Quaresimin, M. Salviato, and M. Zappalorto, 'Strategies for the assessment of nanocomposite mechanical properties', *Composites Part B: Engineering*, vol. 43, no. 5, pp. 2290–2297, Jul. 2012, doi: 10.1016/j.compositesb.2011.12.012.

[87] J. C. H. Affdl and J. L. Kardos, 'The Halpin-Tsai equations: A review', *Polymer Engineering & Science*, vol. 16, no. 5, pp. 344–352, 1976, doi: 10.1002/pen.760160512.

[88] D. Punera, 'The effect of agglomeration and slightly weakened CNT–matrix interface on free vibration response of cylindrical nanocomposites', *Acta Mech*, vol. 232, no. 6, pp. 2455–2477, Jun. 2021, doi: 10.1007/s00707-020-02933-y.

[89] E. Sadeghpour, Y. Guo, D. Chua, and V. P. W. Shim, 'A modified Mori–Tanaka approach incorporating filler-matrix interface failure to model

graphene/polymer nanocomposites', *International Journal of Mechanical Sciences*, vol. 180, p. 105 699, Aug. 2020, doi: 10.1016/j.ijmecsci.2020.105699.
[90] R. Rahman and A. Haque, 'Molecular modeling of crosslinked graphene–epoxy nanocomposites for characterization of elastic constants and interfacial properties', *Composites Part B: Engineering*, vol. 54, pp. 353–364, Nov. 2013, doi: 10.1016/j.compositesb.2013.05.034.
[91] A. E. H. Love and G. H. Darwin, 'XVI. The small free vibrations and deformation of a thin elastic shell', *Philosophical Transactions of the Royal Society of London. (A.)*, vol. 179, pp. 491–546, Jan. 1997, doi: 10.1098/rsta.1888.0016.
[92] E. Reissner, 'On the Theory of Bending of Elastic Plates', *Journal of Mathematics and Physics*, vol. 23, no. 1–4, pp. 184–191, Apr. 1944, doi: 10.1002/sapm1 944 231 184.
[93] E. Reissner, 'On bending of elastic plates', *Quarterly of Applied Mathematics*, vol. 5, no. 1, pp. 55–68, 1947.
[94] R. D. Mindlin, 'Influence of Rotatory Inertia and Shear on Flexural Motions of Isotropic, Elastic Plates', *Journal of Applied Mechanics*, vol. 18, no. 1, pp. 31–38, Mar. 1951, doi: 10.1115/1.4010217.
[95] S. P. Timoshenko, 'LXVI. On the correction for shear of the differential equation for transverse vibrations of prismatic bars', *The London, Edinburgh, and Dublin Philosophical Magazine and Journal of Science*, vol. 41, no. 245, pp. 744–746, May 1921, doi: 10.1080/1 478 644 210 8 636 264.
[96] V. Birman and C. W. Bert, 'On the Choice of Shear Correction Factor in Sandwich Structures', *Jnl of Sandwich Structures & Materials*, vol. 4, no. 1, pp. 83–95, Jan. 2002, doi: 10.1177/1 099 636 202 004 001 180.
[97] C. M. Wang, G. T. Lim, J. N. Reddy, and K. H. Lee, 'Relationships between bending solutions of Reissner and Mindlin plate theories', *Engineering Structures*, vol. 23, no. 7, pp. 838–849, Jul. 2001, doi: 10.1016/S0141-0296(00)00 092-4.
[98] R. P. Shimpi, H. G. Patel, and H. Arya, 'New First-Order Shear Deformation Plate Theories', *Journal of Applied Mechanics*, vol. 74, no. 3, pp. 523–533, May 2006, doi: 10.1115/1.2423036.
[99] A. S. Rezaei, A. R. Saidi, M. Abrishamdari, and M. H. P. Mohammadi, 'Natural frequencies of functionally graded plates with porosities via a simple four variable plate theory: An analytical approach', *Thin-Walled Structures*, vol. 120, pp. 366–377, Nov. 2017, doi: 10.1016/j.tws.2017.08.003.
[100] H. Bellifa, K. H. Benrahou, L. Hadji, M. S. A. Houari, and A. Tounsi, 'Bending and free vibration analysis of functionally graded plates using a simple shear deformation theory and the concept the neutral surface position', *J Braz. Soc. Mech. Sci. Eng.*, vol. 38, no. 1, pp. 265–275, Jan. 2016, doi: 10.1007/s40 430-015-0354-0.
[101] L. F. Greimann and P. P. Lynn, 'Finite element analysis of plate bending with transverse shear deformation', *Nuclear Engineering and Design*, vol. 14, no. 2, pp. 223–230, Dec. 1970, doi: 10.1016/0029-5493(70)90 101-9.
[102] J. N. Reddy and C. D. Chin, 'THERMOMECHANICAL ANALYSIS OF FUNCTIONALLY GRADED CYLINDERS AND PLATES', *Journal of Thermal*

Stresses, vol. 21, no. 6, pp. 593–626, Sep. 1998, doi: 10.1080/0 149 573 980 8 956 165.

[103] L. Della Croce and P. Venini, 'Finite elements for functionally graded Reissner–Mindlin plates', *Computer Methods in Applied Mechanics and Engineering*, vol. 193, no. 9, pp. 705–725, Mar. 2004, doi: 10.1016/j.cma.2003.09.014.

[104] H. Nguyen-Xuan, T. Rabczuk, S. Bordas, and J. F. Debongnie, 'A smoothed finite element method for plate analysis', *Computer Methods in Applied Mechanics and Engineering*, vol. 197, no. 13, pp. 1184–1203, Feb. 2008, doi: 10.1016/j.cma.2007.10.008.

[105] G. Wei, P. Lardeur, and F. Druesne, 'Solid-shell approach based on first-order or higher-order plate and shell theories for the finite element analysis of thin to very thick structures', *European Journal of Mechanics - A/Solids*, vol. 94, p. 104 591, Jul. 2022, doi: 10.1016/j.euromechsol.2022.104591.

[106] A. J. M. Ferreira, R. C. Batra, C. M. C. Roque, L. F. Qian, and R. M. N. Jorge, 'Natural frequencies of functionally graded plates by a meshless method', *Composite Structures*, vol. 75, no. 1, pp. 593–600, Sep. 2006, doi: 10.1016/j.compstruct.2006.04.018.

[107] P. Zhu and K. M. Liew, 'Free vibration analysis of moderately thick functionally graded plates by local Kriging meshless method', *Composite Structures*, vol. 93, no. 11, pp. 2925–2944, Oct. 2011, doi: 10.1016/j.compstruct.2011.05.011.

[108] S. S. Chen, C. J. Xu, G. S. Tong, and X. Wei, 'Free vibration of moderately thick functionally graded plates by a meshless local natural neighbor interpolation method', *Engineering Analysis with Boundary Elements*, vol. 61, pp. 114–126, 2015, doi: 10.1016/j.enganabound.2015.07.008.

[109] M. Malik and C. W. Bert, 'Differential Quadrature Analysis of Free Vibration of Symmetric Cross-Ply Laminates with Shear Deformation and Rotatory Inertia', *Shock and Vibration*, vol. 2, no. 4, pp. 321–338, Jan. 1995, doi: 10.3233/SAV-1995-2406.

[110] K. M. Liew, Y. Q. Huang, and J. N. Reddy, 'Vibration analysis of symmetrically laminated plates based on FSDT using the moving least squares differential quadrature method', *Computer Methods in Applied Mechanics and Engineering*, vol. 192, no. 19, pp. 2203–2222, 2003, doi: 10.1016/S0045-7825(03)00 238-X.

[111] S. A. Mohamed, N. Mohamed, and M. A. Eltaher, 'Bending, buckling and linear vibration of bio-inspired composite plates', *Ocean Engineering*, vol. 259, 2022, doi: 10.1016/j.oceaneng.2022.111851.

[112] Y. B. Zhao and G. W. Wei, 'DSC ANALYSIS OF RECTANGULAR PLATES WITH NON-UNIFORM BOUNDARY CONDITIONS', *Journal of Sound and Vibration*, vol. 255, no. 2, pp. 203–228, Aug. 2002, doi: 10.1006/jsvi.2001.4150.

[113] Ö. Civalek, 'Analysis of Thick Rectangular Plates with Symmetric Cross-ply Laminates Based on First-order Shear Deformation Theory', *Journal of Composite Materials*, vol. 42, no. 26, pp. 2853–2867, Dec. 2008, doi: 10.1177/0 021 998 308 096 952.

[114] Ö. Civalek, 'Free vibration of carbon nanotubes reinforced (CNTR) and functionally graded shells and plates based on FSDT via discrete singular convolution method', *Composites Part B: Engineering*, vol. 111, pp. 45–59, Feb. 2017, doi: 10.1016/j.compositesb.2016.11.030.
[115] J. L. Mantari and E. V. Granados, 'A refined FSDT for the static analysis of functionally graded sandwich plates', *Thin-Walled Structures*, vol. 90, pp. 150–158, May 2015, doi: 10.1016/j.tws.2015.01.015.
[116] J. L. Mantari and E. V. Granados, 'Dynamic analysis of functionally graded plates using a novel FSDT', *Composites Part B: Engineering*, vol. 75, pp. 148–155, Jun. 2015, doi: 10.1016/j.compositesb.2015.01.028.
[117] F. Z. Zaoui, D. Ouinas, and A. Tounsi, 'New 2D and quasi-3D shear deformation theories for free vibration of functionally graded plates on elastic foundations', *Composites Part B: Engineering*, vol. 159, pp. 231–247, Feb. 2019, doi: 10.1016/j.compositesb.2018.09.051.
[118] R. Kienzler and P. Schneider, 'Second-order linear plate theories: Partial differential equations, stress resultants and displacements', *International Journal of Solids and Structures*, vol. 115–116, pp. 14–26, Jun. 2017, doi: 10.1016/j.ijsolstr.2017.01.004.
[119] Y. M. Ghugal and R. P. Shimpi, 'A Review of Refined Shear Deformation Theories of Isotropic and Anisotropic Laminated Plates', *Journal of Reinforced Plastics and Composites*, vol. 21, no. 9, pp. 775–813, Jun. 2002, doi: 10.1177/0 731 684 021 28 988 481.
[120] A. Tati, 'A five unknowns high order shear deformation finite element model for functionally graded plates bending behavior analysis', *Journal of the Brazilian Society of Mechanical Sciences and Engineering*, vol. 43, no. 1, p. 45, Jan. 2021, doi: 10.1007/s40 430-020-02 736-1.
[121] K. Rohwer, 'Application of higher order theories to the bending analysis of layered composite plates', *International Journal of Solids and Structures*, vol. 29, no. 1, pp. 105–119, Jan. 1992, doi: 10.1016/0020-7683(92)90 099-F.
[122] Y. M. Ghugal and R. P. Shimpi, 'A Review of Refined Shear Deformation Theories for Isotropic and Anisotropic Laminated Beams', *Journal of Reinforced Plastics and Composites*, vol. 20, no. 3, pp. 255–272, Feb. 2001, doi: 10.1177/0 731 684 017 72 678 283.
[123] N. F. Hanna, 'Thick plate theories, with applications to vibration', Doctoral thesis, The Ohio State University, United States -- Ohio. Accessed: May 12, 2022. [Online]. Available: https://www.proquest.com/docview/303 861 348/abstract/83C963C723BE499DPQ/1
[124] E. Reissner, 'On transverse bending of plates, including the effect of transverse shear deformation', *International Journal of Solids and Structures*, vol. 11, no. 5, pp. 569–573, May 1975, doi: 10.1016/0020-7683(75)90 030-X.
[125] M. Levinson, 'An accurate, simple theory of the statics and dynamics of elastic plates', *Mechanics Research Communications*, vol. 7, no. 6, pp. 343–350, Jan. 1980, doi: 10.1016/0093-6413(80)90 049-X.
[126] M. V. V. Murthy, 'An improved transverse shear deformation theory for laminated antisotropic plates', 1981.

[127] J. N. Reddy, 'A Simple Higher-Order Theory for Laminated Composite Plates', *Journal of Applied Mechanics*, vol. 51, no. 4, pp. 745–752, Dec. 1984, doi: 10.1115/1.3167719.
[128] J.N. Reddy and N.D.Phan, 'Stability and vibration of isotropic, orthotropic and laminated plates according to a higher-order shear deformation theory', *Journal ofSound and Vibration*, vol. 98, no. 2, pp. 157–170, 1985, doi: 10.1016/0022-460X(85)90 383-9.
[129] G. Shi, 'A new simple third-order shear deformation theory of plates', *International Journal of Solids and Structures*, vol. 44, no. 13, pp. 4399–4417, Jun. 2007, doi: 10.1016/j.ijsolstr.2006.11.031.
[130] R. P. Shimpi, 'Refined Plate Theory and Its Variants', *AIAA Journal*, vol. 40, no. 1, pp. 137–146, Jan. 2002, doi: 10.2514/2.1622.
[131] R. P. Shimpi and H. G. Patel, 'Free vibrations of plate using two variable refined plate theory', *Journal of Sound and Vibration*, vol. 296, no. 4, pp. 979–999, Oct. 2006, doi: 10.1016/j.jsv.2006.03.030.
[132] R. P. Shimpi and H. G. Patel, 'A two variable refined plate theory for orthotropic plate analysis', *International Journal of Solids and Structures*, vol. 43, no. 22, pp. 6783–6799, Nov. 2006, doi: 10.1016/j.ijsolstr.2006.02.007.
[133] H.-T. Thai and D.-H. Choi, 'Improved refined plate theory accounting for effect of thickness stretching in functionally graded plates', *Composites Part B: Engineering*, vol. 56, pp. 705–716, Jan. 2014, doi: 10.1016/j.compositesb.2013.09.008.
[134] M. Levy, 'Mémoire sur la théorie des plaques élastiques planes', *Journal de Mathématiques Pures et Appliquées*, vol. 3, pp. 219–306, 1877, Accessed: Feb. 25, 2023. [Online]. Available: http://www.numdam.org/item/JMPA_1877_3_3__219_0/
[135] N. A. Kil'chevskiy, *Fundamentals of the analytical mechanics of shells*. National Aeronautics and Space Administration, 1963.
[136] M. Stein and D. C. Jegley, 'Effects of transverse shearing on cylindrical bending, vibration, and buckling of laminated plates', presented at the Structures, Structural Dynamics, and Materials Conference, Orlando, FL, Jan. 1985. Accessed: Feb. 25, 2023. [Online]. Available: https://ntrs.nasa.gov/citations/19 850 048 133
[137] M. Stein, 'Nonlinear theory for plates and shells including the effects of transverse shearing', *AIAA Journal*, vol. 24, no. 9, pp. 1537–1544, Sep. 1986, doi: 10.2514/3.9477.
[138] D. C. Jegley, 'An analytical study of the effects of transverse shear deformation and anisotropy on natural vibration frequencies of laminated cylinders', NAS 1.15:100 554, Jan. 1988. Accessed: Feb. 25, 2023. [Online]. Available: https://ntrs.nasa.gov/citations/19 880 008 355
[139] M. Touratier, 'An efficient standard plate theory', *International Journal of Engineering Science*, vol. 29, no. 8, pp. 901–916, Jan. 1991, doi: 10.1016/0020-7225(91)90 165-Y.
[140] A. M. Zenkour, 'Analytical solution for bending of cross-ply laminated plates under thermo-mechanical loading', *Composite Structures*, vol. 65, no. 3, pp. 367–379, Sep. 2004, doi: 10.1016/j.compstruct.2003.11.012.

[141] A. M. Zenkour, 'Generalized shear deformation theory for bending analysis of functionally graded plates', *Applied Mathematical Modelling*, vol. 30, no. 1, pp. 67–84, Jan. 2006, doi: 10.1016/j.apm.2005.03.009.
[142] A. M. Zenkour, 'Buckling of fiber-reinforced viscoelastic composite plates using various plate theories', *Journal of Engineering Mathematics*, vol. 50, no. 1, pp. 75–93, Sep. 2004, doi: 10.1023/B:ENGI.0000042123.94111.35.
[143] Y. S. Li and E. Pan, 'Static bending and free vibration of a functionally graded piezoelectric microplate based on the modified couple-stress theory', *International Journal of Engineering Science*, vol. 97, pp. 40–59, Dec. 2015, doi: 10.1016/j.ijengsci.2015.08.009.
[144] H.-T. Thai and T. P. Vo, 'A nonlocal sinusoidal shear deformation beam theory with application to bending, buckling, and vibration of nanobeams', *International Journal of Engineering Science*, vol. 54, pp. 58–66, May 2012, doi: 10.1016/j.ijengsci.2012.01.009.
[145] H.-T. Thai, T. P. Vo, T.-K. Nguyen, and J. Lee, 'A nonlocal sinusoidal plate model for micro/nanoscale plates', *Proceedings of the Institution of Mechanical Engineers, Part C: Journal of Mechanical Engineering Science*, vol. 228, no. 14, pp. 2652–2660, Oct. 2014, doi: 10.1177/0954406214521391.
[146] A. Tounsi, M. S. A. Houari, S. Benyoucef, and E. A. Adda Bedia, 'A refined trigonometric shear deformation theory for thermoelastic bending of functionally graded sandwich plates', *Aerospace Science and Technology*, vol. 24, no. 1, pp. 209–220, Jan. 2013, doi: 10.1016/j.ast.2011.11.009.
[147] S. Merdaci, A. Tounsi, M. S. A. Houari, I. Mechab, H. Hebali, and S. Benyoucef, 'Two new refined shear displacement models for functionally graded sandwich plates', *Arch Appl Mech*, vol. 81, no. 11, pp. 1507–1522, Nov. 2011, doi: 10.1007/s00419-010-0497-5.
[148] M. Ameur, A. Tounsi, I. Mechab, and A. A. El Bedia, 'A new trigonometric shear deformation theory for bending analysis of functionally graded plates resting on elastic foundations', *KSCE J Civ Eng*, vol. 15, no. 8, pp. 1405–1414, Nov. 2011, doi: 10.1007/s12205-011-1361-z.
[149] H.-T. Thai and T. P. Vo, 'A new sinusoidal shear deformation theory for bending, buckling, and vibration of functionally graded plates', *Applied Mathematical Modelling*, vol. 37, no. 5, pp. 3269–3281, Mar. 2013, doi: 10.1016/j.apm.2012.08.008.
[150] A. M. A. Neves *et al.*, 'A quasi-3D sinusoidal shear deformation theory for the static and free vibration analysis of functionally graded plates', *Composites Part B: Engineering*, vol. 43, no. 2, pp. 711–725, Mar. 2012, doi: 10.1016/j.compositesb.2011.08.009.
[151] A. M. Zenkour and M. H. Aljadani, 'Buckling analysis of actuated functionally graded piezoelectric plates via a quasi-3D refined theory', *Mechanics of Materials*, vol. 151, p. 103632, Dec. 2020, doi: 10.1016/j.mechmat.2020.103632.
[152] H.-T. Thai and S.-E. Kim, 'A simple quasi-3D sinusoidal shear deformation theory for functionally graded plates', *Composite Structures*, vol. 99, pp. 172–180, May 2013, doi: 10.1016/j.compstruct.2012.11.030.

[153] M. Sid Ahmed Houari, A. Tounsi, and O. Anwar Bég, 'Thermoelastic bending analysis of functionally graded sandwich plates using a new higher order shear and normal deformation theory', *International Journal of Mechanical Sciences*, vol. 76, pp. 102–111, Nov. 2013, doi: 10.1016/j.ijmecsci.2013.09.004.

[154] K. K. Żur, M. Arefi, J. Kim, and J. N. Reddy, 'Free vibration and buckling analyses of magneto-electro-elastic FGM nanoplates based on nonlocal modified higher-order sinusoidal shear deformation theory', *Composites Part B: Engineering*, vol. 182, p. 107 601, Feb. 2020, doi: 10.1016/j.compositesb.2019.107601.

[155] A. M. Zenkour, 'A simple four-unknown refined theory for bending analysis of functionally graded plates', *Applied Mathematical Modelling*, vol. 37, no. 20, pp. 9041–9051, Nov. 2013, doi: 10.1016/j.apm.2013.04.022.

[156] A. M. Zenkour, 'Bending analysis of functionally graded sandwich plates using a simple four-unknown shear and normal deformations theory', *Jnl of Sandwich Structures & Materials*, vol. 15, no. 6, pp. 629–656, Nov. 2013, doi: 10.1177/1 099 636 213 498 886.

[157] J. L. Mantari and C. Guedes Soares, 'A novel higher-order shear deformation theory with stretching effect for functionally graded plates', *Composites Part B: Engineering*, vol. 45, no. 1, pp. 268–281, Feb. 2013, doi: 10.1016/j.compositesb.2012.05.036.

[158] C. H. Thai, A. J. M. Ferreira, S. P. A. Bordas, T. Rabczuk, and H. Nguyen-Xuan, 'Isogeometric analysis of laminated composite and sandwich plates using a new inverse trigonometric shear deformation theory', *European Journal of Mechanics - A/Solids*, vol. 43, pp. 89–108, Jan. 2014, doi: 10.1016/j.euromechsol.2013.09.001.

[159] J. L. Mantari, A. S. Oktem, and C. Guedes Soares, 'A new trigonometric shear deformation theory for isotropic, laminated composite and sandwich plates', *International Journal of Solids and Structures*, vol. 49, no. 1, pp. 43–53, Jan. 2012, doi: 10.1016/j.ijsolstr.2011.09.008.

[160] H. Ait Atmane, A. Tounsi, I. Mechab, and E. A. Adda Bedia, 'Free vibration analysis of functionally graded plates resting on Winkler–Pasternak elastic foundations using a new shear deformation theory', *Int J Mech Mater Des*, vol. 6, no. 2, pp. 113–121, Jun. 2010, doi: 10.1007/s10 999-010-9110-x.

[161] S. Benyoucef, I. Mechab, A. Tounsi, A. Fekrar, H. Ait Atmane, and E. A. Adda Bedia, 'Bending of thick functionally graded plates resting on Winkler–Pasternak elastic foundations', *Mech Compos Mater*, vol. 46, no. 4, pp. 425–434, Nov. 2010, doi: 10.1007/s11 029-010-9159-5.

[162] N. El Meiche, A. Tounsi, N. Ziane, I. Mechab, and E. A. Adda.Bedia, 'A new hyperbolic shear deformation theory for buckling and vibration of functionally graded sandwich plate', *International Journal of Mechanical Sciences*, vol. 53, no. 4, pp. 237–247, Apr. 2011, doi: 10.1016/j.ijmecsci.2011.01.004.

[163] H.-T. Thai, T. P. Vo, T. Q. Bui, and T.-K. Nguyen, 'A quasi-3D hyperbolic shear deformation theory for functionally graded plates', *Acta Mech*, vol. 225, no. 3, pp. 951–964, Mar. 2014, doi: 10.1007/s00 707-013-0994-z.

[164] K. P. Soldatos, 'A transverse shear deformation theory for homogeneous monoclinic plates', *Acta Mechanica*, vol. 94, no. 3, pp. 195–220, Sep. 1992, doi: 10.1007/BF01 176 650.
[165] A. Mahi, E. A. Adda Bedia, and A. Tounsi, 'A new hyperbolic shear deformation theory for bending and free vibration analysis of isotropic, functionally graded, sandwich and laminated composite plates', *Applied Mathematical Modelling*, vol. 39, no. 9, pp. 2489–2508, 2015, doi: 10.1016/j.apm.2014.10.045.
[166] F. Ebrahimi and A. Jafari, 'A four-variable refined shear-deformation beam theory for thermo-mechanical vibration analysis of temperature-dependent FGM beams with porosities', *Mechanics of Advanced Materials and Structures*, vol. 25, no. 3, pp. 212–224, Feb. 2018, doi: 10.1080/15 376 494.2016.1255820.
[167] M. Karama, K. S. Afaq, and S. Mistou, 'Mechanical behaviour of laminated composite beam by the new multi-layered laminated composite structures model with transverse shear stress continuity', *International Journal of Solids and Structures*, vol. 40, no. 6, pp. 1525–1546, Mar. 2003, doi: 10.1016/S0020-7683(02)00 647-9.
[168] M. Karama, K. S. Afaq, and S. Mistou, 'A new theory for laminated composite plates', *Proceedings of the Institution of Mechanical Engineers, Part L: Journal of Materials: Design and Applications*, vol. 223, no. 2, pp. 53–62, Apr. 2009, doi: 10.1243/14 644 207JMDA189.
[169] A. M. Zenkour and A. F. Radwan, 'Bending and buckling analysis of FGM plates resting on elastic foundations in hygrothermal environment', *Archiv.Civ.Mech.Eng*, vol. 20, no. 4, p. 112, Sep. 2020, doi: 10.1007/s43 452-020-00 116-z.
[170] A. M. Zenkour and M. H. Aljadani, 'Porosity effect on thermal buckling behavior of actuated functionally graded piezoelectric nanoplates', *European Journal of Mechanics - A/Solids*, vol. 78, p. 103 835, Nov. 2019, doi: 10.1016/j.euromechsol.2019.103835.
[171] X. Yang, S. Sahmani, and B. Safaei, 'Postbuckling analysis of hydrostatic pressurized FGM microsized shells including strain gradient and stress-driven nonlocal effects', *Engineering with Computers*, vol. 37, no. 2, pp. 1549–1564, Apr. 2021, doi: 10.1007/s00 366-019-00 901-2.
[172] M. Aydogdu, 'A new shear deformation theory for laminated composite plates', *Composite Structures*, vol. 89, no. 1, pp. 94–101, Jun. 2009, doi: 10.1016/j.compstruct.2008.07.008.
[173] C. H. Thai, S. Kulasegaram, L. V. Tran, and H. Nguyen-Xuan, 'Generalized shear deformation theory for functionally graded isotropic and sandwich plates based on isogeometric approach', *Computers & Structures*, vol. 141, pp. 94–112, Aug. 2014, doi: 10.1016/j.compstruc.2014.04.003.
[174] L. Dozio, 'Exact free vibration analysis of Lévy FGM plates with higher-order shear and normal deformation theories', *Composite Structures*, vol. 111, pp. 415–425, May 2014, doi: 10.1016/j.compstruct.2014.01.014.
[175] M. Bouazza, A. Tounsi, E. A. Adda-Bedia, and A. Megueni, 'Thermoelastic stability analysis of functionally graded plates: An analytical approach',

Computational Materials Science, vol. 49, no. 4, pp. 865–870, Oct. 2010, doi: 10.1016/j.commatsci.2010.06.038.

[176] H. Asadi and Q. Wang, 'Dynamic stability analysis of a pressurized FG-CNTRC cylindrical shell interacting with supersonic airflow', *Composites Part B: Engineering*, vol. 118, pp. 15–25, Jun. 2017, doi: 10.1016/j.compositesb.2017.03.001.

[177] H.-T. Thai and S.-E. Kim, 'Analytical solution of a two variable refined plate theory for bending analysis of orthotropic Levy-type plates', *International Journal of Mechanical Sciences*, vol. 54, no. 1, pp. 269–276, Jan. 2012, doi: 10.1016/j.ijmecsci.2011.11.007.

[178] Z. Wang and L. Ma, 'Effect of Thickness Stretching on Bending and Free Vibration Behaviors of Functionally Graded Graphene Reinforced Composite Plates', *Applied Sciences*, vol. 11, no. 23, Art. no. 23, Jan. 2021, doi: 10.3390/app112311362.

[179] H.-T. Thai and S.-E. Kim, 'Closed-form solution for buckling analysis of thick functionally graded plates on elastic foundation', *International Journal of Mechanical Sciences*, vol. 75, pp. 34–44, Oct. 2013, doi: 10.1016/j.ijmecsci.2013.06.007.

[180] Y. M. Ghugal and A. S. Sayyad, 'Free vibration of thick orthotropic plates using trigonometric shear deformation theory', *Lat. Am. j. solids struct.*, vol. 8, pp. 229–243, Sep. 2011, doi: 10.1590/S1679-78252011000300002.

[181] M. Filippi, M. Petrolo, S. Valvano, and E. Carrera, 'Analysis of laminated composites and sandwich structures by trigonometric, exponential and miscellaneous polynomials and a MITC9 plate element', *Composite Structures*, vol. 150, pp. 103–114, Aug. 2016, doi: 10.1016/j.compstruct.2015.12.038.

[182] G. Giunta, D. Crisafulli, S. Belouettar, and E. Carrera, 'Hierarchical theories for the free vibration analysis of functionally graded beams', *Composite Structures*, vol. 94, no. 1, pp. 68–74, 2011, doi: 10.1016/j.compstruct.2011.07.016.

[183] E. Carrera, 'Mixed layer-wise models for multilayered plates analysis', *Composite Structures*, vol. 43, no. 1, pp. 57–70, Sep. 1998, doi: 10.1016/S0263-8223(98)00097-X.

[184] E. Carrera, 'Theories and Finite Elements for Multilayered Plates and Shells:A Unified compact formulation with numerical assessment and benchmarking', *ARCO*, vol. 10, no. 3, pp. 215–296, Sep. 2003, doi: 10.1007/BF02736224.

[185] E. Carrera, S. Brischetto, and A. Robaldo, 'Variable Kinematic Model for the Analysis of Functionally Graded Material plates', *AIAA Journal*, vol. 46, no. 1, pp. 194–203, Jan. 2008, doi: 10.2514/1.32490.

[186] G. Giunta, D. Crisafulli, S. Belouettar, and E. Carrera, 'A thermo-mechanical analysis of functionally graded beams via hierarchical modelling', *Composite Structures*, vol. 95, pp. 676–690, Jan. 2013, doi: 10.1016/j.compstruct.2012.08.013.

[187] C. He, J. Zhu, Y. Hua, D. Xin, and H. Hua, 'A study on the vibration characteristics of functionally graded cylindrical beam in a thermal

environment using the Carrera unified formulation', *Mechanics of Advanced Materials and Structures*, vol. 0, no. 0, pp. 1–13, Aug. 2023, doi: 10.1080/15 376 494.2023.2242861.
[188] R. Leetsch, T. Wallmersperger, and B. Kröplin, 'Thermomechanical Modeling of Functionally Graded Plates', *Journal of Intelligent Material Systems and Structures*, vol. 20, no. 15, pp. 1799–1813, Oct. 2009, doi: 10.1177/1 045 389X08 098 097.
[189] F. A. Fazzolari and E. Carrera, 'Thermal Stability of FGM Sandwich Plates Under Various Through-the-Thickness Temperature Distributions', *Journal of Thermal Stresses*, vol. 37, no. 12, pp. 1449–1481, Dec. 2014, doi: 10.1080/01 495 739.2014.937251.
[190] I. A. Ramos, J. L. Mantari, A. Pagani, and E. Carrera, 'Refined theories based on non-polynomial kinematics for the thermoelastic analysis of functionally graded plates', *Journal of Thermal Stresses*, vol. 39, no. 7, pp. 835–853, Jul. 2016, doi: 10.1080/01 495 739.2016.1189771.
[191] M. Farrokh and H. S. Mousavi Fard, 'An extension of Carrera unified formulation in polar coordinates for mechanical and thermal buckling analysis of axisymmetric FG circular plate using FEM', *Mechanics of Advanced Materials and Structures*, vol. 0, no. 0, pp. 1–9, Nov. 2022, doi: 10.1080/15 376 494.2022.2142885.
[192] M. Cinefra, E. Carrera, S. Brischetto, and S. Belouettar, 'Thermo-Mechanical Analysis Of Functionally Graded Shells', *Journal of Thermal Stresses*, vol. 33, no. 10, pp. 942–963, Sep. 2010, doi: 10.1080/01 495 739.2010.482379.
[193] J. C. Monge and J. L. Mantari, 'Thermal bending response of functionally graded magneto-electric–elastic shell employing non-polynomial model', *Mechanics of Advanced Materials and Structures*, vol. 30, no. 14, pp. 2882–2898, Jul. 2023, doi: 10.1080/15 376 494.2022.2064570.
[194] J. C. Monge, J. L. Mantari, and M. A. Hinostroza, 'Non-polynomial hybrid models for the bending of magneto-electro-elastic shells', *Mechanics of Advanced Materials and Structures*, vol. 0, no. 0, pp. 1–35, Mar. 2023, doi: 10.1080/15 376 494.2023.2190743.
[195] M. H. Ghadiri Rad and S. M. Hosseini, 'Application of the CUF–EFG method for buckling analysis of the multilayer GPLs–CNTs-reinforced FG plates with cutout', *Mechanics of Advanced Materials and Structures*, vol. 0, no. 0, pp. 1–17, Sep. 2022, doi: 10.1080/15 376 494.2022.2116664.
[196] A. M. A. Neves, 'Analysis of laminated and functionally graded plates and shells by a unified formulation and collocation with radial basis functions', Doctoral thesis, Faculdade de Engenharia, Universidade do Porto Departamento de Engenharia Mecânica, 2012. Accessed: Aug. 28, 2023. [Online]. Available: https://repositorio-aberto.up.pt/handle/10 216/75 571
[197] B. A. Finlayson and L. E. Scriven, 'The method of weighted residuals—a review', *Appl. Mech. Rev*, vol. 19, no. 9, pp. 735–748, 1966.
[198] A. H. Nayfeh and P. F. Pai, *Linear and nonlinear structural mechanics*. John Wiley & Sons, 2008.
[199] Y. Wang, C. Feng, Z. Zhao, and J. Yang, 'Eigenvalue buckling of functionally graded cylindrical shells reinforced with graphene platelets (GPL)',

Composite Structures, vol. 202, pp. 38–46, Oct. 2018, doi: 10.1016/j.compstruct.2017.10.005.
[200] Irving H. Shames and Clive L. Dym, *Energy and finite element methods in structural mechanics*. CRC Press (Taylor and Francis Group), 1985.
[201] J. N. Reddy, *Theory and Analysis of Elastic Plates and Shells*, Second. CRC Press (Taylor and Francis Group), 2007.
[202] M. Shariyat and K. Asemi, '3D B-spline finite element nonlinear elasticity buckling analysis of rectangular FGM plates under non-uniform edge loads, using a micromechanical model', *Composite Structures*, vol. 112, pp. 397–408, Jun. 2014, doi: 10.1016/j.compstruct.2014.02.005.
[203] S. Abrate, 'Functionally graded plates behave like homogeneous plates', *Composites Part B: Engineering*, vol. 39, no. 1, pp. 151–158, Jan. 2008, doi: 10.1016/j.compositesb.2007.02.026.
[204] T. Morimoto, Y. Tanigawa, and R. Kawamura, 'Thermal buckling of functionally graded rectangular plates subjected to partial heating', *International Journal of Mechanical Sciences*, vol. 48, no. 9, pp. 926–937, Sep. 2006, doi: 10.1016/j.ijmecsci.2006.03.015.
[205] S. Krenk and J. Høgsberg, *Statics and Mechanics of Structures*. Dordrecht: Springer Netherlands, 2013. doi: 10.1007/978-94-007-6113-1.
[206] A. Mahi, E. A. Adda Bedia, A. Tounsi, and I. Mechab, 'An analytical method for temperature-dependent free vibration analysis of functionally graded beams with general boundary conditions', *Composite Structures*, vol. 92, no. 8, pp. 1877–1887, Jul. 2010, doi: 10.1016/j.compstruct.2010.01.010.
[207] Amale Mahi, 'Analyse et étude des plaques composites FGM en vibrations libres', Doctoral thesis, University of Blida 1, Blida, Algeria., 2012.
[208] W. Huang *et al.*, 'Realizing load bearing-heat insulation integration of lightweight porosity-controlled SiC(rGO) bulk ceramics via precursor route for hypersonic vehicles', *Ceramics International*, p. S0 272 884 222 025 275, Jul. 2022, doi: 10.1016/j.ceramint.2022.07.134.
[209] M. I. A. Latiff, D. M. Nuruzzaman, S. Basri, N. M. Ismail, S. N. S. Jamaludin, and F. F. Kamaruzaman, 'Preparation and characterization of 6-layered functionally graded nickel-alumina (Ni-Al2O3) composites', *IOP Conf. Ser.: Mater. Sci. Eng.*, vol. 342, p. 012 063, Apr. 2018, doi: 10.1088/1757-899X/342/1/012 063.
[210] G. Jin, Z. Su, S. Shi, T. Ye, and S. Gao, 'Three-dimensional exact solution for the free vibration of arbitrarily thick functionally graded rectangular plates with general boundary conditions', *Composite Structures*, vol. 108, pp. 565–577, Feb. 2014, doi: 10.1016/j.compstruct.2013.09.051.
[211] H. Guo, S. Cao, T. Yang, and Y. Chen, 'Vibration of laminated composite quadrilateral plates reinforced with graphene nanoplatelets using the element-free IMLS-Ritz method', *International Journal of Mechanical Sciences*, vol. 142–143, pp. 610–621, Jul. 2018, doi: 10.1016/j.ijmecsci.2018.05.029.
[212] K. D. Nguyen and H. Nguyen-Xuan, 'An isogeometric finite element approach for three-dimensional static and dynamic analysis of functionally

graded material plate structures', *Composite Structures*, vol. 132, pp. 423–439, 2015, doi: https://doi.org/10.1016/j.compstruct.2015.04.063.

[213] E. E. Ghandourah, A. A. Daikh, A. M. Alhawsawi, O. A. Fallatah, and M. A. Eltaher, 'Bending and Buckling of FG-GRNC Laminated Plates via Quasi-3D Nonlocal Strain Gradient Theory', *Mathematics*, vol. 10, no. 8, p. 1321, Apr. 2022, doi: 10.3390/math10 081 321.

Appendix A

Matrices elements

The elements of the stiffness and inertia matrices are given as follows:

$$
\begin{aligned}
k_{11} &= A_{11}\alpha^2 + A_{66}\beta^2 \\
k_{12} &= \alpha\beta\left(A_{12} + A_{66}\right) \\
k_{13} &= \left(B^a_{11} - B_{11}\right)\alpha^3 + \left(2B^a_{66} - 2B_{66} + B^a_{12} - B_{12}\right)\alpha\beta^2 \\
k_{14} &= B^a_{11}\alpha^2 + B^a_{66}\beta^2 \\
k_{15} &= \left(B^a_{66} + B^a_{12}\right)\alpha\beta \\
k_{22} &= A_{22}\beta^2 + A_{66}\alpha^2 \\
k_{23} &= \alpha^2\beta\left(2B^a_{66} - 2B_{66} + B^a_{12} - B_{12}\right) + \beta^3\left(B^a_{22} - B_{22}\right) \\
k_{24} &= \left(B^a_{66} + B^a_{12}\right)\alpha\beta \\
k_{25} &= B^a_{66}\alpha^2 + B^a_{22}\beta^2 \\
k_{33} &= \left(D_{11} - 2D^a_{11} + D^{aa}_{11}\right)\alpha^4 + 2\left(2D_{66} - 4D^a_{66} + 2D^{aa}_{66} + D_{12} - 2D^a_{12} + D^{aa}_{12}\right)\alpha^2\beta^2 \\
&\quad + \left(D_{22} - 2D^a_{22} + D^{aa}_{22}\right)\beta^4 + \alpha^2 A^a_{55} + \beta^2 A^a_{44} \\
k_{34} &= \left(D^{aa}_{11} - D^a_{11}\right)\alpha^3 + \left(D^{aa}_{12} - D^a_{12} + 2D^{aa}_{66} - 2D^a_{66}\right)\alpha\beta^2 + A^a_{55}\alpha \\
k_{35} &= \left(D^{aa}_{22} - D^a_{22}\right)\beta^3 + \left(D^{aa}_{12} - D^a_{12} + 2D^{aa}_{66} - 2D^a_{66}\right)\beta\alpha^2 + A^a_{44}\beta \\
k_{44} &= D^{aa}_{11}\alpha^2 + D^{aa}_{66}\beta^2 + A^a_{55} \\
k_{45} &= \left(D^{aa}_{12} + D^{aa}_{66}\right)\alpha\beta \\
k_{55} &= D^{aa}_{22}\beta^2 + D^{aa}_{66}\alpha^2 + A^a_{44}
\end{aligned}
\tag{A1}
$$

$$
\begin{aligned}
m_{11} &= I_1 \\
m_{12} &= 0 \\
m_{13} &= \left(I^a_2 - I_2\right)\alpha \\
m_{14} &= I^a_2 \\
m_{15} &= 0 \\
m_{22} &= I_1 \\
m_{23} &= \left(I^a_2 - I_2\right)\beta \\
m_{24} &= 0 \\
m_{25} &= I^a_2 \\
m_{33} &= I_1 + \left(I^{aa}_3 + I_3 - 2I^a_3\right)\left(\alpha^2 + \beta^2\right) \\
m_{34} &= \left(I^{aa}_3 - I^a_3\right)\alpha \\
m_{35} &= \left(I^{aa}_3 - I^a_3\right)\beta \\
m_{44} &= I^{aa}_3 \\
m_{45} &= 0 \\
m_{55} &= I^{aa}_3
\end{aligned}
\tag{A2}
$$

Appendix B

Solution algorithm

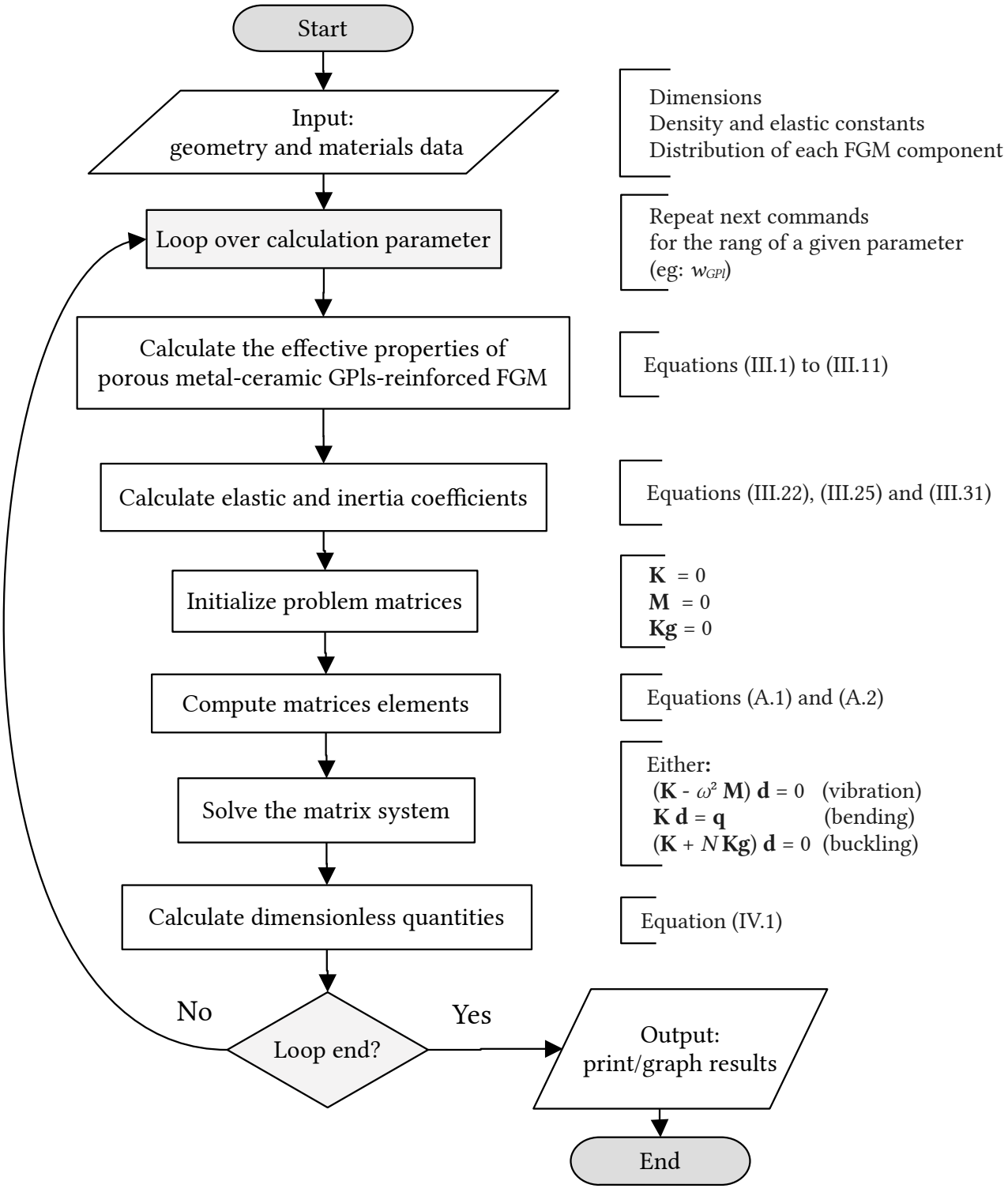

Figure B1: Organigram of solution algorithm for the mechanical analysis of porous GPls-reinforced FGM plate.

Appendix C

Buckling modes shapes

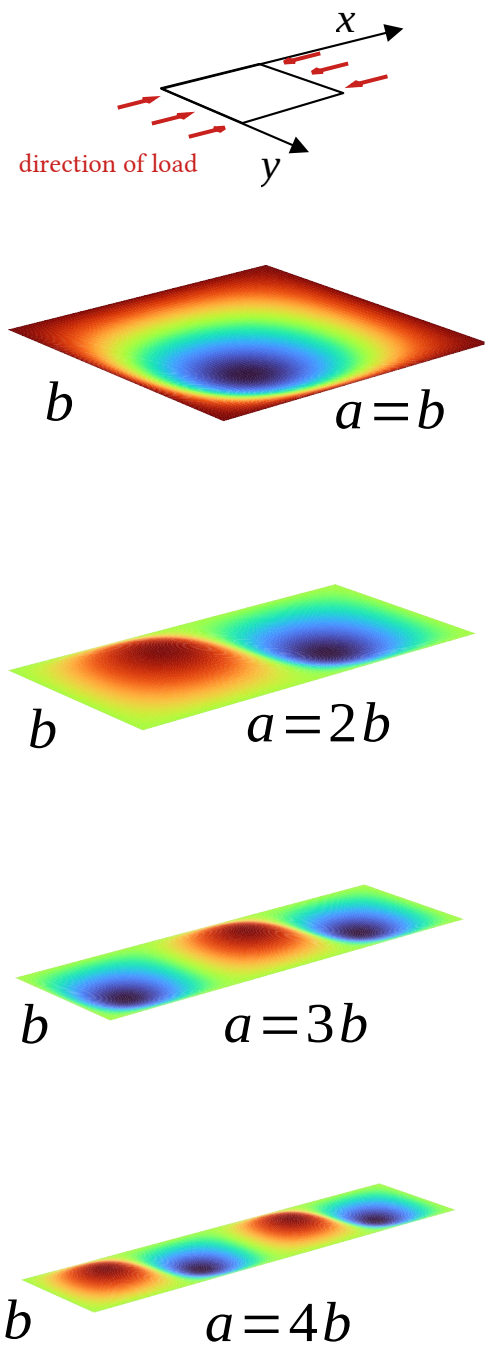

Figure C1: Effect of aspect ratio of rectangular FGM plates on the buckling mode shape.